# Convective Dynamics of the Tropical Atmosphere in Three Idealized Approaches

by

Martin Velez Pardo

B.S. Environmental Engineering, Universidad de los Andes, 2017

B.A. History, Universidad de los Andes, 2015

Submitted to the Department of Earth, Atmospheric and Planetary Sciences
in partial fulfillment of the requirements for the degree of

DOCTOR OF PHILOSOPHY IN ATMOSPHERIC SCIENCE

at the

MASSACHUSETTS INSTITUTE OF TECHNOLOGY

February 2024



Authored by: Martin Velez Pardo
Department of Earth, Atmospheric and Planetary Sciences
January 12, 2024

Certified by: Timothy W. Cronin
Associate Professor of Atmospheric Science, Thesis Supervisor

Accepted by: Robert D. van der Hilst
Schlumberger Professor of Earth and Planetary Sciences
Head of Department of Earth, Atmospheric, and Planetary Sciences

# Convective Dynamics of the Tropical Atmosphere in Three Idealized Approaches

by

Martin Velez Pardo

Submitted to the Department of Earth, Atmospheric and Planetary Sciences
on January 12, 2024 in partial fulfillment of the requirements for the degree of

DOCTOR OF PHILOSOPHY IN ATMOSPHERIC SCIENCE

## ABSTRACT

Atmospheric convection organized at large spatial scales significantly influences precipitation patterns and weather events in tropical and subtropical regions, and has a rich, two-way interaction with Earth's climate. Tropical cyclones, mesoscale convective complexes, heat lows, and the rainbands of the Intertropical Convergence Zone are all examples of such large-scale convective organization, but despite their relevance for human life and ecosystems, the mechanisms that govern their formation and many of their characteristics are not fully understood. This work presents three studies of convective dynamics in the tropical atmosphere using idealized frameworks. In the first part, we use direct numerical simulations of simple setups of rotating dry convection based on the Rayleigh-Bénard system to study minimal conditions that produce large-scale convective organization, and the spontaneous formation of tropical-cyclone-like structures. We find that the latter form more readily for a particular set of controlling parameters and thermal boundary conditions, characterized by a slow enough rotation rate, asymmetry of the heat fluxes at the boundaries, effective internal cooling, and a dependence of the low-level heat flux on the overlying flow. In the second part, we use rotating tank experiments of turbulent convection to probe further some of the findings of the first part, particularly the formation of large-scale cyclonic flows with top-bottom asymmetric, flux-based thermal boundary conditions, in a setup with hot water insulated at the bottom and sides, and cooling freely to the air above. We find large, persistent cyclonic vortices in experiments with a similar range of governing parameters as the results from the numerical simulations in the first part, particularly for cases where

the convective time scale is shorter than the rotational time scale, that is, for convective Rossby numbers greater than about 1. Our approach in the first two parts seeks to narrow the disciplinary gap between traditional turbulence research and the physics of atmospheric convective organization and tropical cyclones. In the third part, we turn to the topic of the mechanisms that drive precipitation in the tropics at scales of tens to a few hundred kilometers. Using cloud-resolving model simulations, we study how rainfall responds to imposed anomalies in the surface temperature, the atmospheric heating rate at different heights, and the pressure gradients that drive the winds near the surface. We find that such forcings lead to self-consistent but different relationships between the amount of rainfall produced and the net heating of the atmosphere, quantified by the Normalized Gross Moist Stability. We show that the spatial extent of the forcings affects how well this relationship can be inferred from horizontally-averaged atmospheric properties. In contrast, we find that the relationship between rainfall and the average relative humidity in the atmosphere falls onto the same curve for all types of environmental forcings considered. As a general contribution, the three parts of this work highlight the fruitfulness of a diverse set of idealized approaches in deriving a more mechanistic understanding of the convective dynamics of the atmosphere.

Thesis supervisor: Timothy W. Cronin
Title: Associate Professor of Atmospheric Science

# Acknowledgments

Sometimes, an abundance of things to say makes it difficult to say anything at all. These lines are an attempt to make explicit some of the deep gratitude that underlies the rest of this thesis, and all of my efforts, intellectual and personal, over the past five and a half years.

I first thank my advisor, Tim Cronin, for his truly unwavering support through the good and the difficult times. For hundreds of discussions and exchanges that have substantially shaped the way I think about the atmosphere, about science, and about my own ideas, intuitions, and learning process. For giving me interesting and challenging problems to work on, and for teaching me by example about selfless mentorship, rigor, intellectual honesty, and self-discipline. I appreciate the many lighthearted conversations about Kieran's growth, development and antics, and find great inspiration in how Tim seamlessly integrates a deep love for his family and a keen devotion to his craft. His uncanny ability to methodically dissect a tough problem and see right through to its core has been a continual source of learning, inspiration and courage in my own intellectual journey.

I thank my de facto second advisor for four years, and my friend, the late Peter Molnar, who passed away in June of 2022. Peter marked my life, like that of many in academia and outside, with his candor, generosity, and his boundless, relentless and contagious intellectual curiosity. The weeks spent with Tim, Peter and Sara Neustadtl at Peter and Sara's home in Colorado doing science, hiking in the mountains and talking about music, books, cultures, politics and life, are among the fondest memories of the PhD experience.

I am grateful for the generous support and feedback from my thesis committee members, Kerry Emanuel, Glenn Flierl and Morgan O'Neill. I thank Kerry for his support in helping my work gain visibility among the fluid dynamics and the atmospheric science communities, and

for his many lessons through his inspiring lectures, papers, talks, and through our exchanges. It is hard to overstate the influence that Kerry has had in imbuing multiple generations of researchers in meteorology and climate science with the desire to understand the mechanisms that govern atmospheric phenomena in the simplest terms possible. I am grateful to be part of that tradition. I thank Glenn for teaching me two of the most challenging classes I have ever taken, on turbulence and on large-scale dynamics—they opened a new and rich way of thinking about geophysical fluids for me. The contrast between his kind, unassuming attitude and his profound knowledge and insight is a lesson in humility that I appreciate just as much as all the math and physics I have learned from him. He has also been invariably generous with his time, and with his help in the fluids' lab during my experimental thesis work. I thank Morgan for accepting to join my committee as an external member despite an unfavorable time difference, for her flexibility and generosity with her time even through early motherhood(!), for helping me maintain rigor by asking hard questions without losing the slightest bit in friendliness, and for being a role model in my own pursuit of a style that aptly balances assertiveness and empathy.

I also thank David McGee for guiding me through my brief foray in the study of paleoclimate, and for his great generosity in the face of unforeseen challenges; and Paul O'Gorman, for teaching me about atmospheric dynamics and climate change through elegant simple models and interesting paper discussions.

I appreciate the many interactions with my fellow labmates in the Cronin group, Tristan Abbott, Paul Nicknish, Nick Lutsko, Tom Beucler and Daniel Koll. I owe Tristan extra gratitude for his disinterested help and his generosity with his time and knowledge in my early and more clueless years, and for his help with the particle tracker used in chapter 3.

A heartfelt thank you to:

My close friends in the department and MIT, Constantin Arnscheidt, Matthieu Kohl, Praneeth Gurumurthy, Prajwal Niraula and Sarah Greer. Each one of you has made my PhD life better in unique ways, and has made me a better human. I hope our friendship endures through the years and despite the long distances and reduced contact.

Laura Ramírez, who has been there in one way or another since we were 5 years old: gracias por tu amistad y tu apoyo constante.

Silvia Villalba, Camila Guerrero, Gabriela Navas, Laura Montenegro, Franklin González: gracias por estar ahí a pesar de la distancia.

The many resourceful and helpful staff members in EAPS, especially to Ann Greaney-Williams, Alma Pellecer, Jaga Purevsuren, Daisy Caban, Megan Jordan and Roberta Allard.

The DEAPS co-organizers and pre-frosh, for a lot of shared joyful memories: Lodovica Illari, John Marshall, Bill McKenna, Phoebe Lin, Grace O'Neil, Lily Zhang, Sean Chen, Zach Molitor, Nicholas Wei, Mason Fang, Brian Hoh, Philip PJ Tuckman, and many others.

My EAPS friends Anuar Togaibekov, Casey Densmore, Erik Tamre, Hanyuan Liu, Jeffrey Grabon, Jonathan Lin, Julia Wilcots, Kasturi Shah, Lesly Franco, Mara Freilich, Mason Rogers, Mira Santos, Raphael Rousseau-Rizzi, Robert van der Drift, Rohini Shivamoggi, Santiago Benavides, Sydney Sroka, Ziwei Li, and several others with whom I wish I had had more chances to interact.

The many dear friends or meaningful companions in Colombia, Boston or elsewhere, Ana M. García, Ana Restrepo, Carlos Arturo Bedoya, Evgeniya Prikhodko, Héctor Ruiz, Hyung Joo Park, Jesús Prada (Yisus), Jingtian Chen, Juan Diego Villegas (Juandi), Juan Luis González (Juanlu), Justin Lim, Kevin Zhang, Leidys Gutiérrez, Luis A. Gutiérrez (Lucho), Nancy Ruiz (Nans), Ranjan Anantharaman, Shashi Krishnagowda, Sinja Küppers, Tsung-Lin Hsieh, Víctor Restrepo, Yipeng Ge, Zoey Song, and all other friends made at Cornell, in Sid-Pac, in school, and elsewhere.

Dr. Rheinila Fernandes, for her warm and insightful support, and for helping me be a better (and less sleep-deprived) human being.

All my high-school and undergraduate mentors, and particularly to my thesis advisors in engineering, Ricardo Morales, and in history, Claudia Leal, for helping me pursue my quirky curiosity.

Other mentors who will not read this thesis, but who have shaped through their ideas much of who I am and how I think: Thich Nhat Hanh, Jesus of Nazareth, Carl Sagan, Richard Feynman, Sam Harris, Ursula K. Le Guin, Bertrand Russell, Karl Popper, Sean Carroll, Robert Sapolsky, Anna Lembke, Steven Pinker, Sabine Hossenfelder, Christopher Hitchens, Yuval Noah Harari, Chimamanda Ngozi Adichie, Ted Chiang, Jorge Luis Borges, Grant Sanderson, Simon Clark, and a rather long etc.

My family, for raising me in an environment filled with love, warmth and joy, and inculcating in me the pursuit of honesty, humility, compassion, integrity and curiosity.

My five grandparents, Lucía Toro, José J. Pardo, Alberto Vélez, Elena Cadavid, María Martínez (Uchita), for all you have taught me about love, loss, and life. Están siempre conmigo.

My aunts, uncles and cousins/a mis tíos y primos: gracias por mantener un hogar extenso de alegría, apoyo y cariño.

Luz Mary Mina, Diana Zapata y Emilly Mena: gracias por su presencia en nuestra vida. Las quiero!

Last but never least, to my mom, dad and brother: a mamá, por su amor incondicional, su calidez, su paciencia, y por inculcarme el amor por los libros. A papá, por su tenacidad, su cariño, su nobleza, y por enseñarme a observar y apreciar la naturaleza. A mi hermano Pedro, por su alegría contagiosa, su generosidad, su ejemplo de servicio, y por el amor compartido por la ciencia, el pensamiento, y el bien de la humanidad.

A ustedes, todo. I would not be here without your love.

I acknowledge support from NSF Grant 1740533, and the MIT Presidential Fellowship.

# Contents

# List of Figures

# List of Tables

# Chapter 1

# Introduction

"Physics is mathematical not because we know so much about the physical world, but because we know so little; it is only its mathematical properties that we can discover."

–Bertrand Russell, *An Outline of Philosophy*, 1927 (in Russell, 2009)

This thesis is about atmospheric convection and how some of its idealized formulations can offer insights into the physics of tropical cyclones, large-scale cyclonic flows like heat lows, and tropical rainfall at scales of tens to hundreds of kilometers. As much as fluid convection is the common theme, the overarching spirit of the work is an emphasis on idealization as a key to connecting complex atmospheric processes to a simpler mechanistic understanding, and to the more general framework of fluid mechanics.

We may find Russell's use of the word "discover" in the quote above too restrictive: we do not wait to have a mathematical formulation for newly observed phenomena in order to call them discoveries. Moreover, coming upon an unexplored territory, a lost ancient manuscript or an unobserved galaxy are uncontroversially regarded as acts of discovery in their own right. Despite this, it is not hard to agree with Russell that something fundamental is missing when we observe some phenomenon or object and are unable to distill part of its essence into a simpler, more general framework of thought; to define some of its coordinates in the map—or phase space—where we encode our knowledge of reality.

The atmosphere is not spared in this pursuit of simplification: the human drive to describe the world using a common conceptual framework applies, naturally, to the flow of the

air we breathe, the rain that allows our crops to grow, and the storms that threaten our communities. In particular through the lens of physics and the language of mathematics, we have found unprecedented success in reducing the complexity of atmospheric and fluid phenomena at all scales, drawing precise commonalities between processes as seemingly disparate as the overturning motion of water in a pot heated on a stove and the thunderstorm that appears to grow out of thin air on a sunny summer afternoon.

Many studies in atmospheric and climate science today rely on the use of complex models that attempt to capture as many of the processes of the climate system as computational resources allow. Often, by selectively reducing aspects of the model complexity—removing some effect, homogenizing some boundary condition, simplifying the relationship between some variables—such studies are able to discern patterns and trends that can guide our understanding of the climate system for one purpose or another. This approach, fruitful for a large number of applications, inherently contends with the challenge of establishing if the observed patterns and trends are physically meaningful, or an artifact of the web of inscrutable relationships between a multitude of tuned parameters used to represent unresolved physical processes.

In a sense, this work goes in the opposite direction: by starting with the equations of motion and highly idealized boundary conditions or forcings, we use numerical simulations (chapters 2 and 4) and tank experiments (chapter 3) to try to capture the essence of different phenomena associated with convection that we observe on Earth's tropical atmosphere.

## 1.1 Context and terminology

Before motivating and outlining the chapter contents in more detail, some terminology and context are in order. In the atmospheric and planetary science literature, convection specifically refers to the vertical motions that result from density anomalies in a fluid subject to the effect of gravity, where "vertical" denotes the direction of the gravitational vector (Emanuel, 1994). A more general definition of convection can include other body forces besides gravity, or other buoyancy mechanisms, but those are outside the scope of this work. Importantly, two types of convection are commonly distinguished in atmospheric science: dry and moist.

Moist convection refers to processes that involve phase changes, such as the condensation of water vapor that occurs as warm air ascends and cools, and their associated latent effects. In dry convection, such phase changes are absent. The terminology can be confusing at first to the non-meteorologist, because a buoyant parcel of a liquid like water typically undergoes dry convection, as there are no phase changes involved in the process, despite the semantic association of the word "moist" with liquids.

Another concept that we will refer to throughout the text is "large-scale organization". Convection is a dominant feature of the tropical troposphere, and is associated with a wide taxonomy of phenomena at different scales. While the typical width of a single convective plume or thermal in the troposphere ranges from a few hundred meters to several kilometers (Orlanski, 1975), convective clusters can organize at scales of hundreds to thousands of kilometers in events with distinct dynamics like tropical cyclones, mesoscale convective complexes, the Madden-Julian Oscillation (Houze Jr & Betts, 1981; Nakazawa, 1988), or the Intertropical Convergence Zone (ITCZ). Although the term "large-scale" typically references scales of thousands of kilometers in the atmospheric science literature, here we use it more broadly to denote spatial scales significantly wider than typical convective thermals or plumes, as it is often used by the fluid dynamics community.

Finally, the term "organization" used here refers to the aggregation of convection that results either spontaneously in domains with homogeneous boundary conditions and forcings—typically termed "self-aggregation" in the field—or induced by heterogeneous conditions. The specific meaning of the term is made clear in each chapter.

## 1.2 Convective organization, tropical cyclones and the Rayleigh-Bénard setup

The study of convective organization at scales significantly larger than the typical sizes of convective events has been an active area of research in the field for many decades. More recently, the discovery of convective self-aggregation in simulations of radiative-convective equilibrium (RCE), where convection spontaneously concentrates into a single large area

even for homogeneous boundaries and forcings (Bretherton et al., 2005; Held et al., 1993), has sparked renewed attention. For instance, it has been found that aggregation can be triggered and sustained by radiative feedbacks (Muller & Held, 2012; Wing & Emanuel, 2014) as well as by weaker precipitation-induced cold pools (Haerter et al., 2019; Jeevanjee & Romps, 2013) through independent pathways. Additional studies have shown that convective aggregation can be triggered by sea-surface temperature anomalies (Shamekh et al., 2020) as well as diabatic heating sources in the atmosphere (Dingley et al., 2021), although the process should not be equated with the convective organization that occurs with homogenous boundary conditions.

Early work by Gray, 1975 identified cloud-radiation interactions as important in the organization of convection into cloud clusters during the early stages of tropical cyclogenesis. Recent studies have provided evidence for this view (Carstens & Wing, 2020; Khairoutdinov & Emanuel, 2013; Rappin et al., 2010; Shi & Bretherton, 2014). Modeling work from the last couple of years has shown that radiative effects dominate at early stages of genesis, while surface enthalpy fluxes and their flow dependence become a dominant effect for subsequent intensification and maintenance (Ruppert Jr et al., 2020; Wing, 2022).

Surface latent and sensible heat fluxes have been recognized to play a central role in tropical cyclone energetics since the mid-twentieth century (Kleinschmidt, 1951; Malkus & Riehl, 1960; Riehl, 1950), and have been linked quantitatively to the potential strength of mature tropical cyclones in the formulation of potential intensity (PI) theory (Emanuel, 1986). In simple terms, it is argued that as near-surface winds spiral inwards towards the low pressure center in a tropical cyclone, net enthalpy is gained by the air from the warm water surface, by virtue of the lower temperature and the water vapor subsaturation of air (sensible and latent contributions, respectively), and this higher enthalpy sustains the storm's warm core. This is known by the acronym "WISHE", or wind-induced surface heat exchange. Crucially, turbulent effects cause surface fluxes to depend approximately linearly on the near-surface wind speeds ($F_{H,E} \propto \|U\|$ ) which is thought to lead to a positive feedback loop where stronger winds translate to enhanced fluxes and vice versa, until the frictional dissipation becomes strong enough to balance the process.

Separate lines of work have provided evidence that relatively intense cyclonic storms can

also arise when the feedback described above is artificially weakened (Montgomery et al., 2015) or suppressed (Ramírez Reyes & Yang, 2021), although it has been shown that storms reach significantly stronger intensities and do so much faster when a WISHE-like mechanism is present (Zhang & Emanuel, 2016).

Despite continuing progress on all fronts described, it is not yet clear if rotation and the simplest forms of large-scale convective organization are in themselves sufficient to produce tropical-cyclone-like flows, and to what extent surface-flux feedbacks affect the process of tropical cyclone formation and intensification.

In chapter 2, we tackle these questions using direct numerical simulations of the Rayleigh-Bénard model of convection, one of the simplest and most widely used convective setups in fluid dynamics, with added rotation. Chapter 3 in turn uses rotating tank experiments of Rayleigh-Bénard-like convection to study further some of the results from chapter 2.

In its classical formulation, the rotating Rayleigh-Bénard setup consists of a fluid contained between a warm bottom plate and a cold top plate, subject to a downward-pointing gravitational force and an upward-pointing rotation vector. For large enough values of the temperature difference between the top and bottom plates, convective instability occurs.

While the majority of efforts involving Rayleigh-Bénard have focused on basic research on fluid dynamics and thermodynamics—such as the conditions for the onset of convective instability, the scaling of heat transport in different parameter regimes, or the conditions leading to regime transitions—the setup has been adapted for several applications to atmospheric physics, for example by incorporating moisture in the study of moist convection (Pauluis & Schumacher, 2010; Vallis et al., 2019) and moist convective aggregation (Pauluis & Schumacher, 2011); by adding moisture and rotation in the study of hurricanes (Chien et al., 2022), or by prescribing internal cooling to better emulate tropical convection conditions on earth (Berlengiero et al., 2012).

A major roadblock in integrating traditional Rayleigh-Bénard setups and the study of tropical cyclones is the purely dry nature of convection in the former, while moisture has long been recognized to be essential for hurricanes on Earth. However, as will be discussed in more detail in the chapters ahead, the discovery of dry hurricanes in simulations by Mrowiec et al., 2011, inspired by Emanuel, 1986, made that connection possible.

The mentioned approaches that have attempted to make Rayleigh-Bénard more Earth-like by introducing moisture and internal cooling to study atmospheric phenomena are valuable in their own right. However, using the dry, more traditional form of the setup allows us to establish a more direct dialogue between the physics of convective organization, tropical cyclones, and other large-scale convective flows on the one hand, and a substantial wealth of knowledge derived from over a century of basic turbulence research on the other.

## 1.3 Rainfall responses to forcings

The spatial and temporal distribution of rainfall in the tropics is not yet thoroughly understood (Back & Bretherton, 2009; Back & Bretherton, 2006; Schneider et al., 2014). The complex interaction between deep convection and different forcings makes a mechanistic explanation of the processes involved particularly challenging. Both mechanical forcings—such as those from large-scale and orographic air convergence—and thermodynamic forcings—including mid- and upper-tropospheric diabatic heating and heterogeneous sea-surface temperature fields—modulate deep convection and precipitation at various spatial and temporal scales, so an ultimate framework explaining the location and timing of rainfall must take them both into account.

The last research chapter of the thesis focuses on understanding how tropical convection and rainfall respond to mechanical and thermodynamic forcings at scales of a few tens to a few hundreds of kilometers. Since precipitation is the core issue, the chapter deals, unsurprisingly, with moist convection, in contrast with the first two.

To study the problem, we introduce simplified forcings over a reference region in a set of cloud-resolving model simulations of the tropical atmosphere in radiative-convective equilibrium (RCE) to contrast their effects on rainfall. RCE has been a seminal framework in the study of tropical convection, in particular, and climate dynamics as a whole, since the pioneering work of Manabe and Wetherald, 1967. It refers to an equilibrium between net heating by enthalpy fluxes from the surface and net radiative cooling in the troposphere. A domain in RCE can be seen as a self-contained "little world" where balance does not depend

on horizontal transport to or from outside. [1]

The chapter contrasts the effects of purely mechanical and thermodynamic—or column-energetic—forcings on rainfall at the scales mentioned, and discusses them through the lens of the Gross Moist Stability (GMS). The concept of Gross Moist Stability was first introduced by the influential work of Neelin and Held, 1987 as a vertically integrated measure of the moist static stability. In essence, it quantifies the export of moist static energy per export of dry static energy, although alternative though equivalent formulations exist.

A recent, more general formulation of the GMS is that by Raymond et al., 2009, which we use in modified form in chapter 4: starting from the budgets of moist static energy and moisture in steady state, one can write a relationship between the net precipitation $P - E$ (where $P$ is precipitation and $E$ is evaporation at the surface), and the total atmospheric heating rate, $\dot{Q}_{atm} = F_s - R$ (where $F_s$ is the net enthalpy flux from the surface, and $R$ is the pressure-integrated sink due to radiative cooling). This relationship is given by

$$P - E = \frac{\dot{Q}_{atm}}{\Gamma_R}. \tag{1.1}$$

where $\Gamma_R$, the Normalized Gross Moist Stability (NGMS), mediates the relationship between net precipitation and net atmospheric column heating. The NGMS thus provides a simple factor to translate forcings to the column energy into precipitation responses. We use it as a way to characterize the effects of different types of forcings, and argue about its advantages and shortcomings in the chapter.

As a final point, it is worth returning to the concept of idealized modeling. An atmospheric model run at convection-permitting resolutions in RCE includes significantly more processes than the dry, rotating, Boussinesq form of the Navier-Stokes equations used in Rayleigh-Bénard, and cannot be characterized by a handful of governing parameters. In this sense, the last research chapter is anchored in a more complex formulation of tropical convective dynamics than the first two, while still retaining a great deal of simplicity. This illustrates that we can obtain valuable knowledge about the climate system by combining approaches with different degrees of idealization. In that way, and perhaps only in that

[1] RCE is broadly representative of what happens in the tropics, though not all the time at all locations. For an observational study of the validity of RCE on Earth, see (Jakob et al., 2019).

way, can we avoid the antipodal risks of oversimplification and of sacrificing our attempt to understand in favor of our ability to merely simulate climate. [2]

[2]For a couple of lucid reflections about the use of a hierarchy of complexity in modeling studies of climate, see Held (2005) and Jeevanjee et al. (2017).

# Chapter 2

# Large-Scale Circulations and Dry Tropical Cyclones in Direct Numerical Simulations of Rotating Rayleigh-Bénard Convection

This chapter is published as Velez-Pardo, M., and T. W. Cronin, 2023. "Large-Scale Circulations and Dry Tropical Cyclones in Direct Numerical Simulations of Rotating Rayleigh-Bénard Convection." *J. Atmos. Sci.*, 80, 2221–2237, https://doi.org/10.1175/JAS-D-23-0018.1. 

## 2.1 Abstract

The organization of convection into relatively long-lived patterns of large spatial scales, like tropical cyclones, is a common feature of the Earth's atmosphere. However, many key aspects of convective aggregation and its relationship with tropical cyclone formation remain elusive. In this work, we simulate highly idealized setups of dry convection, inspired by the Rayleigh-Bénard system, to probe the effects of different thermal boundary conditions on the scale of organization of rotating convection, and on the formation of tropical-cyclone-like structures. We find that in domains with sufficiently high aspect ratios, moderately turbulent ($\mathrm{Ra_f} \gtrsim 10^9$), moderately rotating ($\mathrm{Ro_c} \gtrsim 1$) convection organizes more persistently and at larger

scales when thermal boundary conditions constrain heat fluxes rather than temperatures. Furthermore, for some thermal boundary conditions with asymmetric heat fluxes, convection organizes into persistent vortices with the essential properties of mature tropical cyclones: a warm core, high axisymmetry, a strong azimuthal circulation, and substantially larger size than individual buoyant plumes. We argue that flux asymmetry results in a localized input of buoyancy which allows spatially aggregated convection to sustain a warm core in a developing large-scale vortex. Crucially, the most intense and axisymmetric cyclone forms for setups where the bottom heat flux is enhanced by the nearby flow and the top boundary is insulating, as long as the convective Rossby number is higher than about 1. Our results demonstrate the great potential for dialogue between classical turbulence research and the study of convective aggregation and tropical cyclones.

## 2.2 Introduction

In this work, we present evidence that cyclonic vortices that share the essential dynamical and thermodynamic characteristics of dry tropical cyclones can form in direct numerical simulations of simple setups of dry, rotating turbulent convection. We also show that the combined effects of convective aggregation and rotation are necessary but not sufficient to produce spontaneous cyclogenesis in a dry convective domain, and that only some combinations of thermal boundary conditions are likely to lead to spontaneous dry tropical cyclone formation. This constitutes a step forward in an effort to bring together dry turbulence research and tropical atmospheric dynamics, particularly the study of convective organization and tropical cyclone physics.

Meteorologists define a Tropical Cyclone—TC henceforth—by its structure and geographical location as “a warm-core non-frontal synoptic-scale cyclone, originating over tropical or subtropical waters, with organized deep convection and a closed surface wind circulation about a well-defined center" (National Hurricane Center, n.d.). We take the view here that the essential features of a TC are a low-pressure center, a warm convective core that covers a substantially larger area than individual buoyant thermals, and an axisymmetric, cyclonic, bottom-intensified circulation coupled with the convective region (Cronin & Chavas, 2019).

The formation of TCs in the absence of latent heat fluxes and moisture was first postulated and confirmed for an axisymmetric numerical model in radiative-convective equilibrium

by Mrowiec et al. (2011). Their work inferred this possibility from the formulation of Potential Intensity theory (Emanuel, 1986; Rotunno & Emanuel, 1987), which implied that mature tropical cyclones could be sustained by a strong enough total surface enthalpy flux, regardless of the relative contribution of latent and sensible sources. Subsequent work in 3-D atmospheric simulations has shown that TC-like structures emerge in a wide range of regimes of moisture availability including totally dry conditions (Cronin & Chavas, 2019), and that they share many characteristics with those simulated in a moist atmosphere where irreversible phase changes are suppressed (Wang & Lin, 2020, 2021).

The discovery of dry TCs in simulations has started to narrow the gap separating the study of real-world TCs and traditional turbulence research. Primarily, it has shown that moisture and its irreversible phase changes, with all their associated complexity, need not always be considered to understand important aspects of tropical cyclone physics, such as the connection between convective aggregation and TC formation. This motivates asking if TC-like structures, and the closely related phenomenon of convective organization, can be studied in simplified setups of fluid motion. A quintessential example of such a setup is the Rayleigh-Bénard model of convection—RBC henceforth—formulated on the basis of experimental work by Henri Bénard (Bénard, 1901) and subsequent theoretical treatment by Lord Rayleigh (Rayleigh, 1916) in the early twentieth century. In its basic form, it consists of a layer of Boussinesq fluid contained between a warm, impenetrable horizontal plate at the bottom, and a cold one at the top.

The RBC setup with rotation and others derived from it have been used for decades as a paradigmatic framework for the study of astro- and geophysical convection, both in laboratory experiments and numerical simulations, e.g. (Boubnov & Golitsyn, 1986; Chandrasekhar, 1953; Julien et al., 1996; King et al., 2012; Kunnen, 2021; Nieves et al., 2014; Rossby, 1969; Stevens et al., 2009, 2013). Much interest has been given to the rapidly rotating regime in particular, where the time scale of rotation is substantially shorter than that of convection—that is, where the convective Rossby number, $\mathrm{Ro_c}$, is much less than unity (for a recent review of rotating RBC, see Ecke and Shishkina (2023)). Large-scale vortices have been shown to emerge in the highly turbulent, rapidly rotating regime for domains with anisotropic geometries (Guervilly & Hughes, 2017; Guervilly et al., 2014; Julien

et al., 2018). Unlike tropical cyclones, however, their structure is depth-invariant, and their formation depends on the horizontal aspect ratios being greater than 1.1:1.

A distinctive feature of tropical cyclones is the high level of organization of convection. For instance, model-based studies of moist convection have shown that, when combined with rotation, aggregated convective clusters often become tropical cyclones (Bretherton et al., 2005; Carstens & Wing, 2020; Muller & Romps, 2018; Nolan et al., 2007). For dry RBC setups, numerical simulations and theoretical work have shown that convective aggregation happens readily in domains where the boundary conditions are prescribed as constant fluxes instead of constant temperatures. In non-rotating RBC, constant-flux boundaries lead to the formation of a convective cell that spans the whole domain, as shown by early studies of mantle convection (Chapman & Proctor, 1980; Hurle et al., 1967), and more recently for internally heated/cooled convection close to the onset of convective instability (Goluskin, 2016; Lepot et al., 2018). Vieweg et al. (2021) have shown through Lyapunov analysis that this aggregation towards large scales persists above the critical Rayleigh number, and well into the highly turbulent regime.

To our knowledge, only a handful of studies so far have brought together the conditions of prescribed heat fluxes at the boundaries and slow rotation for 3-D RBC (Dowling, 1988; Takehiro et al., 2002; Vieweg et al., 2022). Importantly, they have found that even rotation rates within the slowly rotating regime—with Rossby numbers of O(10)—can constrain the aggregation to sizes that are not domain-limited, provided that the rotation is not too slow. Furthermore, a couple of recent studies have shown that cyclonic vortices with eye-like structures form in axisymmetric simulations of relatively slowly rotating, non-turbulent RBC with lateral walls and constant flux thermal boundaries (Oruba et al., 2017, 2018), although it is unclear if these phenomena can arise in 3-D, highly turbulent simulations in the absence of lateral confinement. It is worth noting that an unpublished dissertation by (Kannan, 2023) has recently explored tropical cyclogenesis within a similar framework of horizontally-constrained, rotating RBC using large-eddy simulations (LES) and hydrodynamic instability analysis. However, the material is currently not publicly available for proprietary reasons, and we lack enough information about the setup, parameter space or findings to draw a proper comparison with the literature or the present work.

A different line of work has modified the original RBC system to include a simple analogue for latent heating, simulating a lapse rate that is stable to dry and unstable to moist convection (Pauluis & Schumacher, 2010). Although more complex than the classical RBC, this "Moist Rayleigh-Bénard" system has made possible the study of aggregation (Pauluis & Schumacher, 2011) and tropical cyclone formation (Chien et al., 2022) under relatively simple conditions that are one step closer to those we observe on Earth. Particularly, Chien et al. (2022) have found that TC-like structures form when the parameter determining the conditional instability is high enough, and that simulations with convective aggregation in the non-rotating case yield TC-like vortices when a strong enough rotation is introduced. However, a preexisting conditional instability is not likely the primary source of energy for real-world TCs, and a more realistic formulation should account for the fundamental energetic contribution from surface fluxes (Craig & Gray, 1996). In particular, the enhancement of surface heat fluxes by the overlying flow of air, also referred to as wind-induced surface heat exchange, or WISHE, has been shown to play a fundamental role in setting the strength of real-world tropical cyclones (Chavas, 2017; Emanuel, 1986; Zhang & Emanuel, 2016).

These recent efforts share a similar objective to ours: to better understand the nature of convective organization and TC formation, and its relation to the basic equations of fluid motion. These are thus complementary approaches that strive to gain insights into different aspects of the same big problem. By limiting our study to dry convection, our approach to the question sacrifices more of the realism of the phenomena in favor of preserving greater simplicity in their conceptualization. The motivation behind this is twofold: on the one hand, dry TCs have been shown to arise in models and their dynamics are not fully understood yet. On the other, we see great inherent value in creating a dialogue between the traditional studies of dry convection in idealized settings and tropical atmospheric physics.

In this chapter, we use numerical simulations of the Boussinesq equations in the Rotating RBC setup in the moderately rotating, moderately turbulent regime, to show the effects of different thermal boundary conditions and rotation rates on convective organization, and on the formation of TC-like vortices. Additionally, we introduce a simple parameterization that relates the magnitude of the heat flux at the bottom to the overlying flow, and show that the flow dependence of the heat fluxes—or, in other words, a wind-induced surface heat exchange

mechanism—can significantly enhance the strength of the TC-like vortices. We characterize the vortex properties, and conclude by commenting on the role of flux asymmetry, rotation and convective organization on their formation.

## 2.3 Methods

We run a suite of direct numerical simulations of 3-D, dry, turbulent convection to explore the phenomena of convective organization and dry tropical cyclone formation and persistence under different combinations of thermal boundary conditions. For the simulations, we use the pseudo-spectral PDE solver Dedalus, version 2, (Burns et al., 2020) to solve the Navier-Stokes, continuity, and heat equations with the Boussinesq approximation and the thermal boundary conditions explained below. The basic setup consists of a 3-D domain that is doubly-periodic in the horizontal, bounded by impenetrable surfaces and with no-slip flow conditions at the top and bottom, and uses 512 by 512 Fourier basis functions in the horizontal, and 32 Chebyshev basis functions in the vertical, which increase in density near the boundaries.

### 2.3.1 Governing equations and parameter regime

The equations governing the dynamics of the flow in the rotating setup are the Boussinesq form of the Navier-Stokes system for momentum and mass continuity, and a thermodynamic equation (the heat equation), namely:

$$\frac{\partial \vec{u}}{\partial t} + \vec{u} \cdot \nabla \vec{u} + 2\vec{\Omega} \times \vec{u} = -\nabla p + \vec{g}\beta T + \nu \nabla^2 \vec{u} \tag{2.1}$$

$$\nabla \cdot \vec{u} = 0 \tag{2.2}$$

$$\frac{\partial T}{\partial t} + \vec{u} \cdot \nabla T = \kappa \nabla^2 T. \tag{2.3}$$

Here, $\vec{g}$ is the gravitational acceleration, $\vec{u}$ is the flow velocity field, $\vec{\Omega}$ is the vector of rotation, aligned with the vertical direction, $T$ is the temperature deviation with respect to a constant reference value $T_0$, $\beta$ is the coefficient of thermal expansion of the fluid, $\nu$ is

the kinematic viscosity, and $\kappa$ is the thermal diffusivity. $p$ denotes the modified pressure, which incorporates the hydrostatic pressure head, namely $p = p_r/\rho_0 + gz\hat{z}$ (Chandrasekhar, 1961; Ecke & Shishkina, 2023), where $p_r$ is the actual pressure, $z$ is the height over a fixed reference, and $\rho_0$ is the base state density.

We non-dimensionalize our system in two different ways: on the one hand, for convection induced by a prescribed heat flux $Q$ at a boundary, we scale the lengths by the depth of the fluid layer, $H$; the flow velocities by the convective velocity scale, $W^* = (F_B H)^{1/3}$, where $F_B$ is the buoyancy flux, and is given by $F_B = \frac{g\beta Q}{\rho c_p}$, with $c_p$ the specific heat at constant pressure, and $\rho$ the density of the fluid, and the rotation rate by $\Omega$. These yield a scaling of $\nabla \sim \frac{1}{H}, t \sim \frac{H^{2/3}}{F_B^{1/3}}, p \sim (F_B H)^{2/3}, T \sim \frac{{F_B}^{2/3}}{g\beta H^{1/3}}$. The heating itself is incorporated through the boundary conditions, detailed in the next subsection. On the other hand, for convection between two plates at fixed temperatures, we non-dimensionalize $T$ by $\Delta T$, the temperature difference between the plates, and the velocities by the free-fall velocity scale, $W_{ff} = \sqrt{g\beta\Delta T H}$. This gives t $\sim \sqrt{\frac{H}{g\beta\Delta T}}, p \sim g\beta\Delta T H$.

The dimensionless equations become:

$$\frac{\partial \vec{u}}{\partial t} + \vec{u}\cdot\nabla\vec{u} + \frac{1}{\mathrm{Ro_c}}\hat{e}_3 \times \vec{u} = -\nabla p + T\hat{e}_3 + \frac{1}{\mathrm{R}}\nabla^2\vec{u} \tag{2.4}$$

$$\nabla\cdot\vec{u} = 0 \tag{2.5}$$

$$\frac{\partial T}{\partial t} + \vec{u}\cdot\nabla T = \frac{1}{\mathrm{P}}\nabla^2 T. \tag{2.6}$$

For the flux-based non-dimensionalization, $\mathrm{R} = \left(\frac{\mathrm{Ra_f}}{\mathrm{Pr}^2}\right)^{1/3}$, and $\mathrm{P} = (\mathrm{Ra_f Pr})^{1/3}$, where $\mathrm{Ra_f} = \frac{Q\beta g H^4}{c_p \rho \nu \kappa^2} = \frac{F_B H^4}{\nu\kappa^2}$ is the flux Rayleigh number, which can be seen as the ratio of the time scales of diffusive to convective thermal transport, and $\mathrm{Pr} = \frac{\nu}{\kappa}$ is the Prandtl number, or the ratio of the kinematic viscosity to the thermal diffusivity. For the temperature-based scales, we have in turn $\mathrm{R} = \left(\frac{\mathrm{Ra}}{\mathrm{Pr}}\right)^{1/2}$ and $\mathrm{P} = (\mathrm{RaPr})^{1/2}$, where $\mathrm{Ra} = \frac{g\beta\Delta T H^3}{\nu\kappa}$ is the temperature-based Rayleigh number, typically referred to simply as the Rayleigh number. $\mathrm{Ro_c}$ is the convective Rossby number, which represents the ratio of the timescales of rotation to convection, and takes the form $\mathrm{Ro_c} = \left(\frac{F_B}{H^2}\right)^{1/3} \cdot \frac{1}{2\Omega}$ for the flux-based scaling, and $\mathrm{Ro_c} = \left(\frac{g\beta\Delta T}{H}\right)^{1/2} \cdot \frac{1}{2\Omega}$ for the temperature-based one. The system is thus governed by three dimensionless parameters:

the convective Rossby number, $\mathrm{Ro_c}$, the Prandtl number, and either the temperature-based or the flux-based Rayleigh number, Ra or $\mathrm{Ra_f}$.

The 3-D dry cyclones simulated by Cronin and Chavas (2019) provide some guidelines for a plausible region of parameter space to find TCs in a dry convective setup, since a parallel can be traced between RBC and the more earth-like conditions of three-dimensional Radiative-Convective Equilibrium. An approximate layer depth H $\sim 10^4$ m, a vertical velocity w $\sim 1$ m/s, and a Coriolis parameter $f \sim 10^{-4}$ s$^{-1}$ yield a value of $\mathrm{Ro_c} = O(1)$. While realistic atmospheric conditions are characterized by Rayleigh numbers between $O(10^{18})$ and $O(10^{22})$, this is far above the level of turbulence that direct numerical simulations can resolve at present, which are closer to Ra $\sim 10^{10}$ (Plumley & Julien, 2019), which for Pr = 1 corresponds to $\mathrm{Ra_f}$ between $10^{13.3}$ and $10^{15}$, depending on how the heat transport scales with Ra (Aurnou et al., 2020). Such forcings would be expected to yield Reynolds numbers Re $\sim 10^4$ (Fonda & Sreenivasan, 2015).

We choose a value of $\mathrm{Ra_f} = 10^9$ for all simulations with at least one flux-based thermal boundary condition, and Ra $= 10^{7.3}$ for the simulation with fixed-temperature boundaries. These values are chosen such that the resulting convection is in the moderately to highly turbulent regime with flows characterized by Reynolds numbers Re $\sim 10^3$. We diagnose the Reynolds numbers in our simulations as $\mathrm{Re} = \mathrm{R} \cdot (\|\vec{u}\|)_{dom}$ , where R is the parameter associated with the viscous terms in the dimensionless momentum equations, and $(\|\vec{u}\|)_{dom}$ is the domain-averaged value of the dimensionless magnitude of the simulated flow. Using a diagnostic criterion like the Reynolds number as an indication of the strength of turbulence allows us to circumvent the problem of finding an adequate theoretical relationship between $\mathrm{Ra_f}$ and Ra, since our goal is merely to ensure broadly similar regimes. The relatively low choice of Rayleigh and Reynolds numbers compared to what is technically feasible is an attempt to balance the trade-offs in computational cost between running too few simulations at very high levels of turbulence, and many simulations with a very weak thermal forcing. For our simulations, we confine our attention to a value of Pr = 1.0, which lies in between those typical for gases (0.7) and water (6.9) on Earth (Rapp, 2016).

Four basic time scales can be defined for our system: two diffusive time scales for heat and momentum diffusivities, namely $H^2/\kappa$ and $H^2/\nu$; a convective time scale, $t_{Conv} = H/W$

, where $W$ represents $W^*$ or $W_{ff}$ for the flux-based or the temperature-based setups, respectively, and a rotational time scale, $t_{Rot} = 2\pi/\Omega$, which can be written in terms of the convective scale as $t_{Rot} = 4\pi \mathrm{Ro_c} t_{Conv}$, from the definition of the convective Rossby number. Although time in the dimensionless equation is non-dimensionalized by the convective scale, we will use the rotational time scale in our analysis, as it is analogous to a pendulum day.

Finally, a realistic aspect ratio $\Gamma$ (horizontal to vertical length scale) for dry TCs would be $O(10)$, taking a horizontal length scale $O(10^5)$ m. Given the high computational cost of turbulent flows in domains with large aspect ratio, most of our simulations use $\Gamma = 16$, unless stated otherwise.

### 2.3.2 Thermal boundary conditions

We explore nine different combinations of thermal boundary conditions for the simulations of rotating convection, described in Table 2.1. CF denotes a constant flux condition given by $\frac{\partial T}{\partial z} = -(\mathrm{Ra_f Pr})^{1/3}$, where the magnitude of the right-hand side represents the ratio of the scales of convective to conductive heat transport in the thermodynamic equation, i.e. $\frac{W^* H}{\kappa}$, or P in equation 2.6. This amounts to imposing a heat flux at the boundary that sustains the turbulence set by the governing parameters of the flow in the fluid interior, namely $\mathrm{Ra_f}$ and Pr . Additionally, Ins refers to an insulating condition with no heat flux, i.e. $\frac{\partial T}{\partial z} = 0$, and CT refers to constant temperature. Note that $x$ and $y$ represent the horizontal coordinates, and $z$ is the vertical, oriented with the negative of the gravitational vector.

PF denotes a parameterized heat flux condition, where $\frac{\partial T}{\partial z} = -(\mathrm{Ra_f Pr})^{1/3} \cdot (1 + C_k U_h)$, with $C_k$ a dimensionless enthalpy exchange coefficient set to 1, and $U_h$ the total horizontal wind at a height $h$, which we choose to be 1 percent of the domain depth. For reference, the choice $C_k = 1$ implies that the heat flux doubles when the horizontal wind speed at $h$ is 1. We use this as an idealized way to represent a dependence of the heat flux on the strength of the flow aloft, in analogy to the surface enhancement of enthalpy fluxes by surface roughness modeled by a flux aerodynamic formula, which constitutes the basis for WISHE.

For the simulations Ins/CF, Ins/PF, CF/PF, characterized by asymmetric flux conditions, the temperature in the whole domain increases steadily in time, but temperature differences are not eliminated, which means that convection can remain active without any

additional forcing, since it is the buoyancy and not the absolute temperature that has dynamical relevance. In these setups, the effective cooling is a consequence of the asymmetry in the fluxes at the top and the bottom boundaries, which cause the fluid in the interior to lose buoyancy (or to "cool") with respect to the fluid at the bottom, while it gains less (CF/PF) or no buoyancy at all (for Ins/CF and Ins/PF) with respect to the fluid near the top. This is similar to the secular temperature drift in experiments of convection with an internal radiative heating source (Bouillaut et al., 2019). For the setup Ins/CT, an internal cooling term with magnitude -1 in the dimensionless equation (equivalent to a factor of $(\mathrm{Ra_f Pr})^{1/3}$ times the scale of thermal diffusion) is introduced, so that the domain does not become isothermal and suppress convection. The conditions CT/CT correspond to the classical Rayleigh-Bénard model (Bénard, 1901; Rayleigh, 1916), where the top and bottom boundaries are held at fixed temperatures, maintaining an adverse thermal gradient.

For our numerical experiments, we hold Pr constant and equal to 1, hold Ra constant and equal to $10^{7.3}$ for CT/CT, and $\mathrm{Ra_f} = 10^9$ for all other setups. We initially fix $\mathrm{Ro_c}$ to 2 to focus on the effects of the different thermal boundary conditions on the organization of convection and the formation of TCs, but subsequently explore the effects of varying $\mathrm{Ro_c}$ as well. It is worth noting that these nine sets of thermal boundary conditions correspond to all possible combinations from among (PF, CF, CT, Ins) that are physically distinct and able to sustain convection, because the governing equations are invariant to the combined replacement $z \to -z, T \to -T$.

For CT/CT and Ins/CT, an adverse vertical profile of temperature is prescribed at the outset with a temperature drop of 1, so that, for a large enough flux Rayleigh number, the fluid is convectively unstable. The instability is initialized as $T(z) = -z - 10^{-3} \cdot N[\mu = 0, \sigma = 1] \cdot (z_t - z) \cdot (z - z_b)$, where $z_t$ and $z_b$ are the top and bottom values of $z$, and $N[\mu = 0, \sigma = 1]$ represents Gaussian noise with zero mean, and standard deviation of 1. For simulations with prescribed heat fluxes, convection is initialized from a vertically isothermal profile perturbed by Gaussian noise with amplitude $10^{-4}$ and standard normal parameters.

Table 2.1: Combinations of thermal boundary conditions used in the simulations. Conventions are detailed in the text.

| Setup | Top BC | Bottom BC |
|---|---|---|
| Ins/PF | $\frac{\partial T}{\partial z} = 0$ | $\frac{\partial T}{\partial z} = -(\mathrm{Ra_f Pr})^{1/3} \cdot (1 + C_k U_h)$ |
| CT/PF | $T = 0$ | $\frac{\partial T}{\partial z} = -(\mathrm{Ra_f Pr})^{1/3} \cdot (1 + C_k U_h)$ |
| CF/PF | $\frac{\partial T}{\partial z} = -(\mathrm{Ra_f Pr})^{1/3}$ | $\frac{\partial T}{\partial z} = -(\mathrm{Ra_f Pr})^{1/3} \cdot (1 + C_k U_h)$ |
| PF/PF | $\frac{\partial T}{\partial z} = -(\mathrm{Ra_f Pr})^{1/3} \cdot (1 + C_k U_{1-h})$ | $\frac{\partial T}{\partial z} = -(\mathrm{Ra_f Pr})^{1/3} \cdot (1 + C_k U_h)$ |
| Ins/CF | $\frac{\partial T}{\partial z} = 0$ | $\frac{\partial T}{\partial z} = -(\mathrm{Ra_f Pr})^{1/3}$ |
| CT/CF | $T = 0$ | $\frac{\partial T}{\partial z} = -(\mathrm{Ra_f Pr})^{1/3}$ |
| CF/CF | $\frac{\partial T}{\partial z} = -(\mathrm{Ra_f Pr})^{1/3}$ | $\frac{\partial T}{\partial z} = -(\mathrm{Ra_f Pr})^{1/3}$ |
| Ins/CT | $\frac{\partial T}{\partial z} = 0$ | $T = 1.0$ |
| CT/CT | $T = -0.5$ | $T = 0.5$ |

## 2.4 Results and Discussion

### 2.4.1 Convective Organization

Different combinations of thermal boundary conditions produce different levels of convective organization, as illustrated by the spatial distribution of vertically-averaged temperature anomaly, $\{T'\}$, in figure 2.1. For these simulations, the temperature anomaly is calculated with respect to the horizontal mean at each height, and braces denote a vertical average. One way to quantify the level of organization of a field F is through the scale $L_F$ proposed by Beucler and Cronin (2019), defined in this case as

$$L_F \equiv \frac{\langle \lambda \phi_F \rangle}{\langle \phi_F \rangle}, \tag{2.7}$$

where $\phi_F$ is the spatial power spectrum of $F$, $\lambda$ is the wavelength of the spatial wavevector, and angle brackets represent the spectral average given by

$$\langle A \rangle \equiv \frac{\int_{\mathbf{k}_0}^{\mathbf{k}_N} A(\mathbf{k}) d\mathbf{k}}{\int_{\mathbf{k}_0}^{\mathbf{k}_N} d\mathbf{k}}, \tag{2.8}$$

where $k_0, k_N$ are, respectively, the smallest and the Nyquist wavenumbers.

In particular, the simulations with any combination of flux-based boundary conditions

on the lower and upper boundaries (Ins, CF, PF) result in the largest scales of convective organization, with $L_{\{T'\}}$ values of 14.9 for Ins/CF, 15.3 for CF/CF, and 15.4 for Ins/PF, CF/PF, and PF/PF, indicating that features on the length scale of the domain are dominant. Those with at least one fixed-temperature boundary condition exhibit slightly finer spatial structures, with $L_{\{T'\}}$ values of 8.4, 11.5 and 11.9 for Ins/CT, CT/CF and CT/PF respectively. The classical Rayleigh-Bénard configuration, CT/CT, produces the smallest-scale spatial structure, with an $L_{\{T'\}}$ of 1.9, only about twice the domain depth and 1/8 of the domain width.

There are also differences between the highly-organized patterns of flux-only boundary conditions: CF/CF, PF/PF, and CF/PF show banded organization with a wavenumber-one structure in $x$ and little variation in $y$. In contrast, Ins/CF shows two somewhat distinct buoyant ($\{T'\} > 0$) clusters, and Ins/PF one, very distinct cluster and an approximate wavenumber-one pattern in both $x$ and $y$.

In addition to the spatial scale $L_{\{T'\}}$ as an estimate for spatial organization, we calculate the temporal autocorrelation of $\{T'\}$, defined as

$$\alpha_{\{T'\}}(\tau|t_0) = \frac{\int\int\{T'(t_0)\}\{T'(t_0+\tau)\}dxdy}{\left(\int\int\{T'(t_0)\}^2dxdy\right)^{1/2}\left(\int\int\{T'(t_0+\tau)\}^2dxdy\right)^{1/2}}, \tag{2.9}$$

where $\tau$ represents the time lag with respect to the reference time $t_0$. This metric gives information about the persistence of a spatial pattern of vertically averaged temperature anomalies. It should be noted that coherent features that are rapidly drifting in time are not registered by this temporal autocorrelation. In other words, it is an effective metric for persistence in the Eulerian but not in the Lagrangian sense, as it does not track features in space. However, the large-scale, coherent structures found in the simulations are either fixed or move slowly enough for the temporal autocorrelation to register their presence.

The simulations with two flux-based boundary conditions show greater persistence than those with one and, especially, two fixed-temperature boundary conditions, as measured by the temporal autocorrelation calculated with respect to the reference state at $t_0 = 10$ rotational time units, and plotted in figure 2.2a. This indicates that the organization of convection in PF/PF, CF/CF, Ins/PF and Ins/CF remains steady for several rotational

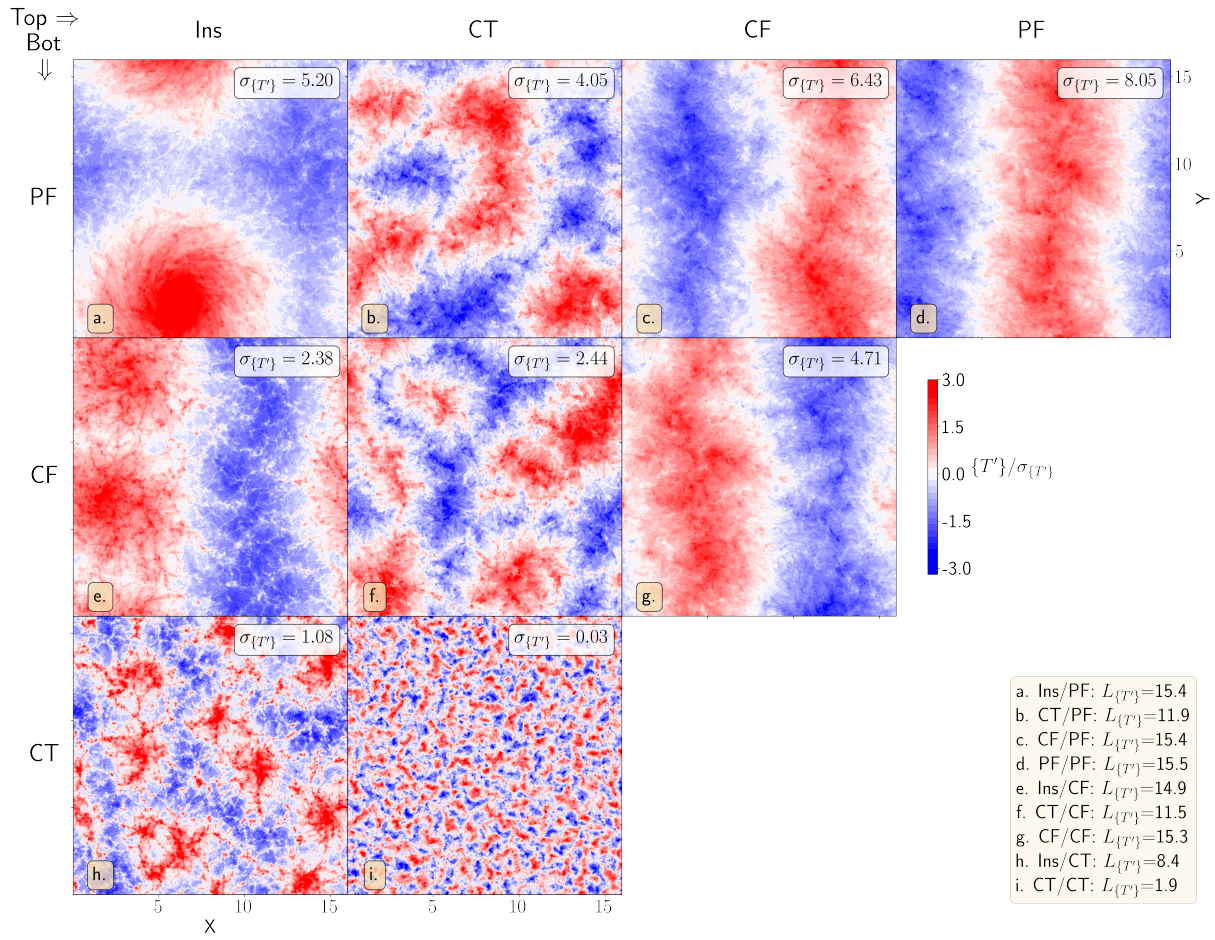


Figure 2.1: Vertically-averaged temperature anomaly, $\{T'\}$ with respect to the horizontal mean for simulations with $\mathrm{Ro_c} = 2.0$. Magnitudes are normalized by the standard deviation ($\sigma$) in each setup, and values of standard deviations are indicated for each simulation. The colorbar saturates at $\pm 2.5\sigma$. Rows represent different bottom thermal boundary conditions and columns are top boundary conditions. Ins refers to a thermally insulating boundary, CF is constant flux, PF is parameterized flux, and CT is constant temperature (see table 2.1 for details). Notably, simulations with two flux-based boundary conditions (Ins, CF or PF) show a higher level of spatial organization in $\{T'\}$ than those with one or two fixed-temperature conditions (CT). All figures correspond to the snapshot at 10 rotational time periods.

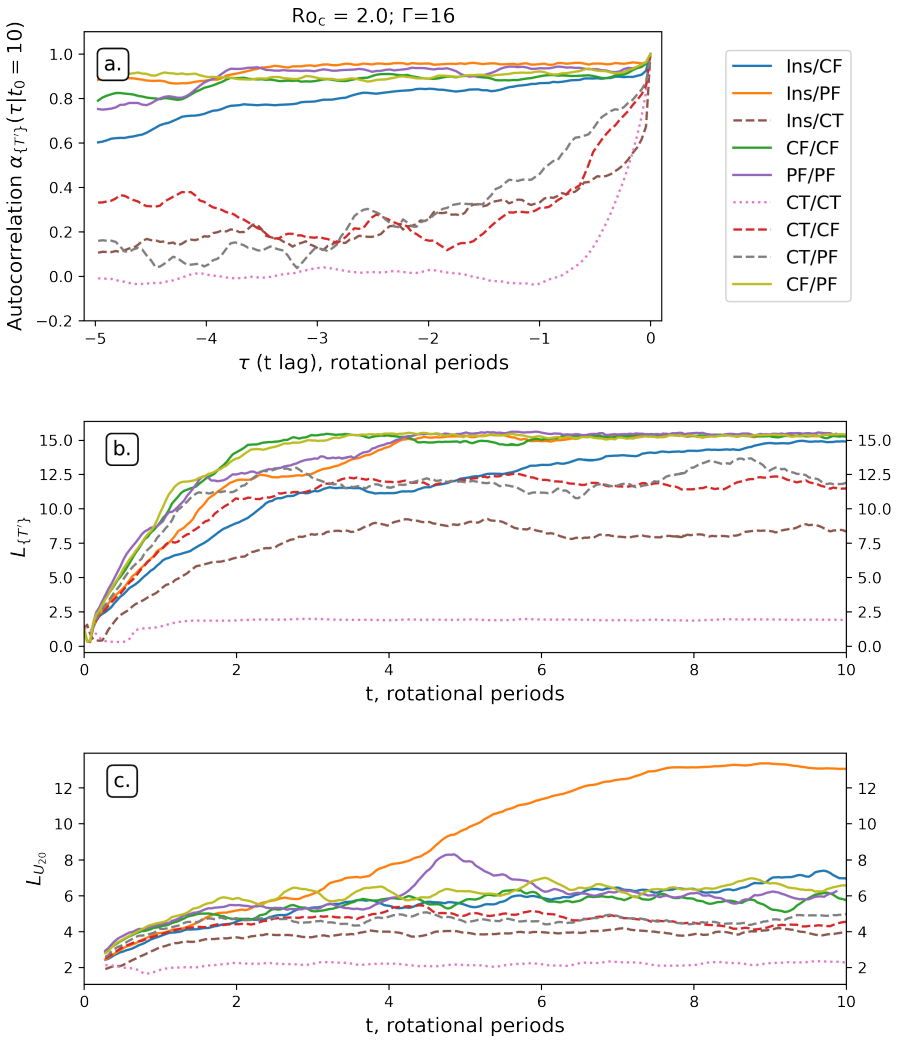


Figure 2.2: Time series of: a. autocorrelation of $\{T'\}$ for the different setups. Time lags are with respect to $t_0 = 10$ rotational time periods. Simulations with two flux-based boundary conditions exhibit higher persistence in the spatial patterns of $\{T'\}$ than those with one or two fixed-temperature conditions. b. and c. length scales $L_{\{T'\}}$ and $L_{U_{20}}$ for the spatial organization of the temperature anomaly and the horizontal wind field at 20 percent of domain height, respectively (see text for definition of L). $L_{U_{20}}$ series corresponds to a moving mean of a half rotational period for visual clarity.

time periods, while it shifts significantly within less than a rotational period for CT/CT.

Previous work has shown that in non-rotating CF/CF setups, as well as in setups with perfectly insulating conditions but internal heating or cooling, the most unstable modes at the onset of convection are those with wavenumber zero (Chapman & Proctor, 1980; Goluskin, 2016; Hurle et al., 1967); that is, the disturbances grow unbounded to span the entire domain. This has been shown to be modified by rotation Takehiro et al. (2002), with faster rotating rates leading to gradually larger wavenumbers for the most unstable modes. Although these studies have focused on the onset of turbulence, and their conclusions should not be extrapolated directly to the highly turbulent regime, Vieweg et al. (2022) have used Lyapunov analysis to show that the formation of a pair of counter-rotating convective cells that grow to the size of the domain persists for high levels of turbulence. An exploration of marginal stability for a rotating setup with different thermal boundary conditions is beyond the scope of this work, but we note that the patterns of organization seen in our simulations suggest that flux-based boundary conditions in a moderately turbulent, moderately rotating regime, also produce organization spanning the entire domain. However, the constraining effects of rotation on this large-scale organization are not seen for the combinations of $\mathrm{Ro_c}$ and $\Gamma$ used here.

### 2.4.2 Formation of Tropical-Cyclone-like vortices

Simulations with the most highly organized patterns of convection also exhibit large-scale patterns in horizontal winds, as shown in figure 2.3 by the contours of total horizontal winds at 20 percent of domain height, i.e. $\sqrt{(u(z=0.2H))^2+(v(z=0.2H))^2}$—denoted by $U_{20}$ henceforth—10 rotational time periods after initialization. In particular, a highly axisymmetric, cyclonic circulation with a well-defined eye covers a significant fraction of the domain in the Ins/PF setup, and the location of its pressure minimum is indicated with an "x". The color scale saturates at $3.5\sigma$, where $\sigma$ is the standard deviation of $U_{20}$ in each setup. This corresponds to a dimensionless wind speed of about 3.2; that is, horizontal wind speeds that are over 3.2 times the typical velocity scale for convective motions in the domain. Two smaller cyclonic vortices also form in the Ins/CF setup, similarly marked with an "x" each. In this case, $3.5\sigma$ corresponds to 1.4 in dimensionless velocity units, indicating that the vortices

are somewhat stronger than the convective velocity scale. All three vortices mentioned are found in the areas of high vertically averaged temperature anomalies of Ins/PF and Ins/CF. The storm centers are identified by applying a Gaussian filter to the map of near-surface pressure, using a binary dilation algorithm to locate contiguous regions of negative pressure anomaly, and calculating their centroid.

None of the other setups produce persistent vortex structures within 10 rotational periods, but large-scale overturning circulations are seen for those with high convective organization: CF/CF, CF/PF, and PF/PF. The traditional Rayleigh-Bénard setup, CT/CT, gives rise to convective structures with an associated cyclonic circulation in the horizontal, but they only persist for a fraction of a rotational time period, and their width, as indicated by $L_{\{T'\}}$, is constrained to within $\sim$2, differing markedly from the large, persistent structures seen in the Ins/CF and Ins/PF setups.

A length scale $L_{U_{20}}$, computed analogously to $L_{\{T'\}}$, but for the horizontal wind speeds at 20 percent of domain height, is shown at 10 rotational periods in Figure 2.3. We use the two length scales as an imperfect but helpful way to track the evolution of the scales of organization of the temperature and the horizontal wind fields (Figure 2.2, b. and c.).

In Ins/PF, $L_{\{T'\}}$ evolves similarly to other setups with two flux-based conditions: rapid growth, and saturation at the domain scale after about 4 rotational time periods However, the spatial scale of horizontal winds $L_{U_{20}}$ grows up to values of about 13, close to the domain length, and about twice the size of the setups with the next largest scales for $U_{20}$, (Ins/CF and PF/PF). The growth of large-scale horizontal flow patterns in Ins/PF and Ins/CF seems to lag the growth of the spatial organization of the thermal field by a couple of rotational periods, indicating that convective aggregation precedes the formation of large-scale, persistent vortices in those setups. At 10 rotational periods, the scales of all simulations appear to have equilibrated. We observe no qualitative difference in the formation of the TC in Ins/PF when a different amplitude ($10^{-3}$) or different seeds are used in the initialization of the convection, suggesting that the finding is robust.

Studies of spontaneous moist cyclogenesis also describe the formation of a large-scale mid-level vortex several days ahead of the formation of a tropical cyclone (Bretherton et al., 2005; Davis, 2015; Nolan et al., 2007). However, in our dry Ins/PF setup, large-scale

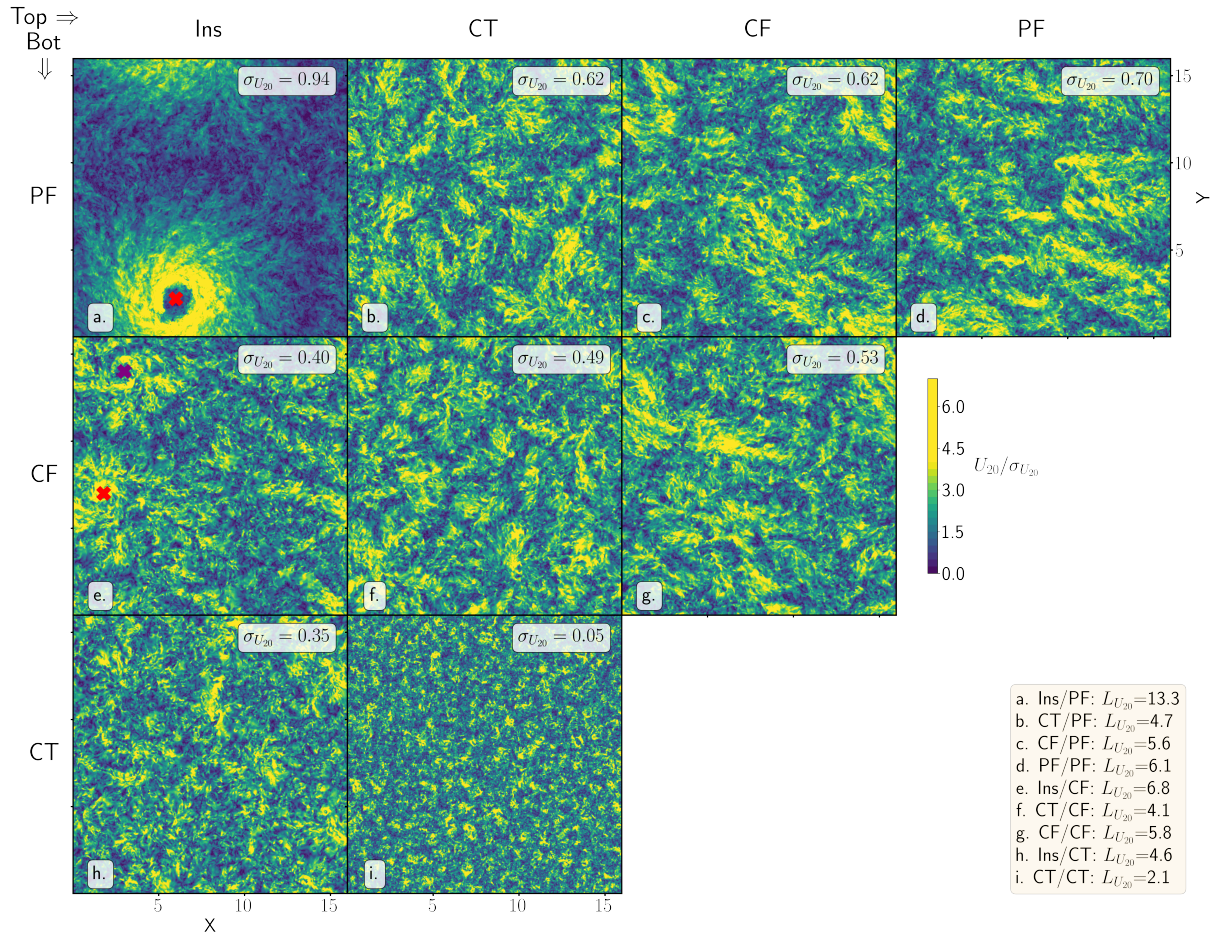


Figure 2.3: Horizontal wind at 20 percent of domain height for simulations with $\mathrm{Ro_c} = 2.0$, at 10 rotational time periods. Similar to figure 2.1, magnitudes are normalized by the standard deviation in each domain, length scales are indicated at the bottom, and color shades saturate at $3.5\sigma$. Locations of near-surface pressure minima corresponding to persistent cyclonic vortices are indicated with "x" markers.

features of the mid-level vorticity field seem to lag rather than to lead cyclogenesis (see video 1 referenced in Appendix A). Key differences between dry and moist TCs arise from the effects of condensate re-evaporation in subsaturated regions, which influence convective organization and warm-core consolidation in the latter (Davis, 2015), but recent work suggests that dry tropical cyclones exhibit similar properties and structure to moist TCs in the absence of irreversible phase changes (Wang & Lin, 2020). Because of this, we expect dry and moist tropical cyclogenesis to exhibit more similarities after significant humidification of the free troposphere by aggregated convection in the latter—an important stage in its development (Nolan, 2007).

The cyclones in Ins/PF and, to a lesser extent, Ins/CF, also share other essential characteristics of tropical cyclones, besides persistence and a horizontal scale substantially larger than that of single convective elements. One of them is slantwise neutrality, or the alignment between isentropes and constant-angular momentum surfaces around the TC. Initially formulated as a characteristic of TCs in a moist atmosphere (Emanuel, 1986), slantwise neutrality has been also shown to be a property of dry tropical cyclones in simulations with parameterized turbulence and surface processes (Wang & Lin, 2020). In a dry, Boussinesq system, slantwise neutrality requires $M = M(T)$, where $M = rV + \frac{1}{2}fr^2$ is the angular momentum per unit mass. We note that the equality implied by strict slantwise neutrality should be relaxed for non-idealized storms: $M \approx M(T)$.

Figure 2.4 shows azimuthally averaged, height-versus-radius profiles centered at the two vortices marked with a red cross (Ins/CF on the left column, Ins/PF on the right). The upper panel contrasts contours of angular momentum (black dashed lines) and the re-scaled temperature $T - T_{dom}$ (colors), where $T_{dom}$ is the domain-mean temperature. In the lower region near the vortex of the Ins/PF case, there is a relatively good alignment between lines of constant $M$ and the isentropes—for our case, those are equivalent to lines of constant $T - T_{dom}$. The alignment is less clear for the core of the vortex of Ins/CF, plausibly because of its lower axisymmetry and its weaker nature.

Another characteristic of tropical cyclones seen in both cases is a secondary circulation with radial inflow at the low levels and outflow near the top. This radial circulation is shown on the middle panels of figure 2.4, which show contours of the Stokes stream function $\psi$,

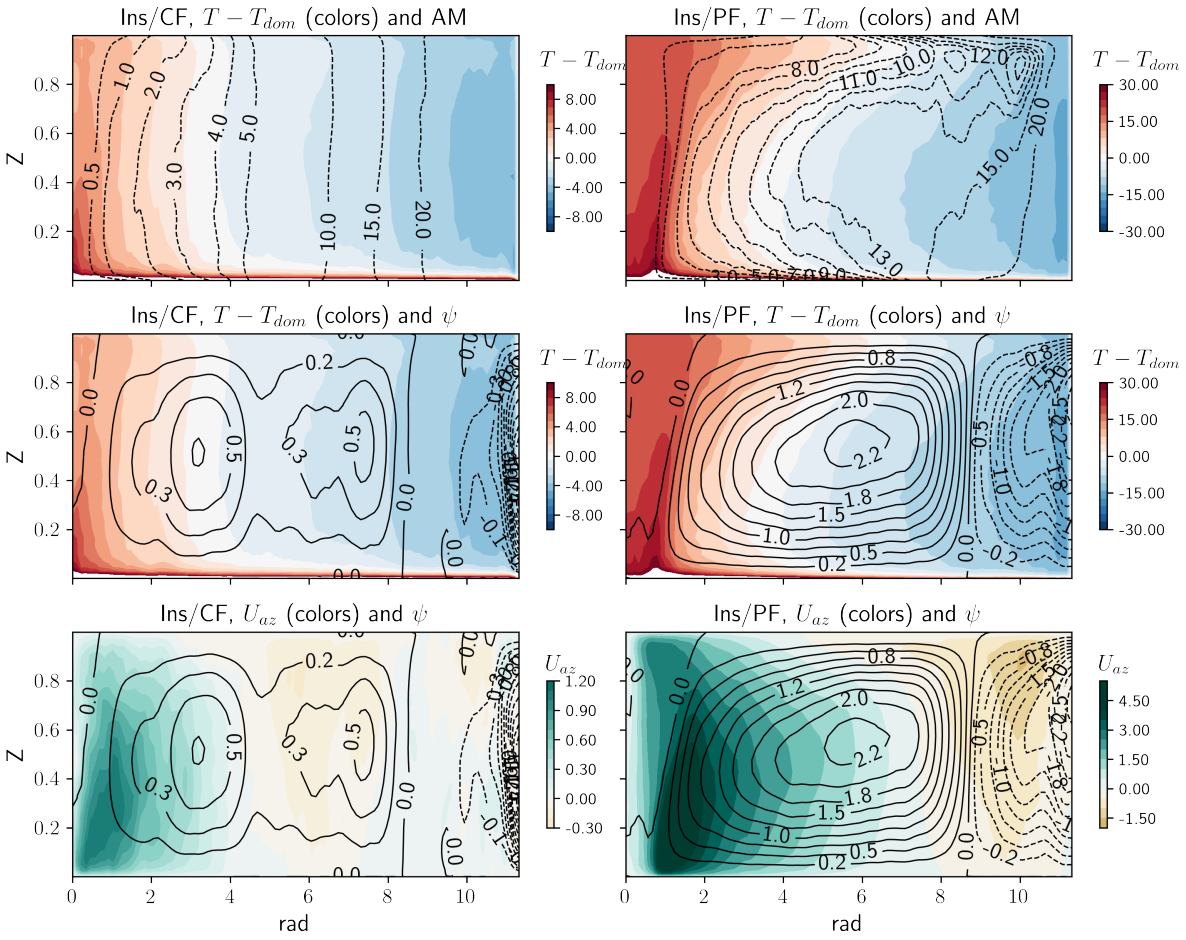


Figure 2.4: Azimuthally-averaged radius vs. height profiles centered at TC center for simulations with $\mathrm{Ro_c} = 2.0$, averaged between the 9th and the 10th rotational time period, for Ins/CF (left column) and Ins/PF (right column). Top row: $T - T_{dom}$ (color) and total angular momentum (line contours). Middle row: $T - T_{dom}$ (color) and the Stokes streamfunction (contours; see text). Bottom row: azimuthal wind (color) and Stokes streamfunction (contours). All quantities are dimensionless.

obtained by solving the system

$$u_r = \frac{-1}{r}\frac{\partial \psi}{\partial z} \tag{2.10}$$

$$w = \frac{1}{r}\frac{\partial \psi}{\partial r}, \tag{2.11}$$

where $u_r, w$ are the radial and the vertical components of the velocity, respectively. Solving the second equation for $\psi$ and prescribing the boundary condition $\psi(r = 0, z) = 0$ yields

$$\psi(r, z) = \int_{r'=0}^{r'=r} w r' dr' \tag{2.12}$$

The Stokes stream function indicates inward flow of buoyant fluid near the surface and radial outflow near the top. The near-surface flow maintains the warm core of the vortices through buoyancy advection and through inward advection of heat extracted from the surface, and is thus a crucial part of their energy cycle. We note that the lower inflow and upper outflow branches could be characterized by relatively constant pressure and an increase/decrease in temperature respectively, while the ascent and descent are closer to isothermal. However, a direct comparison between the different branches of the thermodynamic cycle associated with the circulation in Ins/PF or Ins/CF with more realistic conditions in the atmosphere, even in the absence of phase changes, is challenging, since cooling and compression are decoupled from each other in a Boussinesq system, and the thermodynamic efficiency cannot be defined based on a ratio of absolute temperatures.

For Ins/CF, the radial circulation of the chosen vortex spans radially out to about 5 dimensionless units, beyond which a combination of the secondary cyclone and the background flow are picked up. Since for Ins/PF there is only one vortex, and so only one axis of flow symmetry in the domain, the secondary circulation shows an unambiguous signal that spans out to about 8 or 9 dimensionless units, suggesting that the vortex size is domain-limited. This is consistent with the finding that, for more realistic TC simulations, the vortex can form in domains that are too small to allow for its natural length scales, in which case it grows as much as the domain allows (Chavas & Emanuel, 2014).

The bottom-heavy spatial structure of the azimuthal winds, consistent with the balanced

flow around a warm core, is also a quintessential feature of tropical cyclones. The lowest panels of figure 2.4 show profiles of azimuthal winds (colors) and the Stokes stream function (black lines). The maximum azimuthal winds of both vortices are found near the surface and close to the center of the cyclones, and in Ins/PF this also corresponds to the region of strongest convection as indicated by the slanted, densely packed streamlines, demarcating the boundary between the eye and the eyewall. Additionally, an upper-level anticyclone is sustained at the top. The general structure of the winds in Ins/PF is very similar to that found in previous studies of dry TCs (Cronin & Chavas, 2019; Mrowiec et al., 2011; Wang & Lin, 2020). That of Ins/CF is qualitatively similar, although the strength and the degree of axisymmetry are lower.

The radial profile of winds in Ins/CF and Ins/PF at 20 percent of domain height—approximately the depth of the strongest azimuthal winds for both—shown in figure 2.5 also makes more apparent some of the differences between the two TCs: while the presence of both vortices is discernible from the azimuthal winds, the total winds (blue curve) within the vortex in Ins/CF are not substantially stronger than those far away from it, unlike for Ins/PF, where the total winds of the vortex are enhanced substantially by the wind-dependent heat flux parameterization. Additionally, the increase in the magnitude of the radial winds with radius near the cyclone center, which by continuity indicates the region of highest convergence and strongest convection, is sharp and well-defined in Ins/PF, extending between about $1.2 < r < 2$, whereas it is less steep and broader in Ins/CF, going from $r = 2$ all the way to the center, consistent with a less clear eyewall region.

The red line in figure 2.5 corresponds to the model of wind structure proposed by Emanuel and Rotunno (2011)—ER11 henceforth—in its asymptotic solution. This model was developed to represent the inner convecting region of moist TCs, and can be matched with a separate solution for the outer, non-convecting region (Chavas et al., 2015; Cronin, 2023). However, for dry TCs, the solution for the non-convecting region is not needed (Cronin & Chavas, 2019). Equation (36) of ER11 gives the ratio of angular momentum to the reference value at the location of maximum winds:

$$\left(\frac{M}{M_m}\right)^{2-(C_E/C_D)} = \frac{2(r/r_m)^2}{2-(C_E/C_D)+(C_E/C_D)(r/r_m)^2}, \tag{2.13}$$

where $r_m, M_m$ are the location of maximum azimuthal winds and the angular momentum at that location, respectively, $C_E$ is the enthalpy exchange coefficient, and $C_D$ the drag coefficient. Assuming $C_E = C_D$ for illustrative purposes as ER11 do, and substituting the values of angular momentum, equation 2.13 yields

$$u_{az}(r) = \left(\frac{2}{r}\right)\left(r_m v_m + \frac{r_m^2}{2\mathrm{Ro_c}}\right)\left(\frac{\left(\frac{r}{r_m}\right)^2}{1+\left(\frac{r}{r_m}\right)^2}\right) - \frac{r}{2\mathrm{Ro_c}}. \tag{2.14}$$

where quantities have been non-dimensionalized by the convective velocity scale and the domain depth. The outer radius $r_o$ for which $u_{az}(r_o) = 0$ obtained from equation 2.14 is given by $r_o = r_m\sqrt{4\mathrm{Ro}+1}$, where Ro is the local Rossby number, $\mathrm{Ro} = \mathrm{Ro_c}(v_m/r_m)$. Substituting the values of $v_m$ and $r_m$ found in our simulations, we obtain $r_o = 7.0$ for Ins/PF, and $r_o = 2.7$ for Ins/CF. For comparison, taking the spectrally-weighted mean wavelengths $L_{U_{20}}$ as a rough measure of the diameter of the vortices gives radii estimates of 6.6 for Ins/PF, and 3.4 for Ins/CF. The wind profile of the theoretical model with the assumed ratio $C_E/C_D = 1$ captures the extent of the outer radius of the TC in Ins/PF quite well, and somewhat well for Ins/CF. For the winds outside of the radius of maximum winds, the profile of azimuthal winds predicted by the model also shows quite good agreement with the simulated profile for Ins/PF, but less so for Ins/CF (where the vortex is less axisymmetric).

The fact that Ins/CF produces long-lived, large-scale vortices in the absence of dependence between surface heat fluxes and the flow above (i.e. without WISHE) agrees with the finding that WISHE is not required to produce large-scale, persistent (albeit weaker) TCs in realistic simulations (Chavas, 2017; Montgomery et al., 2015). Importantly, the storm produced in Ins/PF, where WISHE is active, intensifies more quickly and reaches substantially stronger winds than those in Ins/CF, which is also in line with findings about real-world storms (Chavas, 2017; Zhang & Emanuel, 2016).

The winds in the innermost core (i.e. inwards from $r_m$) in Ins/PF are poorly represented by ER11, likely due to the frontogenetic nature of the region and the breakdown of the assumptions of the model there. For similar reasons, the apparent good agreement between the model and the simulated wind speeds in the innermost core in Ins/CF is likely a coincidence, rather than evidence of the skill of the theory. Additionally, the lack of a parameterization

for the drag in our simulations, as well as the simplified form of our enthalpy-flux enhancement, make it challenging to determine the appropriate value of $C_E/C_D$ to use for a more rigorous comparison with the model.

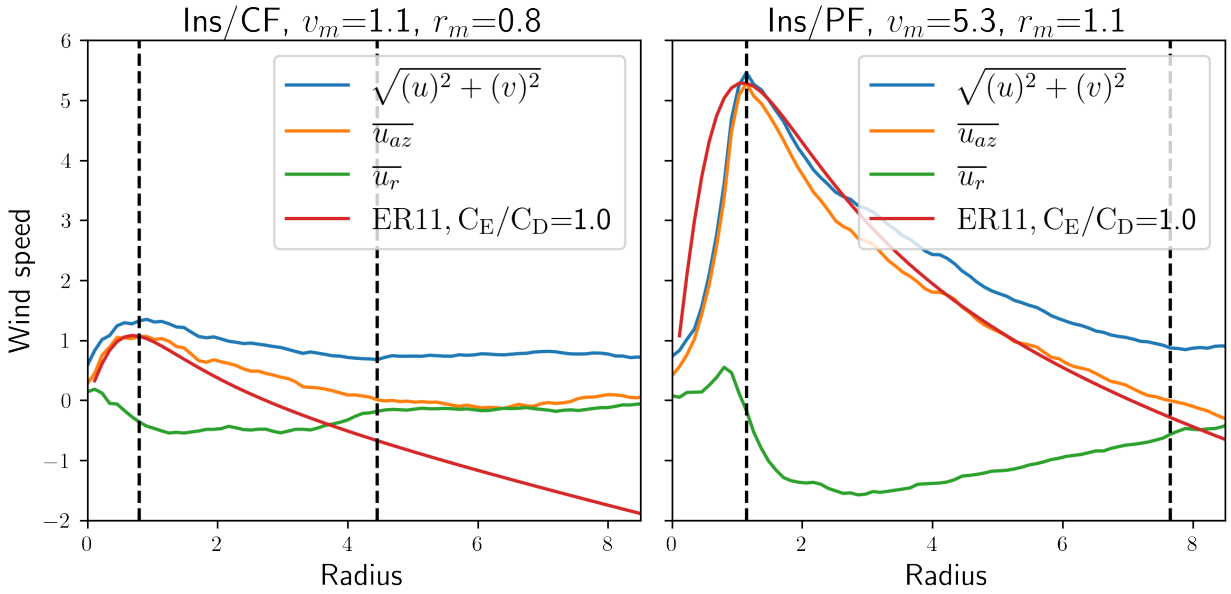


Figure 2.5: Radial profiles of azimuthally-averaged wind speed at 20 percent of domain height for vortices in Ins/CF (left) and Ins/PF (right). Plots show total winds (blue), azimuthal winds (orange), radial winds (green), and the azimuthal wind profile based on the model by Emanuel and Rotunno (2011), denoted by ER11, using $C_E/C_D = 1$ (red; see text for details). $v_m$ and $r_m$ indicate the maximum azimuthal wind speed ($\max(\overline{u_{az}})$) and the radius of maximum winds, respectively. Dashed vertical lines indicate $r_m$, and the innermost location where azimuthal winds drop below 0.01.

### 2.4.3 Rotation rate and TC formation

The Ins/PF setup produces the circulation with the clearest resemblance to a TC, which makes it a suitable candidate to investigate the response of TC characteristics to changes in the governing parameters. Particularly, a faster rotation rate has been shown to lead to a smaller size for equilibrated TCs on an f-plane (Wang et al., 2022), but it is unclear if this scaling breaks down at a particular rotation rate or convective strength. Since the convective Rossby number quantifies the relationship between rotation and convective strength, we perform an additional suite of simulation to study the dependence of vortex characteristics on $\mathrm{Ro_c}$ for Ins/PF boundary conditions. The results are shown in figure 2.6. All simulations

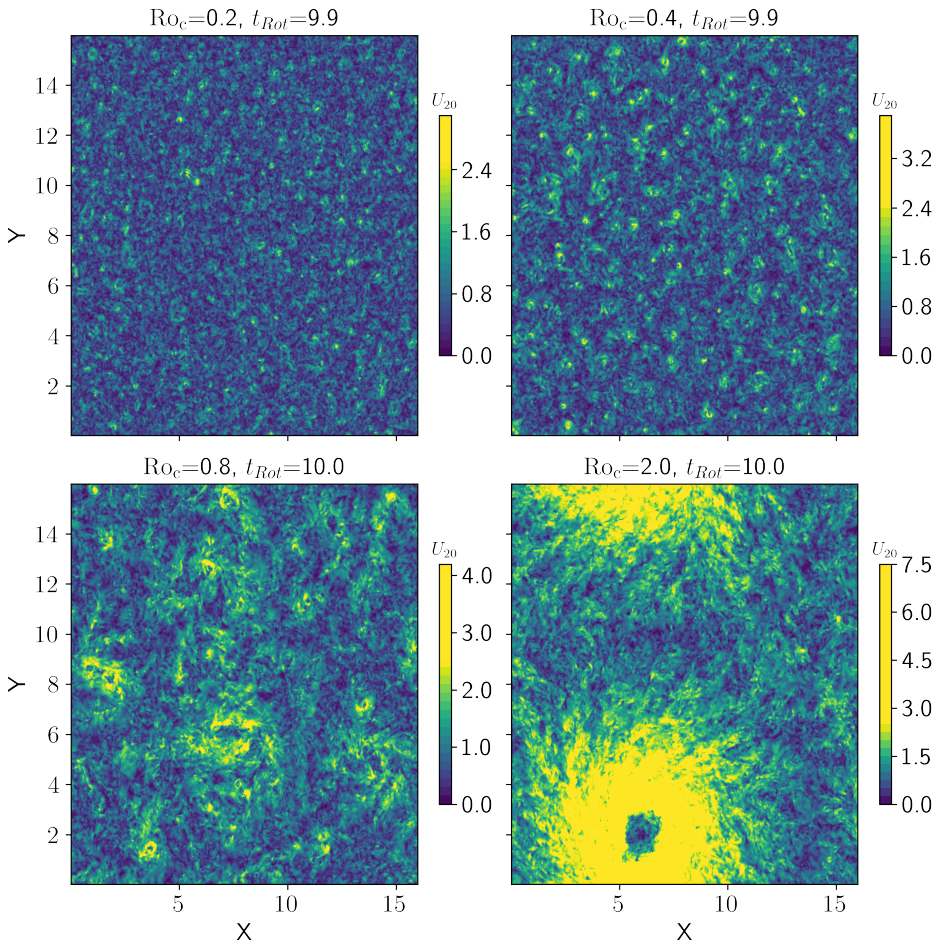


Figure 2.6: Plan views of horizontal wind speeds at 20 percent of domain height for simulations with Ins/PF conditions, for various values of $\mathrm{Ro_c}$, at 10 rotational time periods from the start of the simulations. The values are dimensionless and scale with the convective scale. Colors saturate at a value of $U = 2.5$.

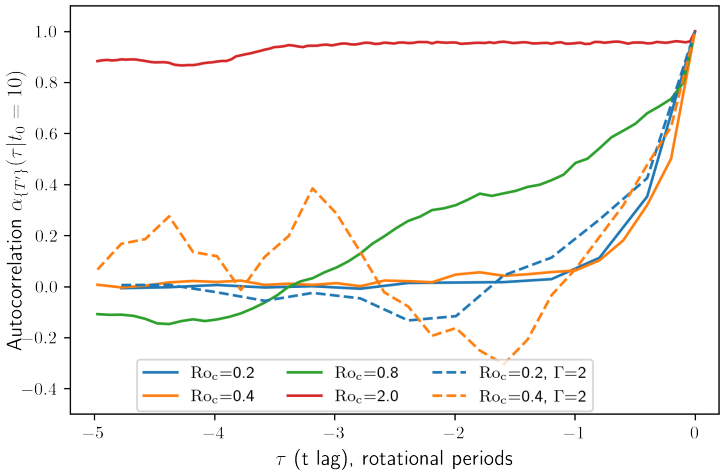


Figure 2.7: Temporal autocorrelation of vertically-averaged temperature anomaly $\{T'\}$ for the four simulations of figure 2.6 (solid lines), and two additional simulations (dashed lines), with domain aspect ratio of 2, and Rossby numbers of 0.2 and 0.4.

produce vortices of some sort, although only that in the simulation with $\mathrm{Ro_c} = 2.0$ persists for much longer than a rotational time period, suggesting a qualitatively different behavior, and a threshold around $\mathrm{Ro_c} \sim 1$ for the formation of proper TC-like structures. The intensity and the size of these vortices is affected by the rotation rate as well, with the latter seeming to scale roughly with $\mathrm{Ro_c}$.

The structure and the persistence of the vortices for the lowest $\mathrm{Ro_c}$ simulations differ markedly from those with $\mathrm{Ro_c} = 0.8$ and, especially, $\mathrm{Ro_c} = 2.0$. Figure 2.7 shows the temporal autocorrelation of the temperature anomaly field for the same suite of simulations as figure 2.6, spanning five rotational time periods, starting at least four rotational periods after the initialization. In addition to these, the figure includes two simulations with lower aspect ratios. The high autocorrelation found for the simulation with $\mathrm{Ro_c} = 2.0$ shows evidence that the large, highly-axisymmetric vortex that forms in it, or more precisely its associated pattern of convection and its warm core, is persistent in time and fixed in space.

We note that the temporal autocorrelation of temperature anomaly is not a perfect metric for the persistence of vortices if those are drifting in the domain. However, the small vortices for small $\mathrm{Ro_c}$ in fact do not persist for much longer than a rotational period (see video 2 referenced in Appendix A). Additional simulations were run with $\Gamma = 2$ , in order to test if the lack of persistence of the small vortices was associated to the size of the domain. Figure

2.7 shows that the autocorrelation does not exhibit a consistent increase. These simulations thus indicate that it is not enough for the domain to tightly contain a vortex—as in a "lattice equilibrium", borrowing the terminology of Zhou et al. (2014) for a doubly periodic domain that contains exactly one vortex—for it to be persistent in time, if the convective Rossby number is too low. All of this is evidence of a fundamental difference between the TC-like structure seen for $\mathrm{Ro_c} = 2.0$ and the small, evanescent structures of $\mathrm{Ro_c} = 0.2$ and 0.4.

The convective Rossby numbers for Ins/PF used here are based on the same scaling used for Ins/CF. That means that, instead of re-defining the buoyancy flux based on the changing bottom flux, we take a fixed reference flux $F_B$, which has an associated velocity scale that is constant. Because this scale does not include the enhancement of the heat flux by the flow, we cannot expect the typical dimensionless wind speeds in the domain to scale with it. There will thus be an effective convective Rossby number, $\mathrm{Ro_{c,eff}} = \mathrm{Ro_c}\,(1 + C_k U_h)^{1/3}$ which gives a more accurate bulk characterization of the flow in the domain than $\mathrm{Ro_c}$. This effective Rossby number cannot be determined a priori, since it depends on the horizontal wind speed, which in turn depends on the heat flux. However, we can calculate it from the values of $U_h$—the horizontal wind speed at 1 percent of domain depth used in our simple parameterization PF. We obtain $\mathrm{Ro_{c,eff}} = 0.23, 0.47, 0.91$ for the simulations with $\mathrm{Ro_c} = 0.2, 0.4, 0.8$, respectively, for which $U_h$ stays fairly constant throughout the simulation. For the simulation with $\mathrm{Ro_c} = 2$, we obtain $\mathrm{Ro_{c,eff}}$ starting at around 2.34 and stabilizing at about 2.45 once the TC has equilibrated. These differences are not negligible, but the fact that they are small indicates that $\mathrm{Ro_c}$ approximately characterizes the bulk properties of our Ins/PF simulations.

The convective Rossby number can be understood as the ratio of the time scale of domain rotation to the time scale of convection. The condition $\mathrm{Ro_c} < 1$ thus corresponds to situations where the depth of penetration of convective thermals is constrained by rotation. While the vertical velocity is not affected by Coriolis, the horizontal convergence and divergence associated with it is, and this affects the rest of the circulation via the pressure gradient and continuity. This constraint causes a reduced ability of convective thermals and plumes to sustain a stable warm core against the destabilizing effects of the internal cooling, which we see as a likely cause for the impermanence of the vortices formed.

Additionally, for a given convective velocity scale, a larger convective Rossby number represents a slower rotation rate, which, as mentioned, is associated with a larger storm at equilibrium (Wang et al., 2022). This suggests that in order to generate storms for higher convective Rossby numbers, larger aspect ratios would likely be needed. For moist RCE simulations, (Zhou et al., 2014) have shown that mature TCs only reach sizes that are domain independent if the domain aspect ratio is large enough, but that domain-size limited TCs form for significantly smaller domains.

We have run additional simulations with reduced horizontal resolution and large aspect ratios in the Ins/PF setup to test the effects of $\Gamma$ on TC size and formation (see Appendix A, figures A.5 to A.10). A large, TC-like vortex forms for ($\mathrm{Ro_c} = 2$; $\Gamma = 32$), still spanning the entire domain, which indicates that the storm has likely not reached its natural length scale. Similarly, ($\mathrm{Ro_c} = 3$; $\Gamma = 32$) also produces a domain-spanning TC-like vortex, but with a significantly narrower eye. The smaller eye for larger $\mathrm{Ro_c}$ is qualitatively consistent with the model by (Chavas et al., 2015) and (Chavas & Lin, 2016), which shows a narrowing of the eye for lower rotation rates when the outer size is fixed—a condition imposed in our case by the domain size limitation—as fluid parcels must travel further inwards to reach a given maximum tangential wind speed.

Other simulations performed also suggest a lower bound for the domain aspect ratio for a given convective Rossby number, below which no TC-like structures are observed: ($\mathrm{Ro_c} = 4$; $\Gamma = 32$) did not produce any persistent, large-scale vortices within more than 20 rotational periods simulated, and neither did $\mathrm{Ro_c} = 2$ or $\mathrm{Ro_c} = 3$ at either $\Gamma = 4$ or $\Gamma = 8$. It remains an avenue for future research to determine whether this lack of formation is due to a dynamical threshold to the domain size that can support a TC for a given convective Rossby number, or caused by insufficient resolution to simulate a narrowing eye adequately for slower rotation rates.

### 2.4.4 Thermal profile

A feature shared by all simulations with a flux-based top boundary condition is a horizontally-averaged temperature profile with a stable layer in the upper half of the domain, as seen in figure 2.8. The strength of this bulk inversion varies between the simulations, and is most

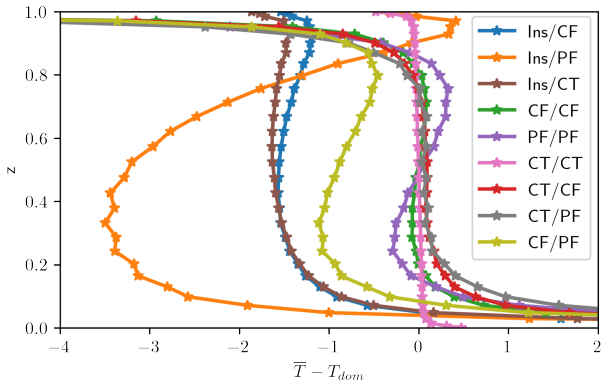


Figure 2.8: Vertical profiles of horizontally-averaged temperature minus domain-averaged temperature, $\overline{T} - T_{dom}$, for all 9 original simulations with $\mathrm{Ro_c} = 2.0$ after 10 rotational time periods. Setups with flux-based upper boundary condition (i.e. Ins/PF, CF/PF, Ins/CF, PF/PF, CF/CF and Ins/CT) show thermal inversions in the upper half of the domain.

pronounced for Ins/PF, followed roughly in order by CF/PF, Ins/CF, PF/PF, Ins/CT, and CF/CF, while none of the simulations with fixed temperature at the top show it. This feature can result from the fluid in the upper layers having been more recently in contact with the bottom surface than the fluid of the middle layers. In a framework with prescribed internal cooling, the situation is equivalent to saying that the fluid in the middle layers has cooled more than that of the upper layers, relative to the bottom. This plausibly explains the thermal inversion between the middle and the upper part of the domain as resulting from more effective detrainment of buoyant air at the top than in the middle.

Such stable thermal profiles imply the existence of an additional basic length scale in the system: a bulk deformation radius, or the length scale of propagation of gravity waves traveling through a layer with constant depth and constant stratification equivalent to those of the actual layers of the simulation. The buoyancy frequency is given by $N = \left(g\beta\frac{dT}{dz}\right)^{1/2}$. We can thus write the first baroclinic deformation radius, $R_D$, as a function of the buoyancy frequency, twice the rotation rate $2\Omega$, and the depth of the stable layer $H_s$ as $R_D = \frac{NH_s}{2\Omega\pi}$. This gives, for flux-based scalings,

$$R_D = \left(\frac{F_B}{H^2}\right)^{1/3}\left(\frac{H_s}{2\Omega\pi}\right)\left(\frac{dT}{dz}\right)^{1/2}, \tag{2.15}$$

where $F_B$ is the buoyancy flux. The convective Rossby number is $\mathrm{Ro_c} = \left(\frac{F_B}{H^2}\right)^{1/3}\left(\frac{1}{2\Omega}\right)$, which

gives in turn $R_D = \mathrm{Ro_c}\left(\frac{H_s}{\pi}\right)\left(\frac{dT}{dz}\right)^{1/2}$. The expression for the temperature-based scaling is analogous, with its respective definition for the convective Rossby number.

The bulk deformation radius calculated for Ins/PF is $\sim 1.0$, about three times as large as that of Ins/CF ($\sim 0.3$), and reasonably close to the scale of the radius of maximum winds, $r_m$. Previous work has shown that the deformation radius is not an accurate scale for either the outer radius or the radius of maximum winds of moist TCs in axisymmetric (Chavas & Emanuel, 2014) or in 3-D simulations on an f-plane (Cronin & Chavas, 2019; Zhou et al., 2014), and other scales, like $u_p/2\Omega$ is, where $u_p$ is the potential intensity, have been proposed. However, for the driest TCs simulated by Cronin and Chavas (2019), the deformation radius is at least as much of a plausible scaling for $r_m$ as $u_p/2\Omega$ is. This agreement between $r_m$ and $R_D$ thus holds in our simulations as well. These observations should be tested further before any physical mechanisms are invoked, but they suggest a possible link among the scale of the radius of maximum winds, the thermal stratification, and the convective Rossby number in fully dry TCs.

### 2.4.5 Boundary-condition symmetry

Among the nine basic setups studied, only four are characterized by an effective internal cooling: Ins/CF, Ins/PF, CF/PF, and Ins/CT. For Ins/CT, the cooling is prescribed explicitly to prevent the fluid from evolving towards an isothermal, quiescent state. For the other three, the effective cooling is a consequence of the flux asymmetry between the upper and lower boundaries: the fluid in the interior is constantly losing buoyancy (and in that sense is "cooling") with respect to the fluid at the bottom, while it is not gaining as much (for CF/PF) or any buoyancy at all (for Ins/PF and Ins/CF) with respect to the fluid near the top. This leads to vertical temperature profiles that are asymmetric, in the sense that $\widetilde{T(z)} \neq -\widetilde{T(1-z)}$, where $\widetilde{T(z)}$ represents the horizontal average of temperature at height z minus the domain-average temperature. This is shown in figure 2.9. The asymmetry coefficient $\alpha$ is defined as $\alpha \equiv \left(\frac{1}{N}\sum_i^N (\Delta_i \widetilde{T})^2\right)^{1/2}$, where the sum is across all $i \in \{1, 2, ..., N\}$ layers of the domain, and $\Delta_i \widetilde{T} = \widetilde{T(z_i)} + \widetilde{T(1-z_i)}$.

The case of CF/PF is of particular interest, because despite the somewhat symmetric

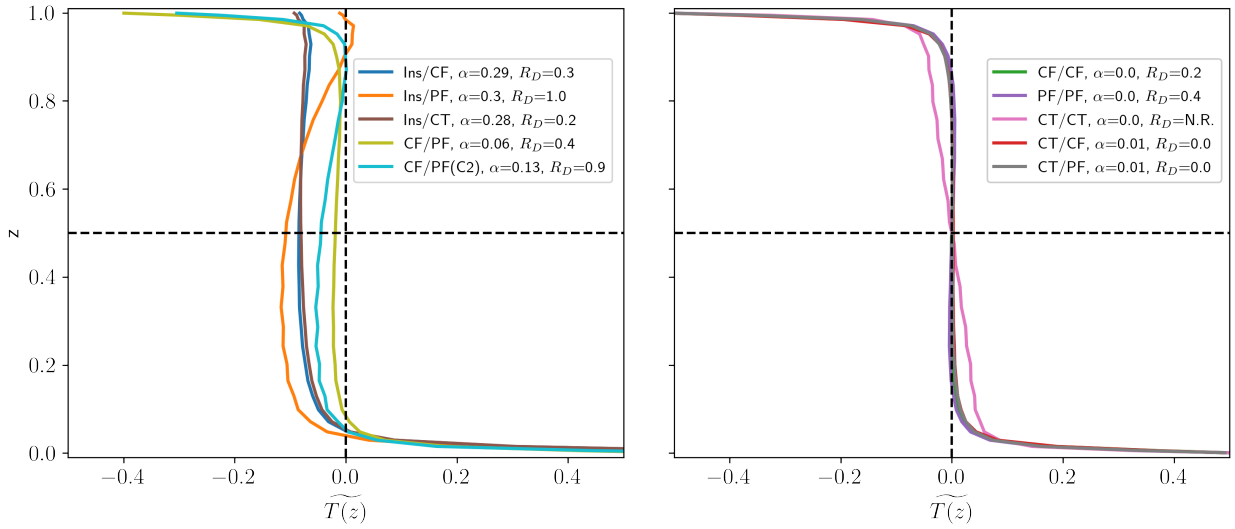


Figure 2.9: Vertical profiles of normalized, horizontally-averaged temperature, $\widetilde{T}$, for all 9 original simulations with $\mathrm{Ro_c} = 2.0$ after 10 rotational time periods, and for additional simulation with CF/PF conditions and $C_k = 2$ at the bottom, denoted by CF/PF(C2). Legend indicates the bulk deformation radius for each set of boundary conditions, as well as the asymmetry coefficient (see text for details), with "N.R." indicating simulations where no stable layer formed. $\widetilde{T}$ is calculated by subtracting the domain-mean temperature, $T_{dom}$, from the horizontally-averaged temperature at each level, $\overline{T}$, and then normalizing by the difference between the maximum and the minimum values of $\overline{T} - T_{dom}$ for each setup. Setups were divided into two groups for visual clarity: those with higher level of asymmetry are shown on the left, and the more symmetric profiles are plotted on the right.

thermal profile (with $\alpha = 0.06$) and the absence of TC-like vortices, it exhibits a strong inversion as well as the second largest deformation radius ($R_D \sim 0.4$). This raises the question of whether enhancing the thermal asymmetry sightly could potentially result in TC formation—in fact, CF/PF will approach the Ins/PF case as $C_k$ is increased to the point where the flux at the top becomes orders of magnitude weaker than the enhanced bottom fluxes. However, we find that the asymmetry need not be pushed that far in order for TCs to form: an additional simulation run with CF/PF boundary conditions, but with an enhancement coefficient $C_k = 2.0$ instead of 1.0 for the bottom parameterization (represented by CF/PF(C2) in figure 2.9) does produce a TC-like vortex after 3 rotational time periods. This indicates that either the asymmetry of the fluxes must be stronger than a given threshold for TCs to form at all, or that a stronger flux asymmetry accelerates their formation substantially, as for $C_k = 1.0$ none form within 10 rotational periods (see figure 16 in the Supplement for a comparison between the two values of $C_k$).

The other setup with internal cooling that does not produce TCs, Ins/CT, is also characterized by a thermal inversion (albeit weaker than the other three) and by substantial asymmetry of the thermal profile. We are thus prevented from concluding that thermal asymmetry is a sufficient condition for TC formation in our setups in the explored parameter regime, although it is still possible that TCs would develop given a longer spin-up time. It may also be the case that the thermal forcing is not strong enough, or that the homogeneous temperature boundary condition at the bottom is less conducive to the large-scale organization of convection and this in turn affects the likelihood of formation of a TC-like structure.

From our numerical experiments, it is unclear how the flux symmetry hinders TC formation. A possibility is that, when the updrafts and downdrafts are similarly strong, an incipient warm core, necessary to sustain the TC and to activate a wind-dependent heat flux enhancement (akin to the wind-induced surface heat exchange, or WISHE) that would power its energy cycle, is more easily disrupted, for example by accelerated heat loss to the top boundary.

A warm core is an essential part of a TC, so in general, conditions that represent a net input of heat (as is the case for asymmetric fluxes) and keep convective areas relatively

persistent in space and time would be more likely to sustain TC development. Investigating if other combinations of asymmetric fluxes can produce TCs—for instance, CF/CF with constant fluxes of different values, or PF/PF with different enhancement coefficients—would help elucidate the mechanisms that disrupt TC formation, and to answer how the spatial pattern of asymmetry matters.

## 2.5 Conclusions

We have shown that thermal boundary conditions significantly affect the patterns of convection in simulations of a relatively highly turbulent ($\mathrm{Ra_f} = 10^9$; $\mathrm{Ra} = 10^{7.3}$), moderately rotating ($\mathrm{Ro_c} = 2.0$) flow in a Rayleigh-Bénard-like setup of dry convection with a large geometric aspect ratio ($\Gamma = L/H = 16$), with Prandtl number $\mathrm{Pr} = 1.0$. Particularly, we have found that setups with boundary conditions with prescribed heat fluxes produce larger-scale and more persistent organization of convection, relative to simulations with at least one fixed-temperature boundary condition.

Importantly, in simulations with asymmetric flux-based thermal boundary conditions, we find long-lived vortices that have a number of the essential characteristics of tropical cyclones: a warm core, a bottom-heavy azimuthal circulation, high levels of axisymmetry, approximate slantwise convective neutrality, and a secondary circulation of radial convergence at the bottom and divergence aloft. These structures, obtained from direct numerical simulations, are similar to the dry TCs found in previous work in 3-D simulations with atmospheric models (Cronin & Chavas, 2019; Wang & Lin, 2020). We note that rotation and persistent, large-scale organization of convection are not sufficient conditions for the formation of dry TCs.

The basic setups that produce TC-like vortices are characterized by an insulating top and either a constant or a parameterized heat flux condition at the bottom. These are analogous to setups with constant or parameterized heat fluxes at the top with an imposed internal cooling rate matching the domain-averaged rate of warming. The parameterized condition prescribes a low-level temperature gradient enhancement that depends on the overlying flow—a simplified analogue to the bulk aerodynamic formulae for enthalpy exchange used in

atmospheric models—, promoting a WISHE-like mechanism of intensification that produces the strongest, largest, and most axisymmetric TC simulated. An additional simulation with parameterized heat flux at the bottom and constant heat flux at the top also gives rise to a well-defined TC-like vortex, suggesting that a strong enough asymmetry of fluxes is conducive to TC development.

Also for the setup with insulating top and parameterized-flux bottom, which produces the clearest TC-like vortices, we find a threshold in the convective Rossby number somewhere between $\mathrm{Ro_c} = 0.8$ and 2.0. Below it, vortices are disorganized and short-lived, suggesting that faster domain rotation weakens the convection, and prevents the buoyant plumes from the bottom from sustaining an organized warm core that extends to the top of the domain.

We find that the simulations resulting in TC formation are characterized by a positive average thermal stratification in the upper half of the domain. This stable layer has a corresponding bulk deformation radius which is proportional to the convective Rossby number, and which agrees fairly well with the scale of the radius of maximum winds, particularly in the simulation with parameterized bottom fluxes. Testing whether the thermal stratification and the associated propagation of gravity waves in the upper part of the domain associated with this deformation radius are a controlling factor or merely a result of TC formation would require additional simulations with larger domain aspect ratios. Further tests would also be necessary to confirm that the radius of maximum winds for dry TCs does indeed scale with the deformation radius.

To synthesize, we have provided evidence that flux-based thermal boundary conditions promote larger spatial organization and persistence of convection in time than temperature-based conditions. In turn, flux asymmetry allows a net input of heat that, combined with temporally autocorrelated, spatially aggregated convection, seems to make it easier for rotating convection to form and sustain a warm core in a developing large-scale vortex. This process is enhanced when a mechanism analogous to a wind-induced surface heat exchange, or WISHE, is prescribed.

We cannot definitively rule out the formation of dry TC-like structures under conditions that did not produce them in our simulations, as it is possible that a stronger thermal forcing, a larger aspect ratio, a slower rotation rate, or a longer time of simulation could lead to flow

transitions that depart from our results. Confirming this would require development of a full theory of the conditions for dry TC formation. That said, this work attests to the higher propensity for development of TC-like vortices of highly turbulent setups with asymmetric heat flux conditions and a rotation rate that is slow enough for a given thermal forcing ($\mathrm{Ro_c} \gtrsim 1.0$) but fast enough for a given domain size, and for stronger and more clearly defined cyclones when WISHE-like mechanism is included, as opposed to when the surface fluxes are constant.

Although recent work by Chien et al. (2022) has found TCs in the relatively simple moist-RBC system of Pauluis and Schumacher (2010), to our knowledge, this is the first time that TCs are simulated in a dry, 3-dimensional, RBC-like setup. We would like to reiterate that our work seeks to promote a closer dialogue between the two distinct communities studying the fluid mechanics of dry convection, and the geophysical problems of convective aggregation and tropical cyclone formation, by showing that dry hurricanes can form under relatively simple conditions of rotating convection in familiar setups about which much has been learned in the past decades. Future questions to explore include, for instance, whether the most unstable modes of marginal stability for the different convective setups persist in the highly turbulent regime; how TC strength depends on the thermal forcing or the enhancement parameter $C_k$; how finite amplitude vortices behave in domains with faster rotation than $\mathrm{Ro_c} \gtrsim 1.0$; how potential intensity can be formulated for simulations without parameterizations for the momentum drag or the enthalpy exchange coefficient (such as Ins/CF), or what relationship exists between the scalings of the heat transport and the potential intensity of TCs in RBC, to name a few.

We end by noting that not all aspects of the physics of dry TCs can be extrapolated to their moist counterparts, but even exploring that distinction may produce valuable insights about the factors that control hurricanes on Earth and potentially on other planetary contexts.

# Chapter 3

# Persistent, Large-Scale Cyclonic Vortices in Rotating Rayleigh-Bénard Tank Experiments

## 3.1 Abstract

Rotating tank experiments of turbulent convection have been used for the better part of a century to study different geophysical and astrophysical phenomena. However, comparatively little attention has been devoted to recreating the conditions under which flows associated with large-scale convective organization happen in tropical and subtropical latitudes on Earth, such as tropical cyclones, heat lows, or mesoscale convective complexes. Such conditions include a relatively slow rotation rate, boundary conditions that produce top-bottom asymmetric buoyancy sources, and large geometric aspect ratios. In this work, we perform experiments of moderately turbulent, moderately rotating convection using a shallow cylindrical tank with hot water that cools off to the air above, and is insulated in its bottom and side boundaries. We find large, persistent cyclonic vortices for experiments with convective Rossby numbers $\mathrm{Ro_C} \gtrsim 1$; smaller, shorter-lived and less organized cyclonic flows for $0.6 < \mathrm{Ro_C} \lesssim 1$, and a relatively persistent, predominantly anticyclonic flow for $\mathrm{Ro_C} < 0.6$. Metrics for temporal persistence and spatial length scales based on the temporal autocorrelation and the two-point correlation, respectively, confirm the dependence of these features on the convective Rossby number, and show no substantial effect from the flux Rayleigh number after controlling for fluid depth and rotational period. These results

indicate great potential for studying convective aggregation and tropical cyclone formation from rotating convection in simple experimental setups in the absence of phase changes

## 3.2 Introduction

Fluid tank experiments have been used extensively in the study of thermally-driven convection, with a notable early exponent found in the paradigmatic work of Henri Bénard (Bénard, 1901) in the early 20th century. This long-standing experimental endeavor has also incorporated the effects of rotation for the better part of a century, with rotating tank setups being used both for basic fluid dynamics and thermodynamics research, as well as astrophysical and geophysical applications (Busse, 2006). Ingenious modifications of basic convective setups like the Rayleigh-Bénard system (RBC) have been used to study real world phenomena. However, comparatively little experimental work has focused on flows associated with large-scale convective organization, such as tropical cyclones (TCs), heat lows, or mesoscale convective complexes, despite their significance in meteorology, oceanography, and climate research. This work seeks to reduce that gap by studying convective organization and large-scale vortex formation in a modified version of the Rayleigh-Bénard system subject to rotation.

Tropical cyclones are an example of large-scale [1] cyclonic flows in the atmosphere that are tightly associated with convective processes, but they are not the only one. For instance, heat lows, also known as thermal lows, defined by the Glossary of the American Meteorological Association as "[Areas] of low atmospheric pressure near the surface resulting from heating of the lower troposphere and the subsequent lifting of isobaric surfaces and divergence of air aloft", are also characterized by large-scale, albeit weaker, cyclonic circulations near the surface (American Meteorological Society, n.d.). Unlike TCs on Earth, heat lows are linked mostly to dry convection, and are driven by horizontal gradients of diabatic heating such as those resulting from land-sea contrasts (Rácz & Smith, 1999). However, similar to TCs, they are warm-core structures (Spengler & Smith, 2008), and their circulations are also

[1] We use the term "large scale", as in the fluid dynamics literature, to denote spatial scales substantially larger than the typical width of convective thermals or plumes. This use differs from the custom in meteorology, where it most often denotes scales of thousands of kilometers.

powered by surface enthalpy fluxes (Johnson, 2003). As these properties suggest, heat lows are similar in many respects to dry TCs found in numerical simulations (Cronin & Chavas, 2019; Mrowiec et al., 2011; Velez-Pardo & Cronin, 2023; Wang & Lin, 2020), except that they are governed by horizontal heterogeneities in the thermal boundary conditions. Because of the absence of irreversible phase changes, both heat lows and dry TCs are thus easier to study in more typical setups of rotating Rayleigh-Bénard convection, compared to moist TCs.

As of November of 2023, a search of the terms "rapidly rotating convection" (under quotations) on Google Scholar returns 565 results, while "slowly rotating convection" gives 43. This simple heuristic alludes to the comparatively little attention that the slowly rotating regimes of convection have received from the scientific community, despite their relevance for many geophysical phenomena. This contrast is likely due in part to the higher non-linearity of weakly rotating convection, compared to the rapidly rotating case, where the dominant balance (geostrophy) is linear. In chapter 2, we primarily discussed previous studies based on numerical simulations of turbulent, slowly rotating regimes in RRBC. This region of parameter space has also been probed by experimental work (e.g., Brown & Ahlers, 2006; Brown et al., 2005; Fernando et al., 1991; Hart et al., 2002; Kunnen et al., 2008; Weiss & Ahlers, 2011; Zhong & Ahlers, 2010), with a substantial–though not absolute–preponderance of domain aspect ratios close to 1, and symmetric thermal boundary conditions.

Overturning circulations larger than typical convective plume widths have been found in multiple experimental studies of RBC for non-rotating (Krishnamurti & Howard, 1981) as well as for rotating, turbulent regimes (Hart et al., 2002; Kunnen et al., 2008; Weiss & Ahlers, 2011) with constant-temperature boundary conditions. These are referred to as large-scale circulations (LSC), or "mean wind", in the literature. The LSC has been shown to precess cyclonically for slow rotation rates ($\mathrm{Ro_C} \gtrsim 1$) and anticyclonically for fast rotation rates when the domain aspect ratio is wider than unity (Weiss & Ahlers, 2011). Doubts exist that the domain-spanning circulations of non-rotating setups result from similar mechanisms as the precessing wind in the rotating cases (Sreenivasan et al., 2002), although they are often referred to by the same terminology. Despite being in the right parameter regime, it is also not clear if these behaviors of the LSCs under rotation could be linked to atmospheric

phenomena, given that the boundary conditions of the latter are not symmetric.

Experimental work by Bogatyrev, 1990; Bogatyrev et al., 2006 and Sukhanovskii et al., 2016 has managed to generate large-scale cyclonic vortices in rotating convection using large tank aspect ratios and slow rotation rates, where convection is forced by a circular bottom heating plate that only spans part of the tank diameter. These results are intriguing, although it remains unclear to what extent such structures are similar to tropical cyclones: the imposed horizontal thermal gradient introduces an external length scale in the flow that has no clear analogue in the case of tropical cyclone formation. However, as mentioned, horizontal heterogeneities in the thermal boundary conditions are characteristic of atmospheric heat lows, suggesting that the findings are still relevant to geophysical flows. We are not aware of any work that has recreated experimentally the conditions under which tropical-cyclone-like structures form from highly turbulent, rotating convection, in the absence of large-scale horizontal thermal gradients.

This work uses rotating tank experiments of a modified RRBC setup to study the flows observed for some of the basic parameter regimes and boundary conditions that favor large-scale convective organization and cyclonic vortices. The findings of Velez-Pardo and Cronin, 2023, presented in the previous chapter, showed that persistent, large-scale vortices, some of which share many of the characteristics of tropical cyclones, formed for suitable configurations of boundary conditions and rotation rates. This is a continuation of the effort to study different conditions under which persistent cyclonic vortices that are larger than the typical length scales of convective plumes form. In particular, we set out to characterize the flow regimes observed for moderately rotating, turbulent convection of hot water with aspect ratio $\frac{R}{H}\epsilon(6.4, 10)$, (where $R$ is the tank radius and $H$ is the water depth), in a tank that is cooling to the air above, and is bounded by insulating walls and a flat, insulating bottom.

The next sections describe the governing equations and the experimental setup and procedure, present the flow regimes found in the experiments, and discuss aspects of their spatial scale, persistence in time, and flow structure, comparing them to results from the numerical simulations of Velez-Pardo and Cronin, 2023. We conclude by outlining implications for future work and the significance of the results.

## 3.3 Methods

### 3.3.1 Experimental setup and procedure

The experiments were carried out in a tank placed over a turning table. The tank consists of an aluminium water heater pan with a diameter of 50.8 cm (20 in) and a depth of 6.25 cm (2.5 in). The inside is insulated with neoprene foam tape with a thickness of 0.95 cm (3/8 in), covered by an additional layer of polyethylene foam lined with aluminium foil, to act as a barrier to radiation as well as thermal conduction. The outside is insulated with two layers of the neoprene foam tape, and one layer of the polyethylene foam with aluminium foil. The total effective diameter of the tank is thus of about 48.9 cm. To insulate the tank edge, and to fill gaps of the inner insulation, we use a polyurethane-based insulating foam sealant. As bottom insulation, one-inch thick polystyrene pads were used. During the experiments, we wrapped a tall barrier of the polyethylene and aluminum foil foam around the tank, to serve as a wind shield to mitigate the effects from potential drafts and eddies in the room, given that the water is not in solid body rotation with the air above. A sketch and photos of the setup are depicted in Figure 3.1.

For each experiment, near-boiling water was poured into the rotating tank, and an insulating lid was placed on top. The water was spun up for at least 20 minutes, guaranteeing solid body rotation at the beginning of the experiment. The lid was then removed, the temperature probe was placed inside the water, and the side barrier was promptly placed around the tank. Black plastic dots were added to the water at 7 rotational periods, to serve as tracers of the flow at the surface. The water temperature was recorded by the probe, located near the edge of the tank, every 2 or 3 minutes, depending on the speed of rotation. Videos were recorded from the removal of the insulating lid until at least 10 rotational periods had elapsed. A total of 36 valid experiments were run, with fluid depths values of 2.5, 3.5, or 4.5 cm, and rotational periods of 35, 70, 104, 125 or 153 seconds. See all data for experiments in Table B.1 in the Appendix.

To guarantee that most of the heat is lost through the top of the setup, we can estimate the losses by conduction through the sides and the bottom. From the thermal conductivity,

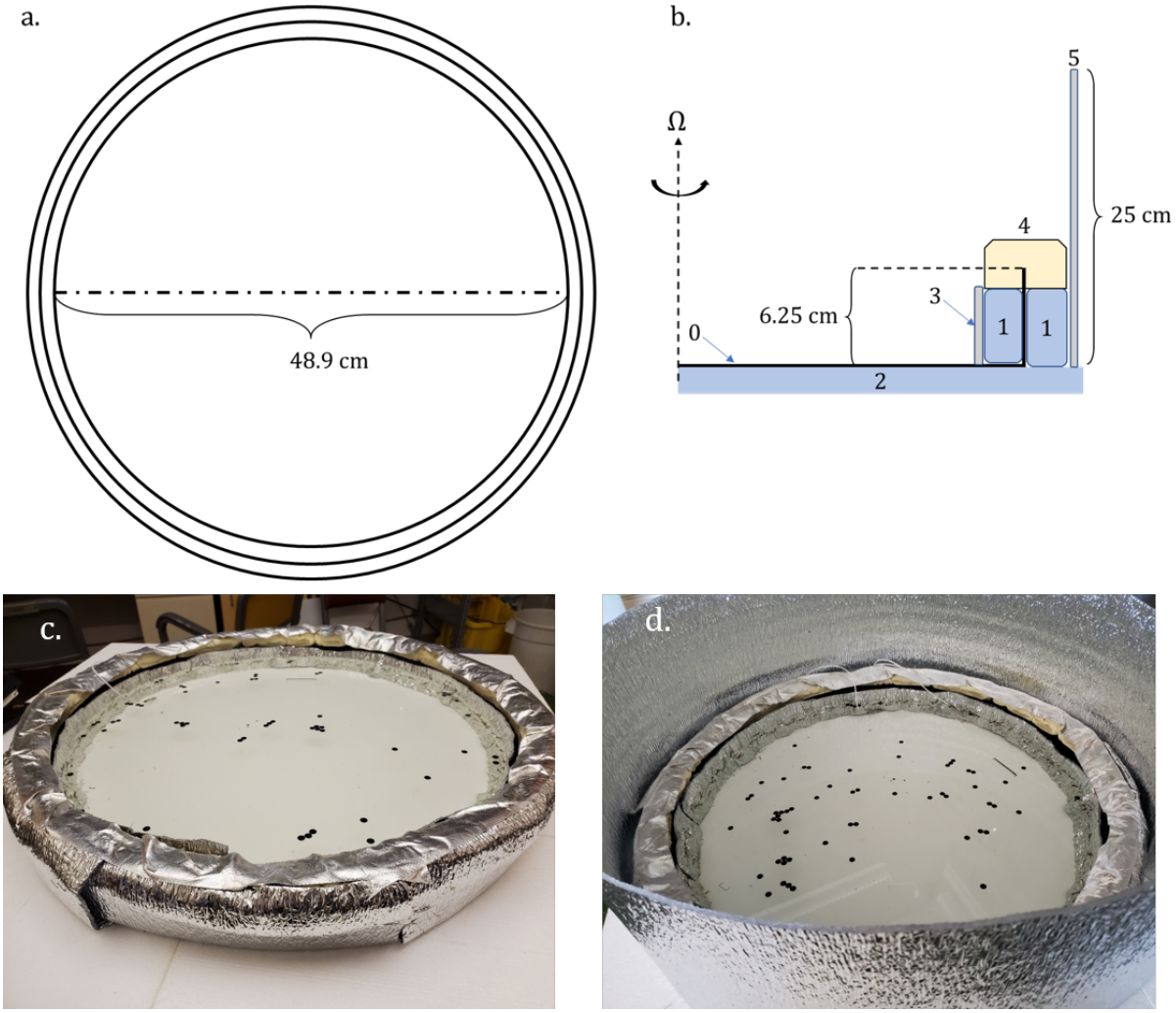


Figure 3.1: Plan view (a) and side view (b) sketches of experimental setup, and photos of setup without (c) and with wind barrier (d). Plastic tracers and insulating layers are visible in the photos. Numbers in (b) correspond to: 0. Aluminium tank, 1. neoprene foam tape, 2. polystyrene pad, 3. aluminium-foil-lined polyethylene foam, 4. polyurethane-based insulating foam sealant, 5. same as 3., used as a wind barrier.

$k$, and the thickness of the insulating layers, we first obtain the heat transfer coefficient $U$ for the sides: We use $k = 0.03$ W m$^{-1}$ K$^{-1}$ for the air-filled aluminum foil (taking the conductivity of air at standard pressure and at 350 K as representative of the material) (Incropera et al., 1996), $k = 0.055$ W m$^{-1}$ K$^{-1}$ for the neoprene foam (Moran et al., 2018), and $k = 0.04$ W m$^{-1}$ K$^{-1}$ for polystyrene (Gnip et al., 2012). Using thicknesses $\delta = 1.5, 2.8$ and 2.5 cm for each of the layers, respectively, we find $U_{sides} = \frac{a}{\frac{\delta_1}{k_1} + \frac{\delta_2}{k_2}}$, where the sub-indices 1 and 2 represent the air-filled aluminum foil and the neoprene foam, and $a$ is the ratio of the lateral area to the area of the tank (close to 0.36, for a water depth of 4.5 cm). This yields $U_{sides} \approx 0.4$ W m$^{-2}$ K$^{-1}$. Similarly, for the bottom we get $U_{bot} \approx 1.6$ W m$^{-2}$ K$^{-1}$. As will be shown later, the heat transfer coefficient of the whole setup, including the exchange at the top, lies in the range between 30 and 100 W m$^{-2}$ K$^{-1}$, which indicates that the losses through the sides and bottom are comparatively small, and most of the transfer occurs through the exposed water surface, as intended.

To track the tracers to infer flow velocities, we used the software Pytrack, developed by Tristan Abbott (Abbott, 2023), which finds the centroids of contiguous areas of black pixels and follows them frame by frame. From the track data, we used bilinear interpolation to obtain the eulerian flow field in the rotating reference frame. We averaged the flow field in time with a 2-second moving mean to smooth out noise, and we used the result for our plots and metrics.

### 3.3.2 Governing equations

Our system is well-described by the Navier-Stokes equations in Boussinesq form. As in the previous chapter, we non-dimensionalize the equations using the fluid depth $H$, the rotation rate $\Omega$, and the convective velocity scale, $W^* = (F_B H)^{1/3}$, where $F_B$ is the buoyancy flux, given by $F_B = \frac{g\beta Q}{\rho c_p}$, with $c_p$ the specific heat at constant pressure, $Q$ the heat flux at the upper boundary, and $\rho$ the density of the fluid. These give the same flux-based scalings presented in the previous chapter, namely: $\nabla \sim \frac{1}{H}, t \sim \frac{H^{2/3}}{F_B^{1/3}}, p \sim (F_B H)^{2/3}, T \sim \frac{{F_B}^{2/3}}{g\beta H^{1/3}}$. The cooling itself is incorporated through the boundary conditions, detailed in the next subsection.

The dimensionless equations become:

$$\frac{\partial \vec{u}}{\partial t} + \vec{u} \cdot \nabla \vec{u} + \frac{1}{\mathrm{Ro_c}} \hat{e}_3 \times \vec{u} = -\nabla p + T \hat{e}_3 + \left( \frac{\mathrm{Pr}^2}{\mathrm{Ra_F}} \right)^{1/3} \nabla^2 \vec{u} \tag{3.1}$$

$$\nabla \cdot \vec{u} = 0 \tag{3.2}$$

$$\frac{\partial T}{\partial t} + \vec{u} \cdot \nabla T = \frac{1}{(\mathrm{Ra_F Pr})^{1/3}} \nabla^2 T, \tag{3.3}$$

with $\mathrm{Ra_F} = \frac{Q \beta g H^4}{c_p \rho \nu \kappa^2} = \frac{F_B H^4}{\nu \kappa^2}$ the flux Rayleigh number, which can be seen as the ratio of the time scales of diffusive to convective thermal transport, and $\mathrm{Pr} = \frac{\nu}{\kappa}$ the Prandtl number, or the ratio of the kinematic viscosity to the thermal diffusivity. The convective Rossby number, $\mathrm{Ro_c} = \left(\frac{F_B}{H^2}\right)^{1/3} \cdot \frac{1}{2\Omega}$, represents the ratio of the timescales of rotation to convection. We set out to explore the slowly rotating ($\mathrm{Ro_C} \lesssim 1$ and $\mathrm{Ro_C} \gtrsim 1$), turbulent $\mathrm{Ra_F} > 10^8$ regime, similarly to the previous chapter. For temperatures between 50 and 90 Celsius, the Pr for water varies between 3.5 and 2 (Lemmon, 2010), but we do not analyze its implications.

In our setup, there are radiative, sensible, and latent heat fluxes at the top. Establishing a priori the value of the heat flux, $Q$, would thus require models for all three exchange mechanisms. Models do exist for water cooling evaporatively to the air above under low-wind conditions (e.g. Adams et al., 1990). However, as an alternative to this, we opt for determining $Q$ empirically from the measured temperature drop over time, as explained below. Once we have estimates of the ranges of $Q$ for water that cools from close to its boiling temperature, we choose rotation rates that produce convective Rossby numbers in the desired ranges. Although we do not fully control the parameters as we do in numerical simulations, we can still sample broadly in the targeted regions of parameter space.

For each experiment, we approximate the heat flux as

$$Q \approx -h \frac{\Delta T}{\Delta t} c_p(T) \rho(T), \tag{3.4}$$

where $\frac{\Delta T}{\Delta t}$ is the temperature change per unit time, and $c_p(T)$ and $\rho(T)$ are the specific heat capacity and the density of water accounting for their temperature dependence. This formulation assumes that the heat lost changes the water temperature uniformly across

its depth. That is a simplification, and does not take into account small losses to the surroundings, or equally small temperature gradients within the fluid. Furthermore, it also assumes that the heat flux is constant over the time interval and across the fluid depth $H$. Based on this, we can estimate the buoyancy flux $F_B$ as

$$F_B(T) = \frac{gQ\beta(T)}{\rho(T)c_p(T)}. \tag{3.5}$$

From these, the flux Rayleigh number $\mathrm{Ra_F}$ is

$$\mathrm{Ra_F} = \frac{F_B(T)H^4}{\kappa(T)^2\nu(T)}, \tag{3.6}$$

where $\kappa, \nu$ are the thermal diffusivity and the kinematic viscosity of water. The dependence on temperature is emphasized, as we retain it in our calculations. In turn, the convective Rossby number $\mathrm{Ro_c}$ is calculated as

$$\mathrm{Ro_c} = \frac{(F_B(T)H)^{(1/3)}}{fh}, \tag{3.7}$$

where $f = 2\Omega$ is the Coriolis parameter, and the angular frequency is $\Omega = 2\pi/\tau_{Rot}$, where $\tau_{Rot}$ is the period of rotation of the tank in seconds. We calculate these values based on data for the thermophysical properties of water (Dinçer & Zamfirescu, 2016; Lemmon, 2010). The ranges of variation are shown in Figure 3.2. Notably, $\nu$ decreases sharply with $T$ while $\beta$ increases with $T$. This allows us to access considerably higher $\mathrm{Ra_F}$ at elevated temperatures, not only because of increased heat flux, but also because of the favorable change in the material properties of water.

## 3.4 Results

### 3.4.1 Flow regimes

We observe three general flow regimes in the range of parameter space covered (Figure 3.3): For experiments with $\mathrm{Ro_C} \gtrsim 1$, persistent, large-scale cyclonic circulations form. In

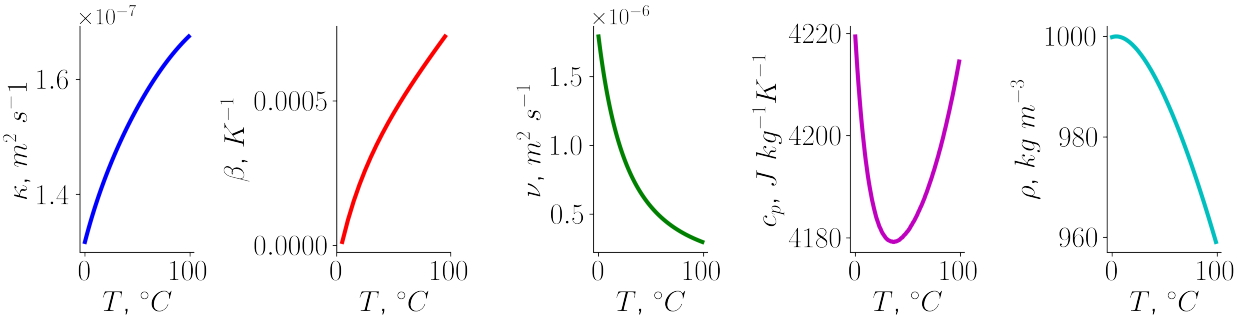


Figure 3.2: Thermophysical properties of liquid water for temperatures between 0 and 100 $°C$ at 1 $bar$. $\kappa$ is the thermal diffusivity, $\beta$ the thermal expansion coefficient, $\nu$ the kinematic viscosity, $c_p$ the specific heat at constant pressure, and $\rho$ is the density. Sources: Dinçer and Zamfirescu, 2016 for $\beta$, Lemmon, 2010 for all others. Note the widely different relative magnitudes of the changes of some of the variables with temperature.

most cases, they span a large fraction of the tank area and are significantly axisymmetric, particularly for the highest convective Rossby numbers. A substantial fraction of the vortex region in these experiments reaches flow speeds greater than the convective velocity scale $W^*$. For cases with $0.7 \lesssim \mathrm{Ro_C} \lesssim 1.0$, the flows are generally cyclonic, although their structure is more disorganized, and the flow speeds are weaker than for higher Rossby numbers. For the lowest three convective Rossby number experiments ($0.3 \lesssim \mathrm{Ro_C} \lesssim 0.6$), the flow fields are dominated by large-scale anticyclonic features, although some regions with transient cyclonic flow are still present. We argue later that these large-scale anticyclones are the result of the specific experimental setup. We observe no consistent qualitative differences in the flow over the two orders of magnitude of the flux Rayleigh number covered.

The parameters in Figure 3.3 represent the values averaged from 7 to 10 rotational periods, for which the tracer tracking was implemented. However, because the water was cooling freely to the air above, the heat flux was decreasing with time throughout each experiment, resulting in a decrease of both $\mathrm{Ra_F}$ and $\mathrm{Ro_C}$. Figure 3.4 shows the evolution of the two parameters as the experiments progressed, with the start indicated by a brown marker, and rotational period 5 by a yellow one. Because for experiments with slower rotation rates more time had elapsed since the beginning, the drop in the convective Rossby and flux Rayleigh numbers was highest. In some cases, $\mathrm{Ro_C}$ dropped by nearly 40 percent, and $\mathrm{Ra_F}$ by nearly an order of magnitude. This change of the governing parameters implies that some

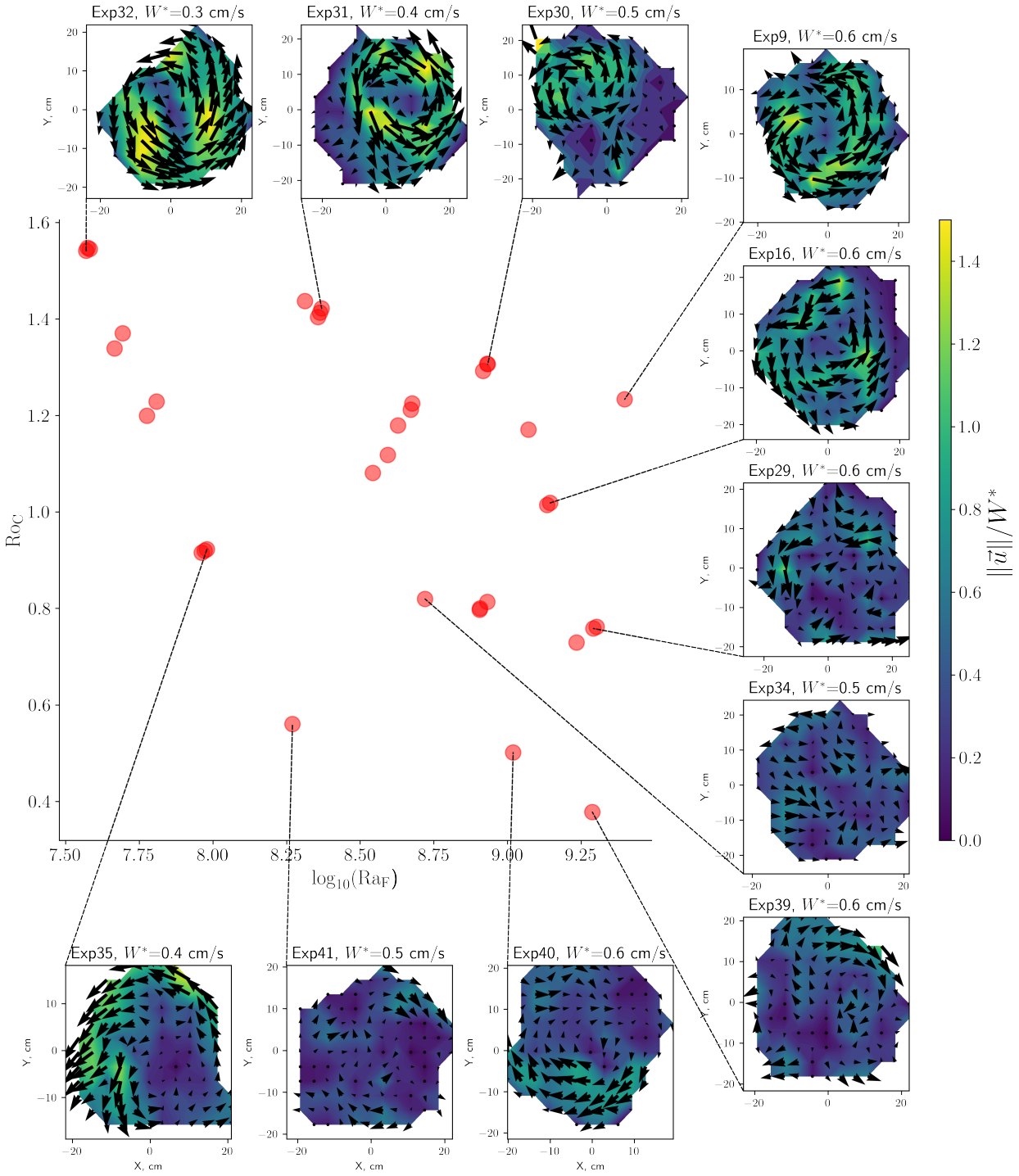


Figure 3.3: Scatterplot of $\mathrm{Ro_C}$ vs. $log(\mathrm{Ra_F})$ for the experiments, with values averaged between 7 and 10 rotational periods. Insets show the flow field for select experiments at $t = 8$ rotational periods, with color contours representing the magnitude of the horizontal flow velocity, non-dimensionalized by the convective velocity scale, $W^*$.

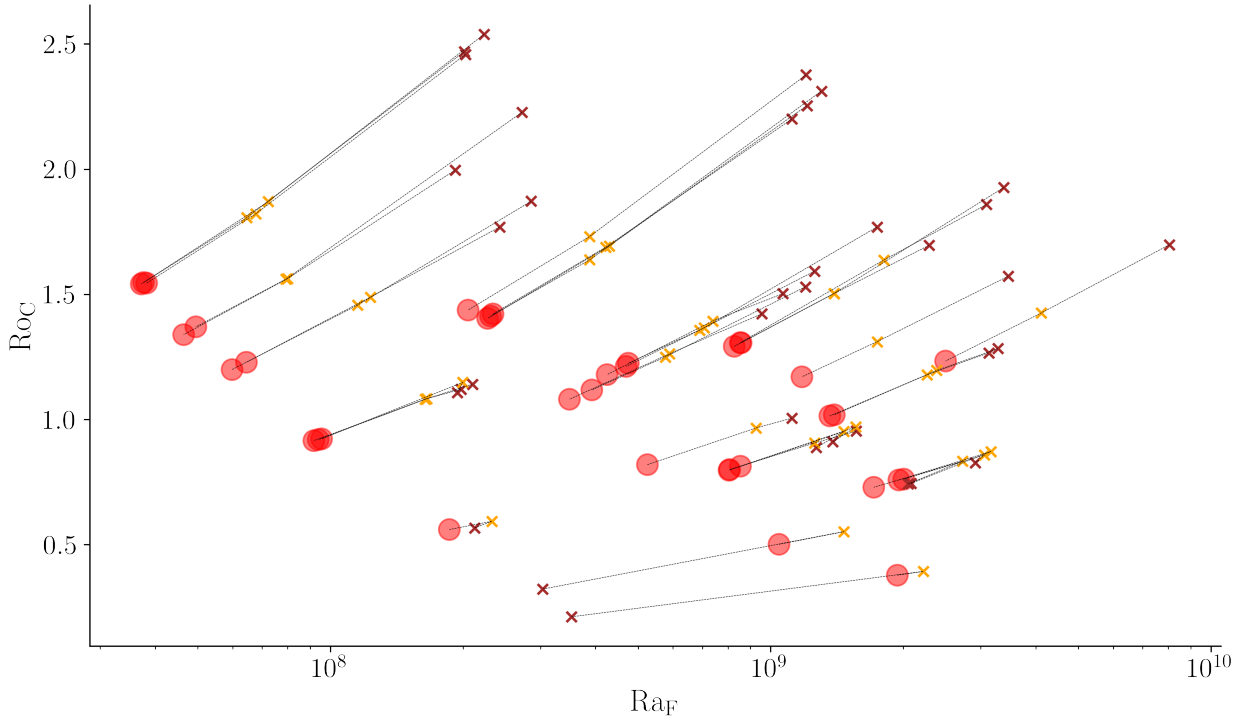


Figure 3.4: Scatterplot of $\mathrm{Ro_C}$ vs. $\mathrm{Ra_F}$ as in Figure 3.3, with 'x' markers indicating the values at the beginning of each experiment (brown) and and at $t = 5$ rotational periods.

memory of previous states might be influencing the observed circulations.

The evolution of the heat flux at different temperatures provides a sense of the similarity between the different experiments, regardless of their duration. If different rotation rates, depths, or heights of the wind barrier, have a significant qualitative impact on the heat exchange, this would result in differences in their evolution in $Q$ vs. $T$ space. However, as Figure 3.5 shows, at 5, 7 and 10 rotational periods, all experiments seem to be following largely the same trajectory. This indicates that the same thermodynamic mechanisms dominate across experimental conditions. Assuming an air temperature of 20 $°C$, the heat transfer coefficient $U$, estimated as $U = Q/\Delta T$, where $\Delta T$ is the difference between water temperature and the air temperature, ranges roughly between 30 and 100 W $\mathrm{m^{-2}}$ $\mathrm{K^{-1}}$.

### 3.4.2 Persistence and size of flow features

To characterize the persistence in time of the features in the flow fields, we use the analogue of the temporal autocorrelation used in the previous chapter, calculated based on the velocity

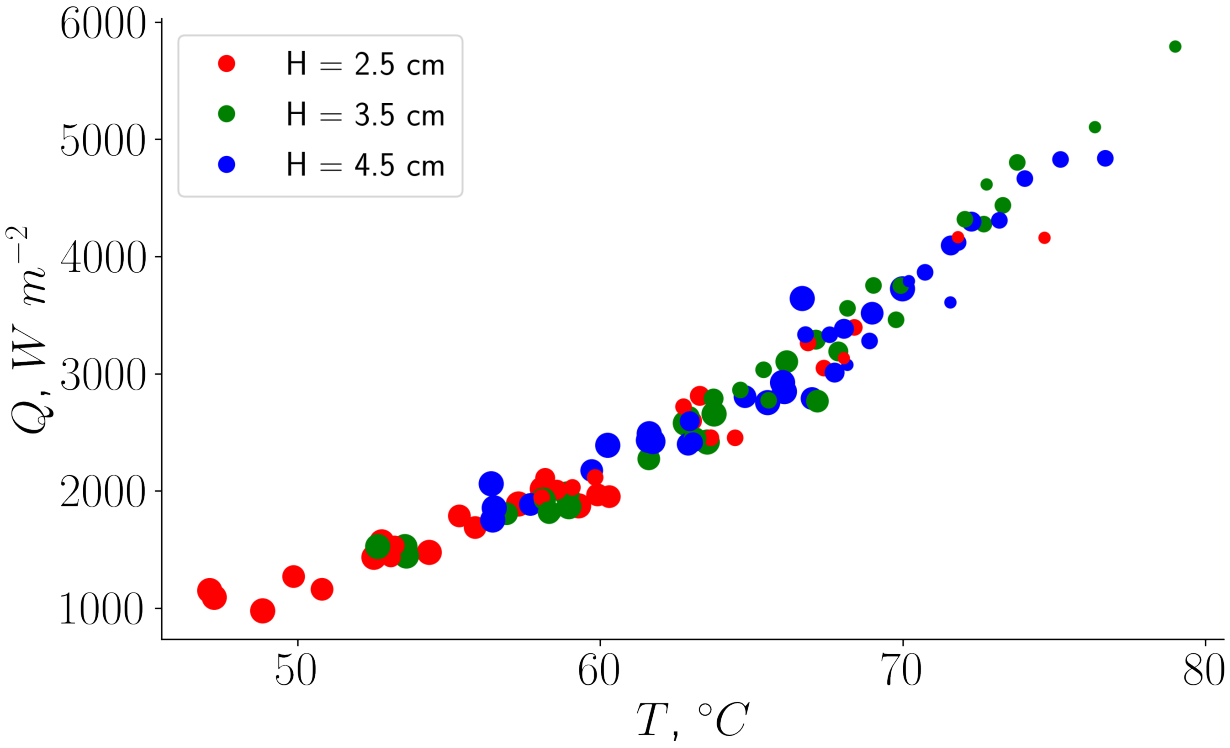


Figure 3.5: Scatterplot of the heat flux $Q$ vs. temperature $T$ for experiments at 5, 7 and 10 rotational periods. Colors denote water depth, and marker sizes are scaled based on the rotational period of the experiment (values of 35, 70, 104, 125 or 153 seconds).

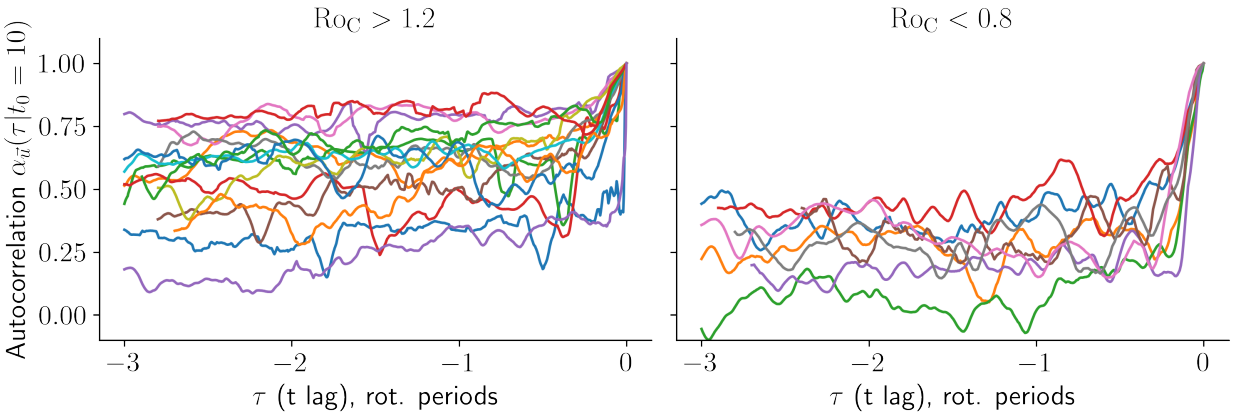


Figure 3.6: Time series of temporal autocorrelation of $\vec{u}$ at $t_0 = 10$ rotational periods, for experiments with $\mathrm{Ro_C} > 1.2$ (left) and $\mathrm{Ro_C} < 0.8$ (right). The series are smoothed with a forward rolling mean with window size 0.1 for $\tau < -0.1$, and a size of $\tau$ for $\tau \geq -0.1$.

vector, namely

$$\alpha_{\vec{u}}(\tau|t_0) = \frac{\int\int \vec{u}(t_0) \cdot \vec{u}(t_0+\tau) dxdy}{\left(\int\int \vec{u}(t_0) \cdot \vec{u}(t_0) dxdy\right)^{1/2} \left(\int\int \vec{u}(t_0+\tau) \cdot \vec{u}(t_0+\tau) dxdy\right)^{1/2}}, \tag{3.8}$$

where $\tau$ is the temporal lag, and $t_0$ represents the time of interest.

A substantial difference in the autocorrelation for experiments with $\mathrm{Ro_C} > 1.2$ and $\mathrm{Ro_C} < 0.8$ is observed (Figure 3.6), with many of the former sustaining values of more than 0.5 for the span of three rotational periods, while none of the latter do. This means that the autocorrelation metric is effectively capturing the time persistence of the large-scale cyclonic vortices observed in the high-$\mathrm{Ro_C}$ experiments.

The contrast in the autocorrelation time series between $\mathrm{Ro_C} > 1.2$ and $\mathrm{Ro_C} < 0.8$ adds to the evidence that important differences in the persistence of structures in the flow occur across a $\mathrm{Ro_C} \approx 1$ threshold. This agrees with the findings from the previous chapter, where a much faster drop in the autocorrelation was found as well, albeit for simulations with an insulating top and a parameterized-flux boundary condition (Ins/PF). This is addressed again in the discussion section.

The metric $L$ used for the length scales in the numerical simulations is not adequate for our non-periodic circular tank, so we define a metric $\Lambda$ as the $1/e$ decay length scale of the

two-point correlation $R_{\vec{u}}$ of the flow field given by

$$R_{\vec{u}}\left(r=\sqrt{(\Delta x)^2+(\Delta y)^2}\right)=\frac{\langle u(x,y)u(x+\Delta x,y+\Delta y)+v(x,y)v(x+\Delta x,y+\Delta y)\rangle}{\langle u(x,y)^2+v(x,y)^2\rangle}. \tag{3.9}$$

where angle brackets denote averaging over the area of overlap between the field and its shifted counterpart. The two-point correlation length is thus the distance $\Lambda$ such that $R_{\vec{u}}(r=\Lambda)=1/e$. This length scale is not a substitute for the radial extent of vortices, but it offers a systematic way to measure the extent of features observed in the circulation for the different experiments.

The two-point correlation length as well as the temporal autocorrelation averaged from time periods 7 to 10 show a general increase with $\mathrm{Ro_C}$ (Figure 3.7). However, the three experiments with $0.3 \lesssim \mathrm{Ro_C} \lesssim 0.6$ exhibit a larger $\Lambda$ than many of their higher-$\mathrm{Ro_C}$ counterparts, which indicates that the metric captures the presence of the large-scale anticyclones observed in the flow fields. The increase in the autocorrelation with $\mathrm{Ro_C}$ is yet clearer, with values of up to 0.7 for the highest convective Rossby numbers. The large anticyclonic features of the low-$\mathrm{Ro_C}$ experiments are less persistent in time, with $\alpha_{\vec{u}} \approx 0.4$ for them.

Experiments with the lowest $\mathrm{Ra_F}$ exhibit some of the highest values of $\Lambda$, but this is an artifact of the experimental setup and the criteria used for averaging: the reported autocorrelation and length correspond to the mean values between 7 and 10 rotational periods, which means that for experiments with shallower depths and slower rotation rates, the water in the tank had been cooling and convecting for longer than for experiments with a deeper water layer and faster rotation rates, giving the vortices more time to grow. Across experiments with the same depth and rotational period, no clear trend was observed between $\mathrm{Ra_F}$ and either $\Lambda$ or $\alpha$, although the ranges sampled under those conditions were limited.

Figure 3.7 also suggests that the largest length scales are associated with higher autocorrelation values, indicating that large-scale structures are also longer-lived. In general, the largest values of both occur for the shallowest layers and the slowest-rotating experiments, because the convective Rossby number varies directly with the period and inversely with the fluid depth.

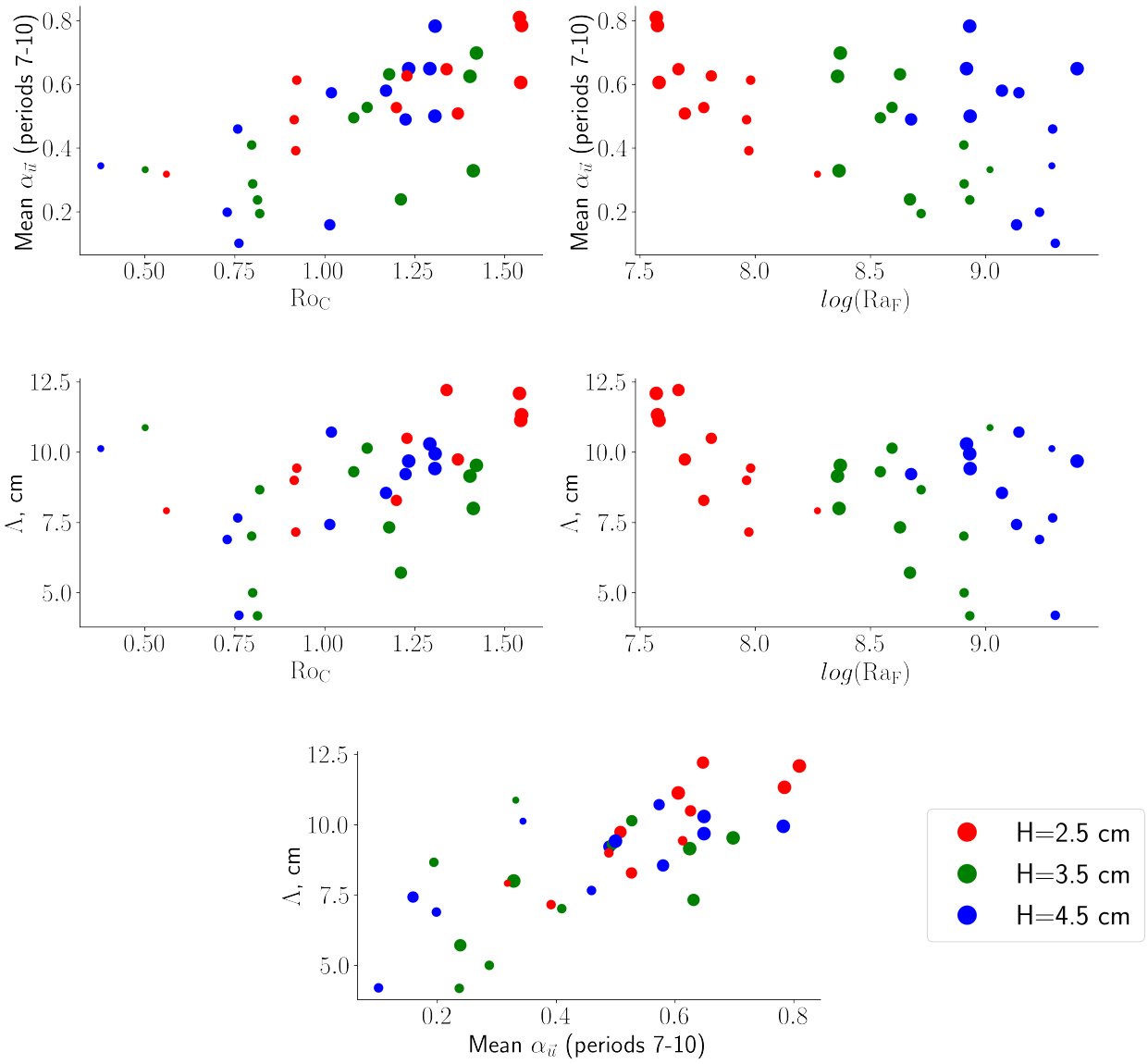


Figure 3.7: Scatterplots comparing the convective Rossby number $\mathrm{Ro_C}$, Flux Rayleigh number $\mathrm{Ra_F}$, two-point correlation length $\Lambda$, and temporal autocorrelation $\alpha$ for the experiments. The lengths and autocorrelations correspond to the mean value between 7 and 10 rotational time periods. Each marker size is scaled by the rotational period of the experiment (values of 35, 70, 104, 125 or 153 seconds).

### 3.4.3 Vortex flow profiles

We use the flow fields calculated from the tracer tracking to determine the radial profile of azimuthally averaged flows of three of the large-scale cyclonic vortices that form in experiments with the higher $\mathrm{Ro_C}$ (Figure 3.8). The difficulty in controlling the distribution of tracers means that some radii are undersampled. Despite this, the radial profiles offer a general sense of the structure of the vortices. The inferred maximum azimuthal flow speeds, non-dimensionalized by $W^*$, are close to 1, similar to the vortices in the Ins/CF simulations in the previous chapter. This suggests little to no intensification beyond the convective velocity scales. The cyclonic flows extend outwards to at least 8 dimensionless length units, spanning most of the tank area. The azimuthally-averaged radial flow ($\overline{u_r}$) profile shows the convergence associated with experiments 31 (top) and 27 (bottom), but less clearly for experiment 32 (middle), likely due to the sparsity in the tracer distribution.

We compare the radial profile of azimuthal flow with the analytic form of the theoretical model of Emanuel and Rotunno, 2011 (ER11) as in the previous chapter. Calculating the dimensionless azimuthal flow speed as

$$u_{az}(r) = \left(2\frac{v_m}{r^*} + \frac{1}{\mathrm{Ro_C}}\frac{r_m}{r^*}\right)\left(\frac{(r^*)^2}{1+(r^*)^2}\right) - \frac{r}{2\mathrm{Ro_c}}, \tag{3.10}$$

where $r^* \equiv r/r_m$, we obtain the ER11 azimuthal profiles shown in red in Figure 3.8. The agreement between the observed azimuthal flow speeds and the values from the physical model is poor, particularly for experiments 32 and 27. The azimuthal flow speeds outside of the radius of maximum flow decay more slowly with radius than ER11 predicts, similar to the case of the Ins/CF simulation. The outer radius $r_o$, calculated as $r_o = r_m\sqrt{4\mathrm{Ro_C}(v_m/r_m)+1}$ as before, gives values of $r_{o,31} = 5.3$, $r_{o,32} = 8.4$, and $r_{o,27} = 6.7$, where the subscripts indicate the experiment number. In dimensional units, these correspond to $r_{o,31} = 18.6$ cm, $r_{o,32} = 21.0$ cm, and $r_{o,27} = 16.8$ cm, all smaller than, but not too different from, the tank radius (24.5 cm). However, this partial agreement is not confirmation that the vortices are like those described by the model.

The analytic form of ER11 on equation 3.10 does not appear to characterize the vortices

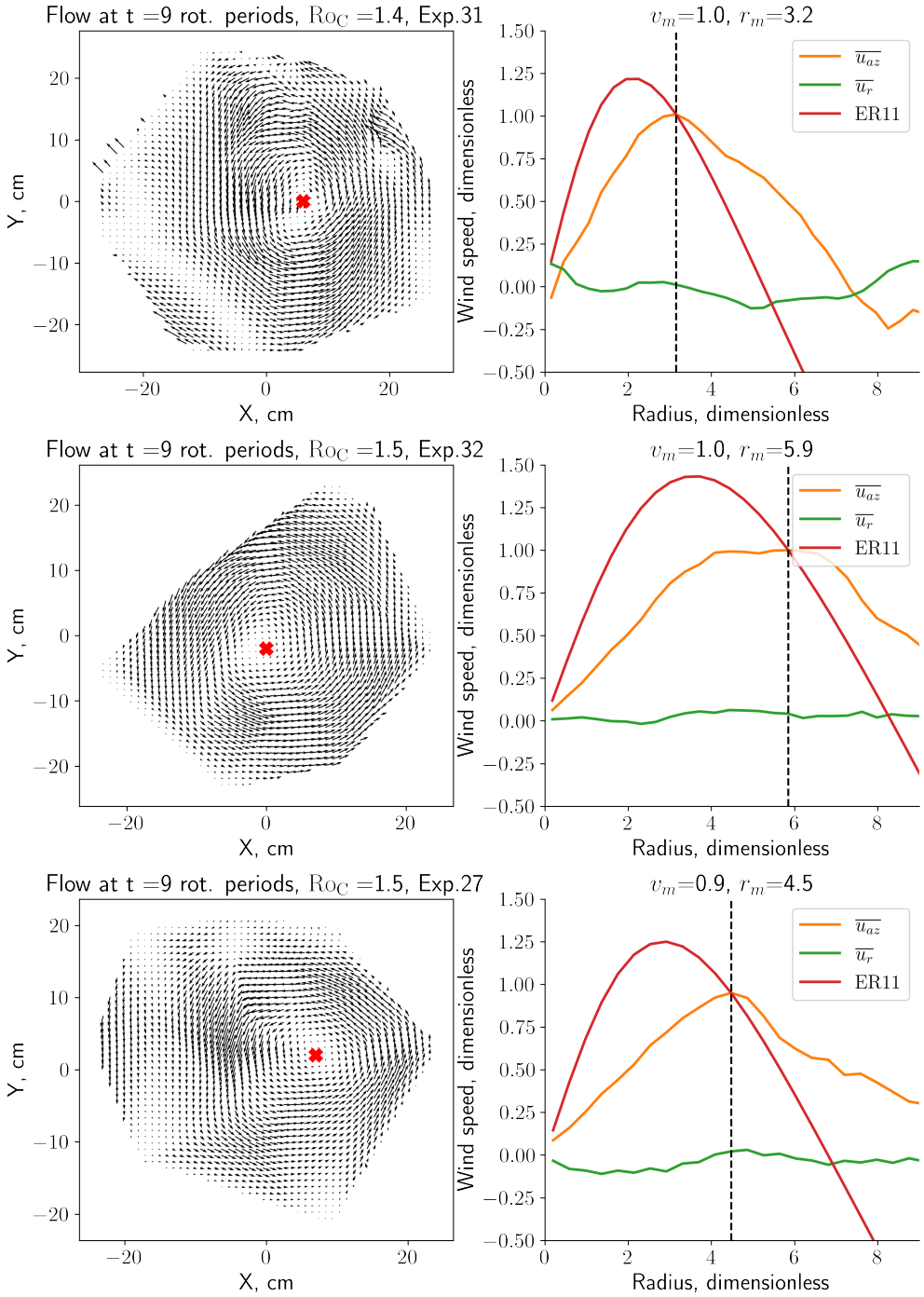


Figure 3.8: Flow field (left) and azimuthally-averaged flow profile at vortex center for select experiments with persistent, large-scale cyclones (right). The azimuthal flow speeds are in orange, the radial flow speeds are in green, and the azimuthal flow based on the model by Emanuel and Rotunno, 2011 with $C_E/C_D = 1$ is denoted in red. The maximum azimuthal flow speed $v_m$ and the radius of maximum flow speed $r_m$ and indicated in the title, and the latter is marked with black dashed lines.

found in our experimental setup. This is not unexpected, as there is likely no significant contribution from a WISHE-like mechanism enhancing the heat fluxes in our experiments, unlike Ins/PF but similar to the Ins/CF simulation setup in the previous chapter. Additionally, the analytic form of ER11 is obtained on the basis of the condition $V \gg fr$, which further explains its greater success for Ins/PF than for Ins/CF or the vortices in the tank experiments. However, the experiments also differ from Ins/CF in two important ways: first, the top (or non-insulating) boundary is free-slip, so friction does not affect the angular momentum of convergence induced by convective plumes. Second, the fluxes at the top boundary in the experiments are not guaranteed to be constant in time or spatially homogeneous. This implies the possibility that convection is heterogeneously forced, marking a difference in the mechanism driving convective organization between the simulations of the previous chapter and the tank experiment results.

## 3.5 Discussion

The formation of large-scale cyclonic vortices for $\mathrm{Ro_C} \gtrsim 1$ agrees with the findings from numerical simulations with parameterized heat fluxes (Chapter 2 and Velez-Pardo and Cronin, 2023). However, we note that the heat transport of the experimental setup is governed by the sensible and latent heat fluxes at the water-air interface, which is not the same as the simple flow-dependent heat flux parameterization (PF) or the constant-flux condition (CF) of chapter 2. For instance, the air above the tank is not in solid body rotation with the water, implying a radially dependent forcing on the flow that modulates the heat fluxes, and constitutes an angular momentum sink. Additionally, the spatial distribution of air temperature and relative humidity above the tank are likely not uniform over the water surface, although they are not monitored in our experimental setup. In the range $0.7 \lesssim \mathrm{Ro_C} \lesssim 1$, some preference for cyclonic flow is observed at the large scale for most experiments. However, the circulations do not organize into coherent, persistent vortices. This is also in line with findings for PF from the previous chapter, providing more evidence of a threshold for large-scale cyclone formation at $\mathrm{Ro_C} \approx 1$.

For convective Rossby numbers below 1, numerical simulations showed a decrease in the

size of the cyclonic features with $\mathrm{Ro_C}$, substantially less axisymmetry, as well as a significant drop in the autocorrelation. Our results confirm this trend, except for the experiments with the lowest convective Rossby numbers, namely $0.3 \lesssim \mathrm{Ro_C} \lesssim 0.6$, which are dominated by anticyclonic flow that spans most of the tank. These likely arise due to the differential wind stress with radius, and are thus a specific feature of the experimental setup: the radial gradient of azimuthal wind stress increases with an increase in the rotation rate. This leads to two effects: on the one hand, it produces a stronger enhancement of heat fluxes and convection at large radii, which, combined with the effects of friction on the bottom outflow, acts as a source of negative (anticyclonic) vorticity in the center of the tank. On the other, the simple mechanical effect of stronger wind shear towards the edges acts as a sink of angular momentum, which can also contribute to anticyclonic flow. More data about the thermal structure of the fluid would help to establish if either (or both) of these effects are causing the observed anticyclones.

The aspect ratios probed in our experiments range from $\Gamma = R/H = 6.4$ to 9.8. While more than one vortex can be seen close to the beginning of some of the higher $\mathrm{Ro_C}$ experiments, they eventually merge into one domain-spanning vortex. This suggests that the domain aspect ratios used are not enough for the cyclones to attain their natural scale. In the previous chapter, an aspect ratio of $\Gamma = 16$ was enough to produce two vortices per domain in the Ins/CF setup. If there is similarity between the two types of vortices, a slightly wider tank could be enough to allow more than one large-scale vortex to form.

As mentioned, the two governing parameters explored, $\mathrm{Ro_C}$ and $\mathrm{Ra_F}$, are not steady in time, due to the slow adjustment of the water temperatures to the environment values. This means that some memory of previous states might influence the properties of flow regimes observed at a given time, which poses a challenge in the interpretation of our experiments. However, the metrics used provide unambiguous evidence that persistent structures that are larger than the fluid depth form for convective Rossby numbers above a certain value that is close to 1, similarly to the results from numerical simulations with either constant or flow-dependent heat flux on one boundary, and an insulating condition on the other.

Unlike the setups in the previous chapter, the upper boundary in our experiments of low convective Rossby numbers is exposed to potentially important effects of shear and

horizontal gradients in diabatic forcing, due to the water moving at different speeds with respect to the air at different radii. This could explain why for the three lowest $Ro_C$, large-scale anticyclones are observed, whereas none formed in numerical simulations. If such gradients are indeed an important control on the flow at high rotation rates, the observed vortices would be dynamically similar to thermal highs—analogues to heat lows, but with an anticyclonic circulation.

It is unclear if the precessing large-scale overturning circulations of previous studies have anything to do with the circulations in our experiments. Nonetheless, experiments by Weiss and Ahlers, 2011 for $\Gamma = 1$ (which is larger than other experiments focusing on the LSC) yield a cyclonic precession of the large-scale flow at $\mathrm{Ro_C} \gtrsim 1$, while an anticyclonic precession develops for $\mathrm{Ro_C} \lesssim 1$. Even if these are unrelated to our findings, at the very least they constitute evidence of an important change in dynamical regimes of large-scale flows happening in RRBC at $\mathrm{Ro_C} \approx 1$.

We have shown that the physically-based model of Emanuel and Rotunno, 2011 for the wind structure in the convective region of tropical cyclones on Earth does not describe the flow structure of our large-scale vortices very well. This is not too surprising, given that the conditions present important differences from those for which the model was formulated. First, the thermal boundary conditions differ, because there is likely no significant flow-induced heat flux enhancement (or WISHE) in our experiments. Secondly, and perhaps more importantly, the momentum boundary conditions also differ: the upper boundary in the experimental setup, which is in contact with the air, does not experience nearly the same amount of drag as the bottom boundary on Earth, where there is a solid surface. A more thorough comparison would require re-formulating the physically-based model to take these differences into account.

## 3.6 Concluding Remarks

To our knowledge, this is the first time that large-scale cyclonic circulations are found in fluid experiments of relatively slowly rotating, turbulent thermal convection without imposed large-scale thermal gradients—the basic conditions that characterize tropical cyclone

formation on Earth, barring the inclusion of moisture and its phase changes. Using domain aspect ratios greater than unity, and top-bottom asymmetric boundary conditions, we find different flow regimes for different convective Rossby numbers, where cases with $\mathrm{Ro_C} \gtrsim 1$ yield domain-spanning, persistent cyclonic vortices, as evidenced by metrics of their size and temporal autocorrelation, those with $\mathrm{Ro_C} < 0.6$ give rise to large-scale anticyclones, and values in between those produce disorganized although generally cyclonic circulations. Previous experiments with aspect ratios close to 1 and symmetric boundary conditions report drastic shifts in the dynamics of the large-scale overturning circulations occurring at $\mathrm{Ro_C} \approx 1$, although it is unclear if this transition is related to the particular phenomena found in our experiments.

Future work characterizing the enthalpy fluxes at the top, the thermal structure of the fluid, and potentially some information about the vertical structure of the flow would help determine to what extent these cyclonic vortices are related to tropical cyclones, heat flows, or other geophysical flows.

# Chapter 4

# The Response of Tropical Rainfall to Idealized Small-Scale Thermal and Mechanical Forcing

This chapter was submitted to *Geophysical Research Letters* as Velez-Pardo & Cronin, "The Response of Tropical Rainfall to Idealized Small-Scale Thermal and Mechanical Forcing". A pre-print is available online on the ESS Open Archive. DOI: 10.22541/essoar.170000346.62539799/v1.

## 4.1 Abstract

Predicting the spatiotemporal distribution of rainfall remains a key challenge in Tropical Meteorology, partly due to an incomplete understanding of the effects of different environmental factors on atmospheric convection. In this work, we use numerical simulations of tropical ocean domains to study how rainfall responds to imposed localized thermal and mechanical forcings to the atmosphere. We use the Normalized Gross Moist Stability—NGMS—to quantify the net precipitation response associated with a given net atmospheric heating. We find that NGMS values differ considerably for different forcings, but show that the relationship between precipitation and column relative humidity collapses along a universal curve across all of them. We also show that the contributions from mean vertical advection of moist and dry static energy only approximate the NGMS well at scales larger than a couple hundred kilometers, indicating that general horizontal mixing processes are not negligible at smaller scales.

## 4.2 Plain Language Summary

Predicting where rain tends to occur in tropical areas is challenging. In this work, we simulate a small area of atmosphere over a tropical ocean to study how rainfall changes when we alter the surface temperature, the atmospheric heating rate at different heights, and the pressure gradients that drive the winds near the surface. We find that such alterations lead to self-consistent but different relationships between the amount of rainfall produced and the net heating of the atmosphere. We show that the spatial extent of the alteration affects how well this relationship can be inferred from horizontally-averaged atmospheric properties. In contrast, we find that the relationship between rainfall and the average relative humidity in the atmosphere remains the same across all types of environmental alterations.

## 4.3 Introduction

What makes it rain where it does in the tropics? Two distinct, influential paradigms often invoked to answer this question are those proposed by Lindzen and Nigam, 1987, and by Neelin and Held, 1987. Lindzen and Nigam argued that maxima in precipitation are controlled by low-level wind convergence that is mechanically forced by boundary-layer pressure gradients associated with sea-surface temperature—SST—patterns. On the other hand, Neelin and Held posited that maxima of deep convection and rainfall are regulated by a combination of the net column energy input, and the "Gross Moist Stability" (GMS) – a metric of how efficiently ascending circulations export this energy surplus. These are representative of what we refer to subsequently as "mechanical" and "column-energetic" schools of thought. These schools are united in the importance they assign to determining patterns of vertical motion, which regulate atmospheric moisture import and thus the amount by which local precipitation exceeds local evaporation. In this work, we use idealized simulations to examine the impacts of both mechanical and column-energetic (or thermodynamic) forcings on precipitation. We focus on scales ranging from tens to a few hundred kilometers, given their significant relevance for human communities and ecosystems, and the size constraints of simulations at cloud- and cloud-system-resolving scales.

The success of column-energetic arguments in accounting for large-scale precipitation patterns and zonal-mean shifts is well-documented (Bischoff & Schneider, 2014; Boos &

Korty, 2016; Donohoe et al., 2013; Marshall et al., 2014; Schneider et al., 2014). However, establishing the value of the GMS in advance poses a singular challenge for predictive uses of the column-energetic approach. Additionally, its explanatory power fails for phenomena at finer scales, for instance the behavior of the narrow East-Pacific Intertropical Convergence Zone (ITCZ) (Back & Bretherton, 2006; Sobel & Neelin, 2006), or precipitation over small islands in idealized models (Cronin et al., 2015). Furthermore, the column-energetic view does little to explain rainfall maxima over orography, which provide critical water supplies for billions of people. In these contexts, the contribution of mechanically induced convergence, ignored by column energetics, seems to play a pivotal role.

Several modeling studies have explored the sensitivity of deep convection and rainfall to forcings of different kinds. Derbyshire et al., 2004 used a CRM with adjusted drying at different heights, allowing the model to relax to a prescribed profile of relative humidity, and found that a strong drying in the mid-troposphere suppressed deep convection and led to shallow convection. Using a CRM under the Weak Temperature Gradient approximation (WTG), Wang and Sobel, 2012 found that mid- and lower-tropospheric drying led to lower precipitation than upper-tropospheric drying. In turn, Anber et al., 2015 separately prescribed heating throughout the depth of the atmospheric column, and surface enthalpy flux anomalies, and showed that, while the former led to more precipitation for forcings close to the RCE reference, total precipitation responded more sensitively to changes in surface enthalpy fluxes than to atmospheric heating, per change in $\mathrm{W/m^2}$ of forcing.

In this chapter, we study how different thermodynamic and mechanical mechanisms affect time-mean rainfall at scales of tens to a few hundred kilometers. We run numerical simulations of convection over idealized ocean domains in a CRM, where we introduce three types of forcings, illustrated in Figure 4.1:

- Localized SST anomalies,
- vertically and horizontally localized heating at different heights,
- mechanical forcing of the horizontal winds consistent with localized convergence.

We use these forcings as an idealized way of separately probing how phenomena such as aerosol-induced warming at different levels, narrow regions of high SST, or wind conver-

gence induced by orography or large-scale circulations, affect tropical rainfall patterns. We characterize the effects of the forcings, and discuss the implications of analyzing their behavior in terms of two metrics of the Gross Moist Stability, and the relationship between precipitation and column moisture. We also assess how the spatial scale of the forcings affects both rainfall and the properties of the ascending circulations over the forced patch.

## 4.4 Methods

We perform numerical simulations in radiative-convective equilibrium using the System for Atmospheric Modeling, SAM (Khairoutdinov & Randall, 2003), version 6.10.6. The basic setup consists of a domain over an ocean surface that is doubly-periodic in the horizontal, with 1024 by 32 grids in the horizontal at 3 km spacing, and a stretched grid with 64 vertical levels. We use the same parameterization schemes as Cronin et al., 2015, and initialize our runs from profiles of temperature and humidity in radiative-convective equilibrium (RCE) with an all-ocean surface.

For all simulations performed, perturbations are prescribed over or along the edges of a reference patch region that spans the whole short dimension of the channel, and has half-width of 24 km in the long dimension (unless indicated otherwise). The surface is allowed to evaporate freely, and its temperature is fixed at 300.2 K, except for the SSTA simulations described below. We follow Cronin, 2014 in prescribing a solar latitude of 45° and a solar constant of 560 $\mathrm{Wm}^{-2}$ and a zenith angle of 56.26°, which yield an insolation of 311 $\mathrm{Wm}^{-2}$. To prevent convective aggregation, all of our runs homogenize radiation across the domain. We perform three main groups of forced simulations (Figure 4.1). All of our simulations are run for 75 days, with the last 50 days used for the analysis.

### 4.4.1 Numerical Experiment 1: SST anomalies

For the first set of simulations, denoted by SSTA, we prescribe a constant surface temperature anomaly for the area of the patch given by $SST(x, y) = T_0 + \Delta T$ if $(x, y)$ are contained within the patch, and $T_0$ otherwise, where $T_0 = 300.2$ K is the reference surface temperature. We run simulations with $\Delta T$ taking values of $-0.4, -0.1, 0.1, 0.4, 0.7, 1.0, 1.5$ and 2.0 K. We

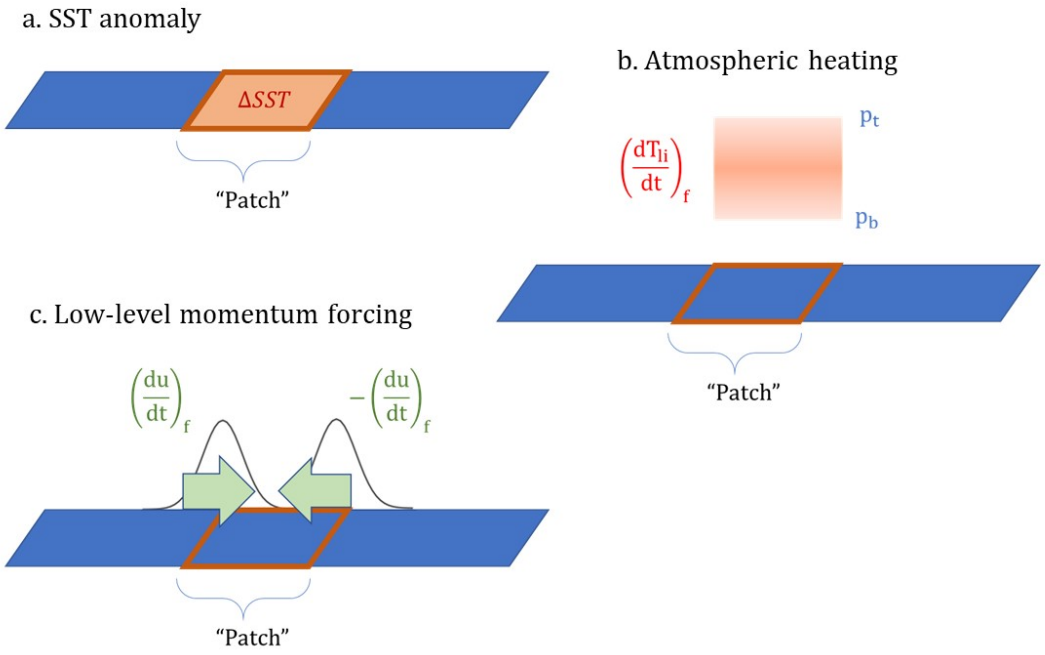


Figure 4.1: Sketches of the setups representing the three different forcings: a. Sea-surface temperature anomaly, b. Atmospheric heating between levels $p_b$ and $p_t$ , c. Low-level momentum forcing. The reference patch for which averages are calculated is indicated in red; geometry is not to scale.

note that the temperature anomaly as prescribed here is discontinuous at the edge of the reference patch—as is the heating forcing discussed in the next section. However, tests run with other profiles did not produce dramatically different results. No pathological behavior was observed from the sharp discontinuities.

### 4.4.2 Numerical Experiment 2: Localized atmospheric heating at different levels

To assess the convective response to heating at different levels, we add a forcing term $Q$ to the equation for the liquid water/ice static energy $h_{li}$:

$$\frac{dh_{li}}{dt}(p,t) = (...) + Q \tag{4.1}$$

For the forcing, we choose a half-sinusoidal shape in the vertical, constrained between two pressure levels, uniform values in the horizontal within the patch region, and zero outside.

$$Q = M \sin\left(\pi \frac{p - p_t}{p_b - p_t}\right) \tag{4.2}$$

where $M$ is the maximum amplitude of the forcing, $p$ is the pressure, and $p_t$ and $p_b$ are the pressure levels at the top and at the bottom of the heated layer, respectively. This yields an expression for $M$ in terms of the integrated column forcing, $Q_f$, namely

$$M = \frac{g\pi Q_f}{2c_p(p_b - p_t)}, \tag{4.3}$$

obtained from the mass-weighted integral of $c_p Q$ in the vertical. For instance, $Q_f = 1$ W/m$^2$ corresponds to $M = 2.05 \cdot 10^{-7}$K/s. We perform simulations with values of $Q_f$ of $-10, -5, 5, 10, 20, 40$ and 50 W/m$^2$, and apply the thermal forcings at four different levels:

- Qlb: $p_b = 1000$ hPa, $p_t = 900$ hPa,
- Qlt: $p_b = 900$ hPa, $p_t = 800$ hPa,
- Qm: $p_b = 700$ hPa, $p_t = 400$ hPa,
- Qu: $p_b = 500$ hPa, $p_t = 200$ hPa,

which represent the boundary layer, the lower free troposphere, and mid- and upper-tropospheric layers, respectively.

### 4.4.3 Numerical Experiment 3: Low-level wind forcing

The last set of numerical simulations examines the effects of purely mechanical low-level convergence on rainfall over the patch region without forced thermal gradients in the boundary layer. To do this, we introduce a forcing $F_m$ in the along-channel component (x) of the momentum equation, namely

$$\frac{du}{dt} = (...) + F_m \tag{4.4}$$

For simplicity, we assume a Gaussian-shaped distribution for the forcing, centered at each border of the strip ($x_0$), with standard deviation $\sigma_m$ of 12 km, and a vertical decay scale $h_l$ of 500 m. That is,

$$F_m(x,z) = \beta \exp\left(-\frac{(x-x_0)^2}{2\sigma_m^2}\right) \exp\left(\frac{-z}{h_l}\right) \tag{4.5}$$

Where $\beta$ is the maximum imposed acceleration. $F_m$ can be interpreted as an additional pressure gradient force, and its integral, through Bernoulli's principle, can be interpreted as a maximum consequent inflow speed in the absence of friction.

$$\int_{-\infty}^{\infty} F_m dx = -\frac{\Delta P}{\rho} = \frac{u_{max}^2}{2} \tag{4.6}$$

Here, $\Delta P$ represents the equivalent pressure drop that the forcing would produce. $\rho$ is the air density. This relationship allows us to relate the forcing strength $\beta$ to a maximal convergent wind speed $u_{max}$:

$$\beta = \frac{u_{max}^2}{2\sigma_m\sqrt{2\pi}} \tag{4.7}$$

We perform momentum forcing simulations, denoted by MF, using values of $u_{max}$ set at $-2, -1, 1, 2, 3, 5, 7$ and 10 m/s, where the negative values signify an imposed tendency for winds to blow out of the patch. We note that, while $\beta$ and $u_{max}$ do not depend on $h_l$, $h_l$ is expected to affect the strength of rainfall by modulating the depth of the convergent flow.

Our approach in the MF simulations provides a convenient way to induce convergence mechanically without prescribing a mean background wind or fixing the low-level convergence. The simple geometry of our simulations does not intend to capture the full complexity of particular scenarios of mechanically driven convergence, such as those of flow over orography. However, previous work on simulations of idealized tropical islands with simple orography and a mean background wind has shown substantial precipitation enhancement for a wide range of imposed background wind speeds (Wang & Sobel, 2017).

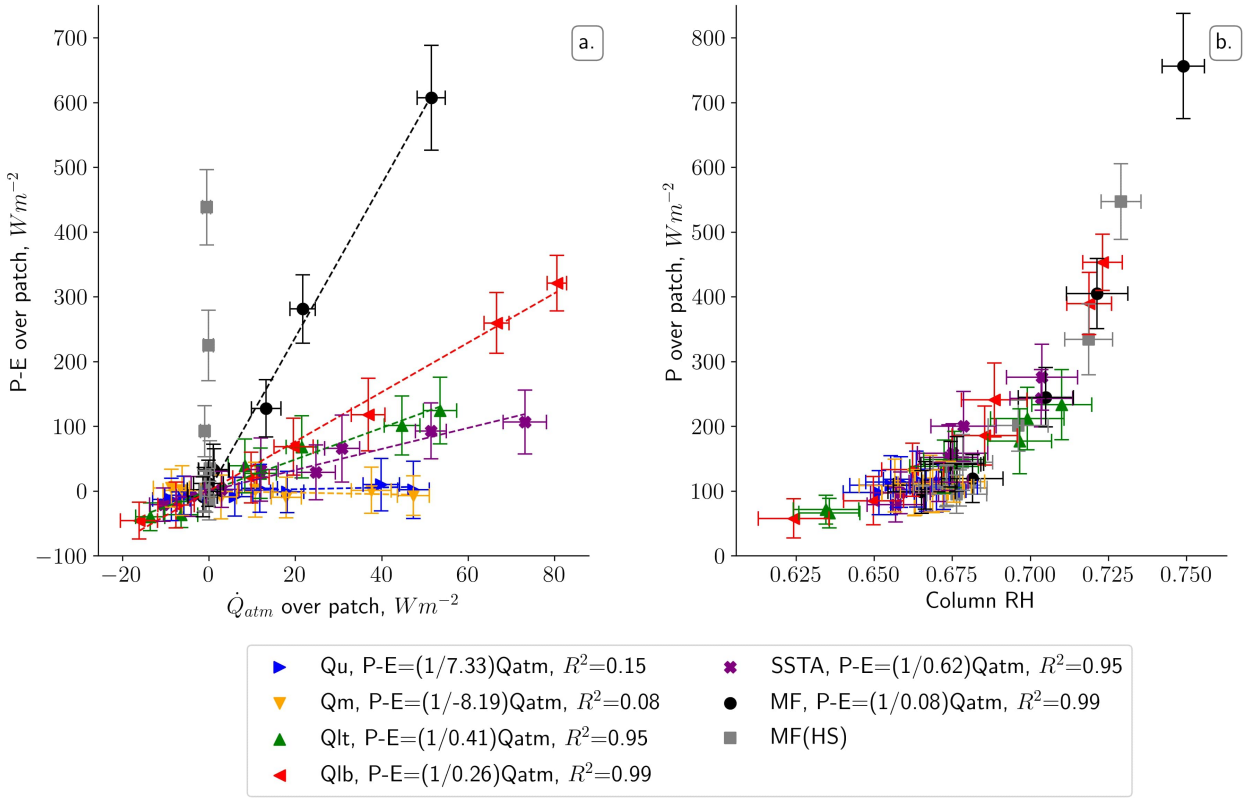


Figure 4.2: (a) $P - E$ vs. $\dot{Q}_{atm}$ over reference patch for simulations forced with atmospheric heating (triangles), SST anomaly (purple exes), low-level momentum (black circles), and low-level momentum with homogenized surface fluxes (gray squares; MF(HS)). For Qlb, Qlt, SSTA and MF, a linear fit is shown whose slope corresponds to the NGMS. Error bars indicate ±2 standard errors of the mean of daily values. (b) Precipitation vs. mean atmospheric column relative humidity—CRH–over reference patch.

## 4.5 Results

### 4.5.1 Different convective responses to different forcings

All surface and low-level forcings, namely SSTA, Qlb, Qlt and MF, result in a significant response in $P - E$, the precipitation minus evaporation or "net precipitation", over the reference patch, as shown in Figure 4.5.1. In contrast, imposed mid- and upper-level heating produces negligible changes in $P - E$. This finding agrees with Wang and Sobel, 2012, who showed a weaker sensitivity of precipitation responses to drying anomalies in the upper troposphere in WTG simulations over oceans.

Our simulations also show that low-level forcings produce different responses in $P - E$

over the patch, as indicated by the slopes of the lines in figure 4.5.1a. Following Raymond et al., 2009, we define the Normalized Gross Moist Stability—NGMS henceforth—as the quantity mediating the relationship between the column-integrated atmospheric heating rate or entropy forcing, $\dot{Q}_{atm}$, and net precipitation $P - E$. The entropy forcing is calculated as $\dot{Q}_{atm} = LHF + SHF + \dot{Q}_{rad} + Q_f$, where LHF and SHF are the surface latent and sensible heat fluxes, respectively, $\dot{Q}_{rad}$ is the radiative heating rate, and $Q_f$ is the imposed heating. Denoting the NGMS by $\Gamma_R$, we write

$$P - E = \frac{1}{\Gamma_R}\dot{Q}_{atm}. \tag{4.8}$$

A higher value of NGMS indicates thus a less efficient conversion of the net column-integrated heating into net precipitation.

A central result of this work is that the net precipitation response to distinct types of low-level forcing results in distinct values of NGMS. A forcing-dependent NGMS is reasonably well-defined for each type of low-level forcing because $P - E$ varies linearly with $\dot{Q}_{atm}$. The linearity of convective responses to transient as well as steady perturbations to the SST and the atmospheric water vapor has been shown in previous simulation based on the Weak Temperature Gradient approximation (Anber et al., 2015; Beucler et al., 2018; Kuang, 2012, 2018; Wang & Sobel, 2012), but, to the best of our knowledge, not for RCE with localized forcings.

For simulations with added column heating, the prescribed forcing, $Q_f$, must be distinguished from the total entropy forcing or atmospheric heating rate $\dot{Q}_{atm}$, which includes the atmospheric feedback on the imposed heating. This feedback is composed of changes in the latent, sensible and radiative heat fluxes from the RCE state. Although $Q_f$ represents the main contribution to $\dot{Q}_{atm}$ for simulations with atmospheric heating, surface flux feedbacks contribute up to 40 percent of the entropy forcing in the simulations with heating at the lowest levels (Qlb). For both SSTA and MF, $\dot{Q}_{atm}$ is dominated by changes in the latent heat flux, with sensible heat fluxes accounting for 20 to 30 percent of the total.

The change in precipitation induced by low-level forcings is strongly associated with changes in the column relative humidity (CRH), as indicated in Figure 4.5.1b. Previous

observational studies of tropical rainfall have documented an approximately exponential relation between precipitation and CRH (Bretherton et al., 2004; Martinez-Villalobos & Neelin, 2019; Peters & Neelin, 2006; Rushley et al., 2018), namely $P = P_0 \exp(A \cdot \text{CRH})$, where $A$ corresponds to the e-folding growth rate, and $P_0$ is a constant. We note that an exponential fit to our simulations (not shown) yields an e-folding growth rate of $\sim 21$, higher than the value of $\sim 15$ documented by observational studies (Bretherton et al., 2004; Rushley et al., 2018). A mechanistic explanation of this well-documented relationship between $P$ and CRH is currently lacking, although our findings suggest that it holds for mechanical as well as thermodynamic forcings.

### 4.5.2 Vertical profiles and Gross Moist Stability

The magnitude and structure of the mean vertical velocity profile over the patch, $\overline{w}$, is key to understanding the contrast in precipitation response across different simulations. Low-level forcings, namely SSTA, MF, Qlb and Qlt, show $\overline{w}$ profiles with two peaks: one at lower levels, localized at or close to the location of the forcing, and one in the free troposphere indicating a deep convective response (Figure 4.3, a. through c.). In contrast, forcings in the mid- and upper troposphere, Qm and Qu, only produce local responses in $\overline{w}$.

The interaction between the profiles of $\overline{w}$ and moist static energy (MSE) offers a key to understand the precipitation responses in our simulations. The MSE is given by $h = c_p T + gz + L_v q$, where $c_p$ is the specific heat capacity of air at constant pressure, $T$ is the temperature, $g$ is the gravitational acceleration, $z$ is the height, $L_v$ is the latent heat of vaporization of water, and $q$ is the specific humidity. In particular, the vertical gradient of MSE over the domain, $\partial\overline{h}/\partial z$, indicates the locations where energy is imported into or exported out of the atmospheric column. For all low-level forcings, the low-level circulations include ascent at heights where $\frac{\partial \overline{h}}{\partial z} < 0$, which implies a net low-level MSE import and its associated instability. This net import requires in turn an energy export mechanism: this occurs both through the development of the deep circulation, which has a positive GMS and thus helps export energy to the rest of the domain, and through lateral mixing (not quantified).

Are the vertical velocity profiles consistent with our expectations based on required ther-

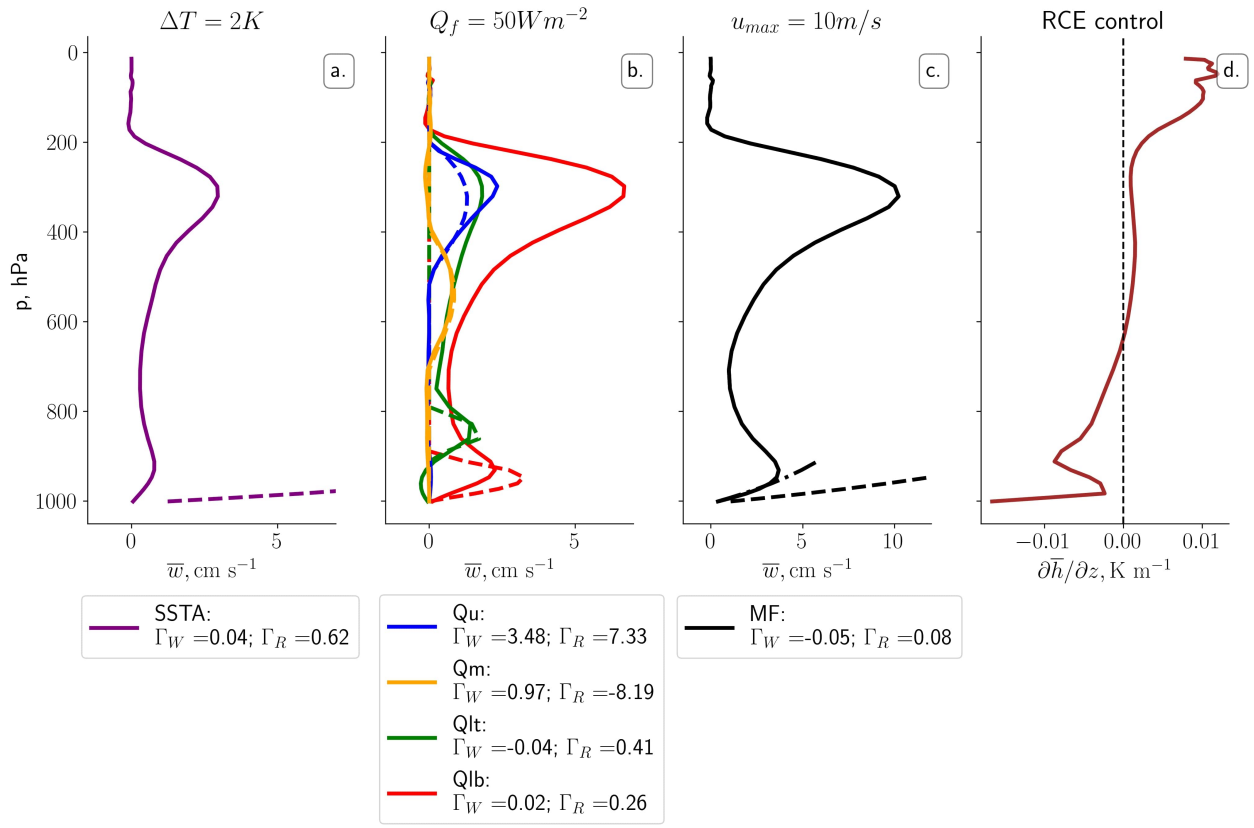


Figure 4.3: (a-c) Profiles of mean vertical velocity over the reference patch for sea-surface temperature, atmospheric heating, and momentum forcings with the highest magnitudes simulated. Dashed lines represent hypothesized profiles of w based on Bernoulli's principle and mass continuity (for SSTA and MF), and on WTG for atmospheric heating simulations (see text). Dashed-dotted line for MF shows the estimate based on the vertical profile of the forcing and the actual velocity at the patch border. (d) Vertical profile of vertical MSE gradient for the control simulation in RCE. Legend indicates the approximate NGMS, $\Gamma_W$, and the full NGMS, $\Gamma_R$ (see text).

modynamic and momentum balances for each forcing? For simulations with localized atmospheric column heating, if the convective heating were unchanged by the addition of the forcing, then the WTG vertical velocity:

$$w_{WTG} = \frac{\dot{Q}_f}{\overline{ds/dz}}, \tag{4.9}$$

would be a good model for how w responds to forcing. In the equation, $\dot{Q}_f$ is the forcing between the pressure levels specified for each simulation, and $\overline{ds/dz}$ is the vertical gradient of dry static energy—given by $s = c_p T + gz$—averaged over the depth between such pressure levels, and over the extent of the patch. Figure 4.3b offers a contrast between the mean vertical velocity profile over the patch, and the equivalent $w_{WTG}$ velocities calculated according to equation 4.9, for simulations with atmospheric column heating at different levels with magnitude of 50 $\mathrm{Wm}^{-2}$. The WTG-inferred vertical velocities capture well the local vertical velocities at the levels where the forcings are prescribed. It is surprising that $w_{WTG}$ works so well in cases that couple strongly to deep convection, like Qlb and Qlt, because there the total convective heating is clearly altered, yet the local (in height) convective heating is not greatly modified. The deep convective responses to the low-level forcings are not captured by $w_{WTG}$, as expected.

Previous work has found that forcings with steady temperature tendencies (Kuang, 2010) as well as with transient temperature anomalies (Tian & Kuang, 2019; Tulich & Mapes, 2010) produce locally confined responses when applied to the upper troposphere, and deep convective responses when applied to the lower troposphere. Using a linear response framework and Lagrangian tracking, Tian and Kuang, 2019 linked these differing responses primarily to the effects of the anomalies on the vertical velocity of updrafts and on their buoyancy, with only a secondary contribution from the changes in liquid water content of the air parcels. Despite some qualitative similarity, we note that our simulations prescribe heating tendencies, and not transient temperature anomalies, and that they are constrained horizontally as well as vertically. Further study is thus needed to assess if the mechanisms are similar.

For the momentum forcing simulation with $u_{max} = 10\mathrm{m/s}$, we obtain a physically-based null model of the $\overline{w}$ profile for the lowermost 100 hPa by equating the pressure gradient

forcing to an equivalent wind convergence through Bernoulli's principle, and integrating the mass continuity equation (see derivation in Appendix C). The null model is at best an upper bound to the horizontal winds, as it neglects friction, as well as feedbacks from cold pools over the reference patch, resulting in a large overestimation of the time-mean ascent through the depth of the mixed layer (Figure 4.3c). We note that there is high temporal variability in the ascent over the patch, and the null model does provide a good upper bound for the strongest circulations at low levels (not shown).

To obtain an analogous null-model for vertical velocity at low levels for SSTA with $\Delta T = 2$K, we proceed similarly to MF, with the added assumption that the air temperature difference between the patch and the surroundings is constant and equal to $\Delta T$ through the depth of the mixed layer (see Appendix C). This gives a corresponding pressure difference profile, which, similarly as for MF, yields an expected $\overline{w}$ of approximately 11 cm s$^{-1}$ at 950 hPa, much higher than the simulated mean. This discrepancy is largely due to the boundary-layer temperature anomalies varying between $-0.1$K and 0.15K in the lowest kilometer of the atmosphere, a much smaller contrast than the imposed SST anomaly. This is crucial, as gradients in boundary layer temperatures, and particularly their Laplacian, have been shown to play a central role in the patterns of surface convergence in the tropics (Duffy et al., 2020). For both SSTA and MF simulations, our results indicate that stabilizing feedbacks on the near-surface pressure gradients tend to weaken the ascent profile considerably.

From the budgets of moist static energy and latent energy, it can be shown that $\Gamma_R = \frac{\nabla\cdot\langle\vec{v}h\rangle}{\nabla\cdot\langle\vec{v}(s-h)\rangle}$ (see the Supplement for a derivation). However, it is common—and often convenient—to approximate $\Gamma_R$ by the contribution from the vertical transport of MSE and dry static energy by the mean vertical circulations only (Anber et al., 2015; Sobel, 2007; Wang & Sobel, 2012). This approximate NGMS, denoted here by $\Gamma_W$ and given by $\Gamma_W = \frac{\langle\overline{w}\partial\overline{h}/\partial z\rangle}{\langle\overline{w}\partial\overline{(s-h)}/\partial z\rangle}$, neglects the contributions from both vertical transients and horizontal transport terms. Horizontal transport could be neglected on the grounds that horizontal gradients in both $h$ and $s$ are normally weak, but this need not always be the case. In fact, this is likely not justified for our patches of 24 km half-widths: as indicated in the legend to Figure 4.3, $\Gamma_W$ shows poor correspondence with the values of $\Gamma_R$. The strength and structure of low-level ascent

relative to upper-tropospheric ascent modulates $\Gamma_W$, but $\Gamma_W$ does not correlate strongly with $\Gamma_R$ for these patch sizes (Figure 4.3), indicating that the effects of transients or horizontal transport—or both—are key in determining the exact value of $\Gamma_R$ for each forcing.

### 4.5.3 Patch size effects

We also test the effects of varying the spatial scales on net precipitation by running additional simulations with patches of half-widths 48, 96 and 192 km, for the SSTA and MF forcings, shown in Figure 4.4. We note that atmospheric heating simulations tended to aggregate convection for larger patch sizes and strong forcings, and were thus not included.

The behavior of $P - E$ with SST anomaly does not change substantially for different sizes for the range of anomalies considered, although the spread reaches up to 70 $\mathrm{Wm}^{-2}$ for the strongest forcing. For the momentum forcing it does exhibit wider spread, since the forcing is applied over the same area while the patch is made larger, leading to a decrease in low-level convergence. The patch size increases cause the theoretical low-level convergence to scale by a factor of 1/L, with L denoting the half-width. However, the curves do not collapse when $P - E$ is plotted against $u_{max}$/L, indicating other effects are at play.

We have established that $\Gamma_W$ is not a good approximation to the NGMS for a scale of 24 km. However, as the patch is made wider, this discrepancy decreases: for SSTA, the relative error between them drops from close to 100 percent at 24 km, to under 5 percent at 192 km. For MF, it drops from 200 percent at 24 km, to about 6 percent at 192 km. This indicates that the net contribution from transients and horizontal transport of moist and dry static energy becomes negligible at a few hundred kilometers, but plays a major role at small scales.

The values of the NGMS for SSTA do not show a clear trend as the patch is made wider, suggesting that net precipitation does not depend monotonically on the size of the region with anomalous SST. In contrast, a slight but monotonic increase is observed for MF simulations, with the lowest NGMS at the smallest scales. This is consistent with low-level wind convergence driving enhanced rainfall and weakening with increased patch area for fixed $u_{max}$.

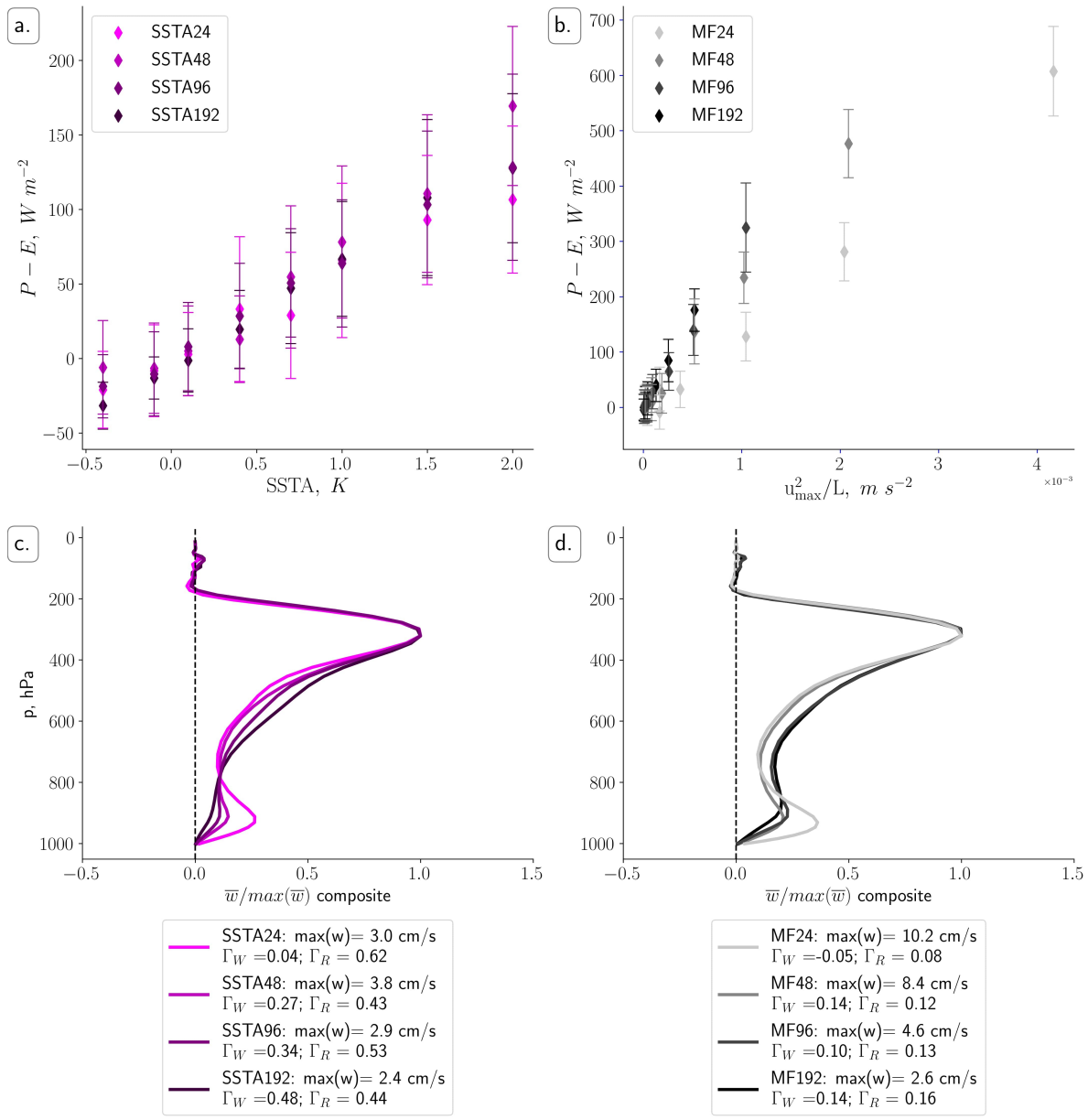


Figure 4.4: (Top row) Scatter plots of $P-E$ vs. sea-surface temperature anomaly (a.) and the square of the momentum forcing parameter $u_{max}$ divided by patch half-width (b.) for patches of half-widths 24, 48, 96 and 192 km. (Bottom row) Vertical profiles of normalized mean vertical velocities for patches of half-widths of 24, 48, 96 and 192 km for SST anomaly of 2K (c.) and momentum forcing with $u_{max}$ = 10m/s (d.). The legend indicates the maximum value of vertical velocity used for normalization, as well as the NGMS ($\Gamma_R$) and its approximated form ($\Gamma_W$; see text).

## 4.6 Discussion

We have found well-defined values of NGMS for different types of low-level forcing imposed. This suggests that we could in principle provide reasonable estimates for $P - E$ for a given forcing magnitude by interpolating from others. However, the necessity of knowing the NGMS a priori, as well as the substantial variations in NGMS between different types of forcings, severely limit the applicability of the column energetic perspective of Neelin and Held, 1987 in predicting precipitation on the basis of environmental forcings. For instance, simulations with mechanically-induced convergence and homogenized surface fluxes show greatly enhanced rainfall over patches with near-zero net atmospheric heating rates.

Our results also show that a prescribed heating in the middle and upper troposphere (above about 700 hPa) does not lead to significant net precipitation enhancement. This is a reminder that knowledge of the total atmospheric column heating rate does not necessarily provide useful information about $P-E$, unless we know how that energy input is distributed in the vertical. The use of a vertically integrated column-energetic budget might overestimate the effectiveness of upper-level heating in driving deep convection, and underestimate the capacity of low-level wind convergence to do the same.

Our simulations provide evidence that $\Gamma_W$, which only takes into account the effects of vertical transport of moist and dry static energy by the mean vertical circulations, is a poor approximation to the NGMS in most of our forcings at scales of 24 km, but improves substantially at scales of a few hundred kilometers. However, the scale at which $\Gamma_W$ becomes a reasonable approximation of $\Gamma_R$ is likely to vary depending on the characteristics of low-level convergence. Horizontal MSE transport in particular has been shown to contribute significantly to the full NGMS in relatively narrow areas such as the East Pacific ITCZ (Back & Bretherton, 2009; Back & Bretherton, 2006).

Although studying convective enhancement at large scales without homogenizing radiation would be desirable, it poses the challenge that large domains in RCE produce convective self-aggregation if radiation is made interactive (Muller & Bony, 2015; Wing et al., 2018).

Previous studies have hypothesized that precipitation rates over tropical oceans are governed by the mean moisture saturation deficit of the troposphere, and hence by the CRH

(Raymond, 2000; Raymond et al., 2009). Satellite-based observations have since confirmed a close relationship between precipitation and CRH (Bretherton et al., 2004; Peters & Neelin, 2006; Rushley et al., 2018). However, recent theoretical frameworks for tropical moist convection have argued that such relationship can be explained as a consequence of the effect of rainfall on environmental humidity via convective moisture detrainment, or that both precipitation and CRH are affected simultaneously by other causes, such as large-scale ascent and column energetics (Emanuel, 2019; Singh et al., 2019).

Our simulations show that large-scale ascent associated with column energy export, as well as ascent associated with mechanically-induced convergence, can both increase CRH. Hence, the dependence of precipitation on CRH is agnostic to the distinction between mechanical and thermodynamic forcings in our simulations, and is likely not merely due to both variables co-varying with column energetics. This hints at a plausible causal link between them, although more evidence and a mechanistic explanation would be needed to settle the matter.

## 4.7 Conclusion

Motivated by the goal of understanding the mechanisms that govern rainfall in the tropics at human-relevant spatial scales, we have explored how different kinds of thermodynamic and mechanical forcings affect precipitation rates in idealized cloud-resolving simulations of a tropical atmospheric domain. Our results indicate that the Normalized Gross Moist Stability, which mediates the relationship between atmospheric heating and net rainfall, is well defined within simulations with low-level forcings, such as localized sea-surface temperature anomalies, low-level atmospheric heating, and mechanically-induced horizontal winds that converge onto a reference area, but varies substantially from one type of forcing to another. Despite their differences in NGMS, our simulations collapse onto the same curve of precipitation versus column relative humidity. This suggests that the mechanisms that maintain this relationship deserve more attention.

## 4.8 Open Research

Processed simulation data and scripts are available on Zenodo. DOI: DOI:10.5281/zenodo.10086216. (Velez-Pardo, 2023).

# Chapter 5

# Concluding Remarks

In this thesis, we have presented three studies that probe two aspects of convective dynamics of the tropical atmosphere through idealized frameworks.

**Numerical simulations of Rayleigh-Bénard convection**

Chapter 2 uses numerical simulations of convective setups based on the Rayleigh-Bénard system to study convective organization and the formation of large-scale flow structures. In it, we find that convection organizes more readily at large scales—i.e. at scales larger than the typical length scales of individual convective plumes or thermals—when the thermal boundary conditions prescribe heat fluxes rather than temperatures. We also show that some combinations of thermal boundary conditions yield structures that share a number of the essential characteristics of tropical cyclones: a warm core, a bottom-intensified azimuthal circulation, a highly axisymmetric wind profile, persistence in time, and a large spatial extent. We identify that asymmetry of the thermal boundary conditions, a convective Rossby number greater than about unity, and, crucially, a dependence of the bottom heat fluxes on the overlying flow, are more conducive—and potentially uniquely so—to the formation of TC-like structures compared with all other combinations of parameters and conditions tried.

More generally, the chapter brings together a framework used in traditional studies of turbulence and fluid mechanics—the Rayleigh-Bénard convective setup, RBC—and current research questions in tropical atmospheric dynamics. In doing so, it purports to establish a

closer dialogue between two disciplines that have much to gain from each other. Thinking about tropical cyclones in terms of the Rayleigh or the convective Rossby numbers can help establish parallels with flows and regimes observed in RBC studies, and continue to provide insights about the mechanisms for TC genesis and intensification.

The work raises plenty of new, potentially meaningful questions for further research. For instance, it is possible that the large-scale vortices that form in setups with a constant flux at one boundary and no flux at the other have some geophysical significance—they could potentially relate to sub-mesoscale eddies in the ocean: assuming a heat flux of 100 $W\ m^{-2}$, a mixed-layer depth of 50 $m$, and an $f = 10^{-4}\ s^{-1}$ yields a convective Rossby number of O(1). Additionally, they show that vertical vorticity organizes rather easily even in the absence of WISHE-like feedbacks, provided a constant buoyancy flux. This constraint could be relaxed, to explore the effects of near-constant and decidedly non-constant flux-based conditions, which might prove of interest in the study of tropical cyclogenesis.

Due to computational constraints, we have not been able to simulate large enough domains to contain more than one TC-like vortex. As computational resources become available, it would be fruitful to revisit simulations like the setup with insulating top and flow-dependent heat flux at the bottom in a substantially larger domain, which would permit exploring the natural scales of the vortices. Another avenue for research that would be possible with greater computational resources would be establishing the effects of much larger flux Rayleigh numbers ($\mathrm{Ra_F} \gg 10^8$) on the spatial scales of convective organization and on the formation of TC-like structures under temperature-based boundary conditions.

Plenty of other questions remain open. We give three more examples: First, in our case, imposing a flow dependence on the heat fluxes was necessary to produce TC-like vortices. However, this could be circumvented by introducing roughness in the bottom boundary, as it helps short-circuit the thin bottom thermal boundary layer, naturally coupling the heat fluxes with the turbulent flow above. Second, we have not carried out finite amplitude simulations, but it would be meaningful to establish, for example, if well-formed TC-like vortices persist when introduced in a setup with a convective Rossby number below 1—if not, this would give more evidence of the dynamical threshold found in our work. Third, formulating a Potential Intensity for the dry TCs in the domain and contrasting it with

their actual strength would be a valuable comparison with our understanding of mature TCs on Earth. Doing so would require a model for the momentum drag, or an imposed drag parameterization at the boundaries, as well as an adequate formulation of the thermodynamic efficiency for the flux-based thermal boundary conditions used, none of which are clear at present.

These are some of the questions inspired by the work which, we hope, help showcase the fertile ground that results from applying an idealized setup with a rich literature of its own like Rayleigh-Bénard, to tropical cyclone physics and convective organization.

**Tank experiments of RBC**

Chapter 3 is motivated by chapter 2, specifically by the finding that persistent, large-scale cyclonic vortices can form in simple dry rotating RBC setups even without parameterizing the heat fluxes to depend on the flow. Using experiments of hot water in a rotating tank with an insulating bottom and sides, and a top exposed to the air, we ran a suite of experiments varying the rotation rate and water depth, which effectively translate into changes in the mean convective Rossby number, flux Rayleigh number and aspect ratio. Our sweep over parameter space covered the approximate intervals $(10^8, 10^{10})$ for $\mathrm{Ra_F}$ , $(0.35, 1.6)$ for $\mathrm{Ro_C}$, and $(4.5, 9.8)$ for the aspect ratio.

The most important finding from the chapter is the experimental confirmation that large-scale, persistent cyclonic flows tend to form in a Rayleigh-Bénard-like setup in the parameter space in which they were observed in numerical simulations of the previous chapter. In particular, we showed that convective Rossby numbers of about 1 or higher are necessary for large-scale cyclones to emerge and persist. However, this comparison must be taken with some caution, as the top thermal boundary condition in the experimental setup is not the same as the homogeneous, no-slip, constant-flux bottom condition of the numerical simulations. The fluxes at the top boundary are affected to some degree by the radially dependent shear caused by the relative motion of the water and the air, as the latter is not in solid body rotation with the tank. At high enough rotation speeds, this might become significant, causing convection to organize at large scales due to the heterogeneities in the forcings at

the boundaries, as in the case of thermal highs/lows in the atmosphere. Importantly, the upper boundary condition in the experiments is free-slip, which introduces differences in the momentum budget with respect to the no-slip conditions of our simulations, and of flows in contact with the Earth's surface. Nonetheless, it is interesting and likely not coincidental that the large cyclonic flows appear in the same range of convective Rossby numbers as in the simulations with no-slip boundaries and either homogeneous or flow-dependent heat fluxes.

Future work could improve upon the setup to guarantee greater control over the range of parameters and the thermal boundary conditions. For instance, using heating pads as the source of buoyancy, instead of relying on the free evaporation of hot water to the air above, would give us better a priori knowledge of the heat flux and thus of the Rayleigh and the convective Rossby numbers. This would likely require changes in the tracers used, as convection would be triggered at the bottom of the fluid. Additionally, in order to properly study organized convection with homogeneous thermal boundaries, the rotating tank setup should have the air spin up alongside the water so that both achieve solid body rotation. This prevents the effects from radially varying shear and the differential heat fluxes caused by it. Finally, characterizing the thermal structure of the fluid would be important, as it would allow to compare the flow speeds with theoretical expectations for balanced flows. Snapshots from a thermal infrared camera did not reveal clear patterns in the fluid surface temperature, although continued monitoring and time averaging might. This can also be achieved by properly distributed thermometers, guarding that they present low enough contrast to not interfere with the tracer tracking.

From a broader perspective, this work shows that tank experiments continue to provide a valuable approach to study geophysical flows, in general, and the convective dynamics of the atmosphere and ocean in particular. While numerical simulations allow easier access to three-dimensional data, experiments facilitate an exploration of higher levels of turbulence than computational costs permit. Just as importantly, they offer a palpable confirmation that the findings from idealized simulations are capturing the right physical processes.

**Precipitation responses to forcings**

Chapter 4 uses cloud-resolving numerical simulations of the tropical atmosphere to study the precipitation responses to imposed mechanical and thermodynamic forcings at scales of tens to a few hundred kilometers. It probes the column-integrated perspective pioneered by Neelin and Held (1987) as a mechanistic explanation for the location and intensity of tropical precipitation, showing that different types of forcings lead to different Normalized Gross Moist Stabilities. It shows that purely mechanically induced low-level wind convergence is an effective driver of precipitation at the smaller scales, despite having little effect on the column MSE budget, and that this is still the case when surface fluxes are homogenized. This indicates that using a vertically integrated column energy budget underestimates the capacity of low-level wind convergence to enhance rainfall.

While the work does not call into question the usefulness of a column-energetic approach in all contexts, it does show several important shortcomings, particularly in cases of strong large-scale wind convergence, or in areas of flow over mountainous terrain where convection is strongly mechanically forced. The vertical component of the GMS, often used as an approximation to the full NGMS, is shown to be a particularly precarious estimate of atmospheric stability for forcings at scales of a few tens of kilometers, although these numbers should not be extrapolated lightly to other environments. It has been shown, for instance, that low-level convergence and horizontal transport of MSE are a dominant control on rainfall over the narrow East Pacific ITCZ, with a scale of several hundred kilometers (Back & Bretherton, 2006).

A limitation of the work, and of RCE simulations in general, is the need to prescribe homogenized radiative fluxes in order to prevent convective aggregation when the domain is larger than a few hundred kilometers. Horizontal variations in the radiative fluxes could have an effect over the responses, but it is unclear how much those would alter the results obtained with homogenized radiation.

An intriguing avenue for future research is the collapse across all forcings onto a common curve of precipitation vs. relative humidity. As a first step, it would be important to document whether this relationship holds at different scales and across other types of forcings, for example artificially drying different layers of the atmosphere. A mechanistic understanding the effects of different forcings on the column relative humidity could potentially provide a

link between the forcing characteristics and the precipitation response, including the effects of mechanically forced convergence.

With a few modifications, this work could be gradually adapted to study land-like or coastal environments, for instance by limiting surface evaporation, using a slab ocean with different heat capacities, or introducing orography. Making the forcings oscillatory or transient is a straightforward modification to study sea breezes and other mesoscale circulations. Additionally, creating purely mechanically forced vortices could contribute to our understanding of some of the dynamics of heat lows and tropical cyclones, tying to the work of the previous chapters.

**To conclude**

As a general contribution, the goal of this thesis has been to highlight the use of idealized frameworks, in experiments as in numerical simulations, in the study of atmospheric convection and phenomena associated with it. We hope to have provided enough evidence that such approaches enrich our understanding of the basic mechanisms behind complex atmospheric processes, create a tangible bridge between disciplines, and spawn fruitful questions that keep the field alive and well. Although a complete mathematical formulation of the phenomena studied here still remains out of reach, we hope this work contributes to shape our physical intuition in the direction of the quote by Bertrand Russell with which we started, by bringing the phenomena analyzed a few steps closer to the basic equations of fluid motion.

# Appendix A

# (Appendix to Chapter 2)

## A.1 Supplemental videos

Two videos are included as supplemental material to Velez-Pardo and Cronin, 2023: Video1: shows the evolution of a TC-like vortex for a simulation with insulating top boundary condition, flow-dependent heat flux boundary condition at the bottom, convective Rossby number 2.0, flux Rayleigh number $10^9$, Prandtl number 1.0. The top three panels show plan views of the horizontal wind speeds at 20 percent of domain height (left), the vertically averaged temperature anomaly (middle), and the vorticity at 50 percent of domain height (right). The bottom two panels show time series for the evolution of L (the length scale of spatial organization defined in the main text) for the fields of the same three variables (top subpanel) and of L relative to its values at 1 rotational time period (bottom subpanel). Video 2: shows a zoomed-in area of the plan view of the horizontal wind speed at 20 percent of domain height for a simulation with Ins/PF boundary conditions, aspect ratio=16, $\mathrm{Ro_C} = 0.2$. Vortices do not exhibit the longer time persistence of higher $\mathrm{Ro_C}$ simulations. Note that Ro in the video titles is the convective Rossby number.

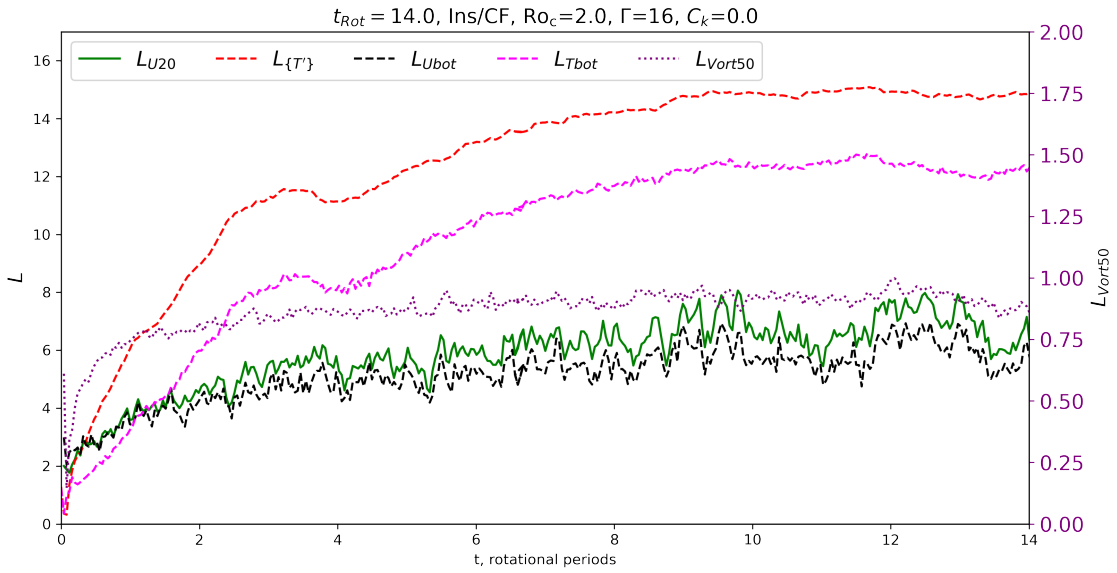


Figure A.1: Time series of L for different fields specified below, for Ins/CF (insulating top, constant-flux bottom) boundary conditions.

## A.2 Evolution of spatial organization (L) for different variables for Ins/CF setup

The variables in Figure A.1 are $L_X$, the spatial length scales defined according to equation 7 in the main text, with the following conventions for the fields:

U20: the horizontal wind speed ($\sqrt{u^2 + v^2}$) at 20 percent of domain height.

$\{T'\}$: the vertically averaged deviation of temperature with respect of the horizontal mean (that is, the vertically averaged Archimedean buoyancy).

Tbot: The temperature field at 5 percent of domain height.

Ubot: The horizontal wind speed at 5 percent of domain height.

Vort50: The vertical component of vorticity ($\partial v/\partial x - \partial u/\partial y$) at 50 percent of domain height.

The figure shows that the time series for Ins/CF shown in Figure 2.2 had equilibrated already by 10 rotational time periods.

## A.3 Simulations with free-slip and no-slip top boundary condition for Ins/PF setup

The simulation with boundary conditions labeled Ins(FS)/PF is similar to the setup Ins/PF, but with a free-slip boundary condition at the top, instead of a no-slip condition. This simulation shows that a free-slip condition does not fundamentally alter the results with a no-slip top.

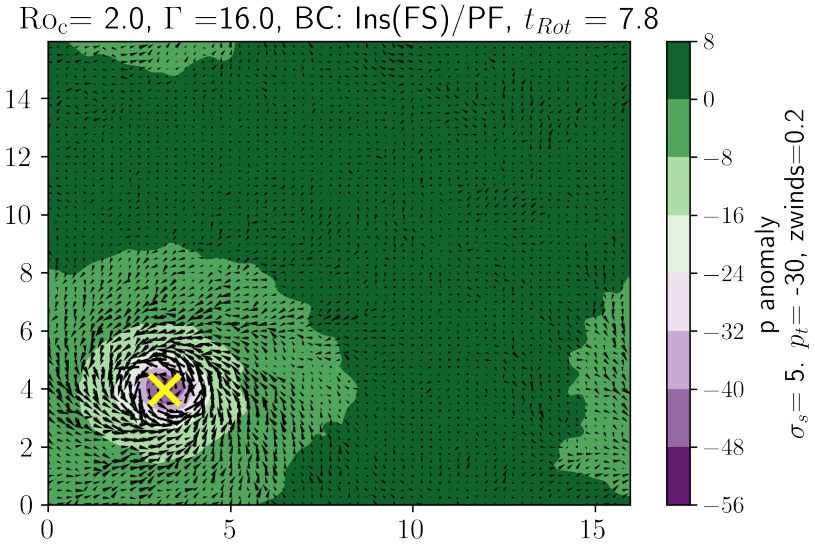


Figure A.2: Plan view of pressure anomaly contours and quiver plot of horizontal winds at 20 percent of domain height for simulation with flow-enhanced heat bottom heat fluxes, insulating top, and free-slip condition. Yellow cross shows the centroid of the pressure anomaly, $\sigma_s$ refers to the standard deviation of the Gaussian filtering, and $p_t$ is the threshold pressure anomaly to calculate the centroid in each case.

## A.4 Additional simulations varying domain size and convective Rossby number

Three additional simulations were run with higher domain aspect ratio and convective Rossby numbers of 2, 3 and 4, as discussed in the main text. Plots from their pressure field, flow, and azimuthally composited profiles are shown here.

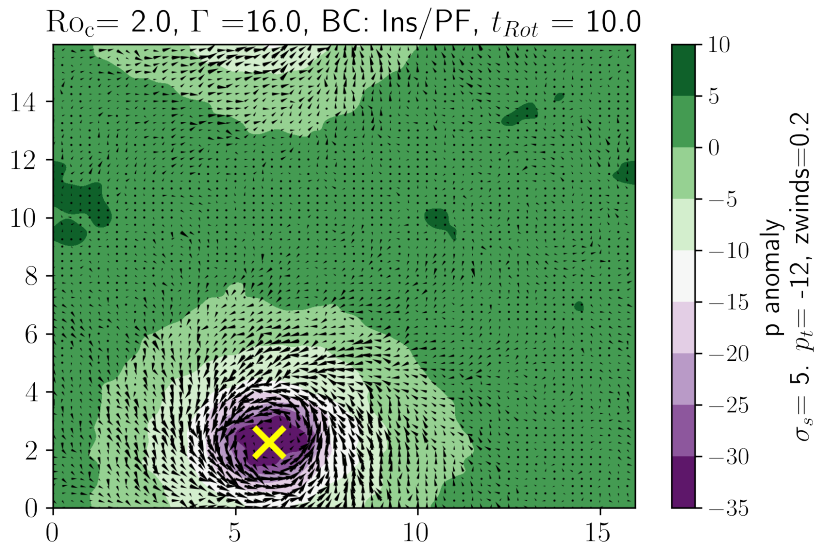


Figure A.3: Same as A.2 but with no-slip top boundary condition.

## A.5 Time series for simulations with asymmetric flux conditions (CF/PF) with two different values of enhancement parameter $C_k$

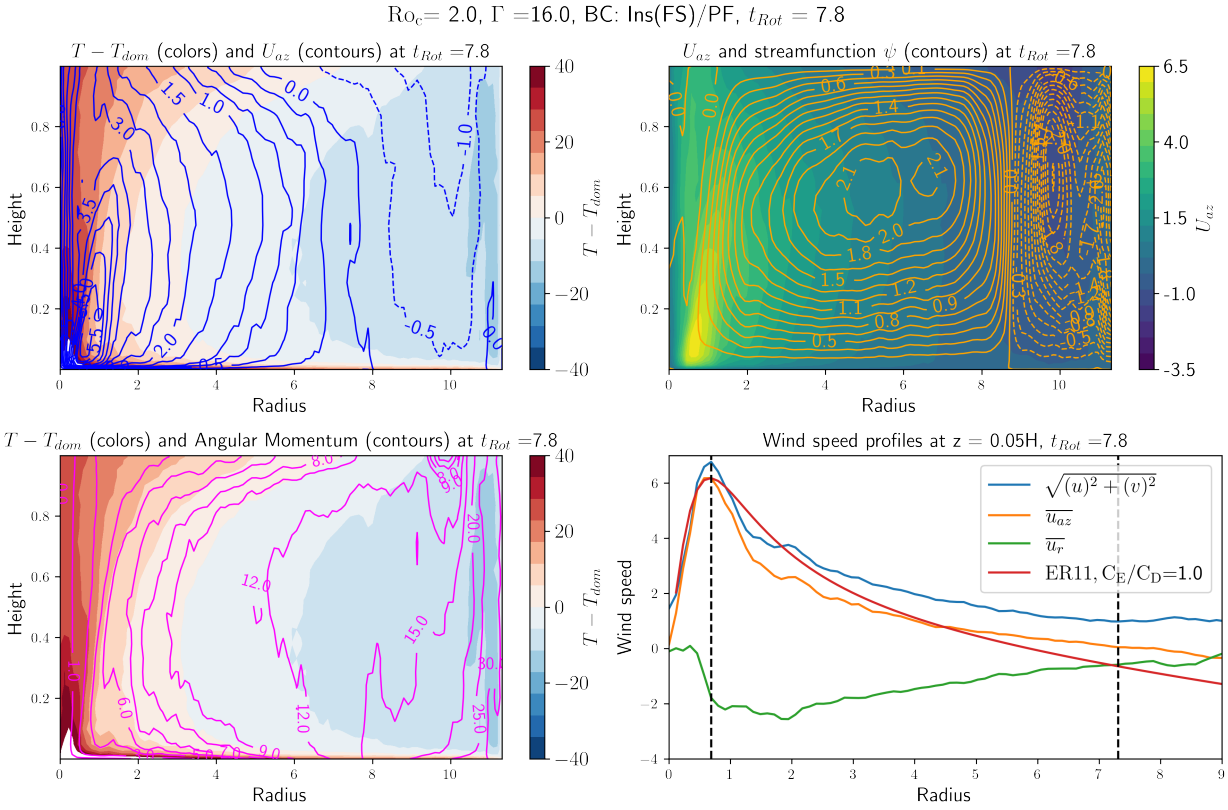


Figure A.4: Contour plots of azimuthally averaged quantities (temperature anomaly with respect to domain mean, azimuthal wind speed, angular momentum, streamfunction of the secondary circulation), and azimuthally averaged wind speed profile of vortex formed in domain Ins/PF thermal boundary conditions, aspect ratio $\Gamma = 16$, convective Rossby number $\mathrm{Ro_C} = 2$, free-slip boundary condition at the top, and no-slip at the bottom, after storm size had equilibrated.

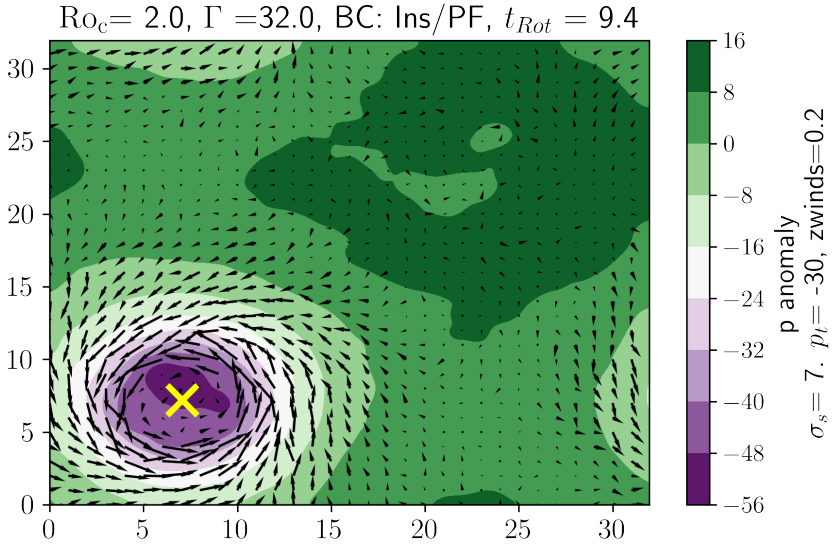


Figure A.5: Plan view of pressure anomaly field and quiver plot of horizontal winds at 20 percent of domain height for simulation with $\Gamma = 32$, and convective Rossby number $Ro_c = 2.0$ after equilibration. A yellow "x" marks the centroid of the low pressure anomaly feature.

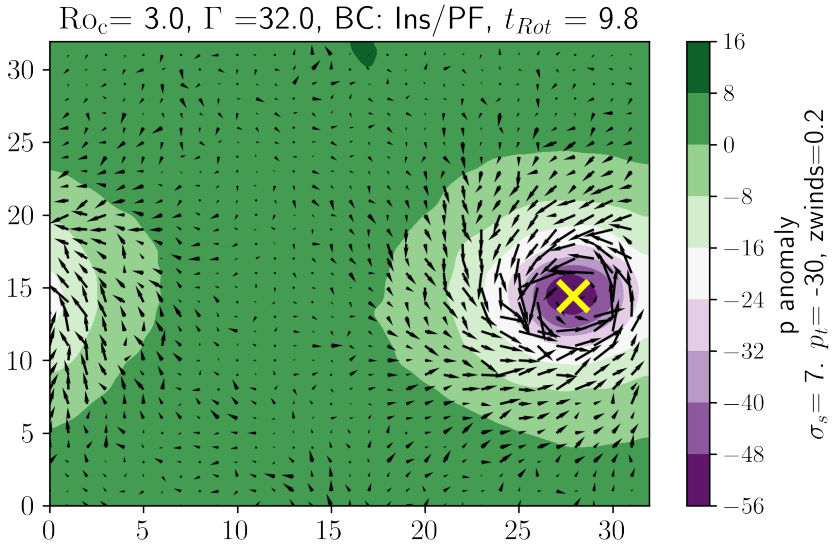


Figure A.6: Same as A.5 but with $Ro_c = 3.0$.

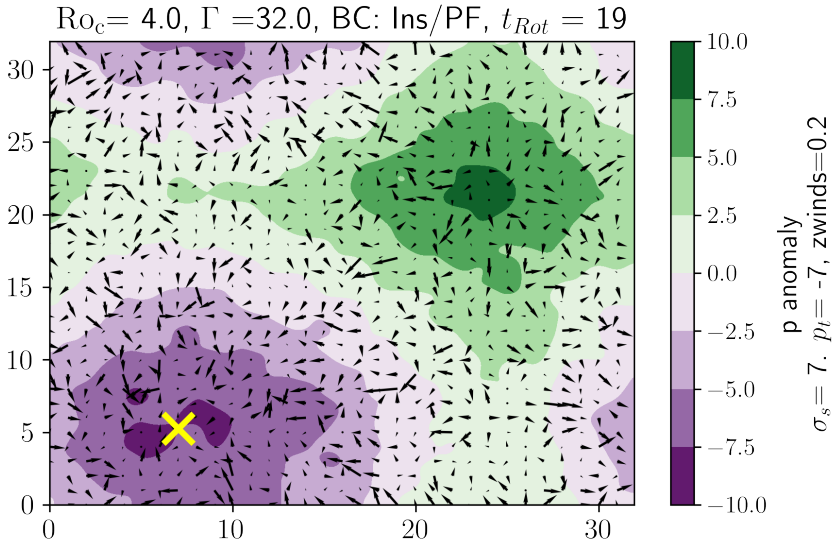


Figure A.7: Same as A.5 but with $Ro_c = 4.0$.

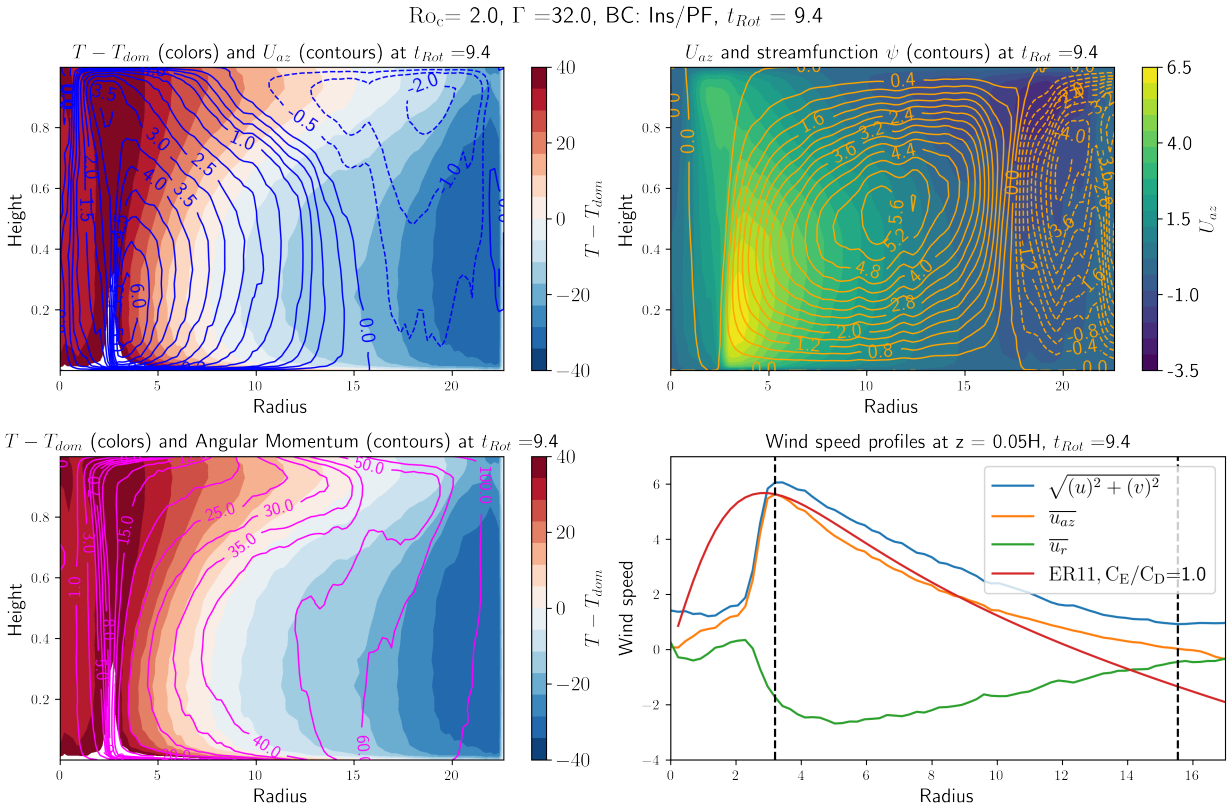


Figure A.8: Contour plots of azimuthally averaged quantities (temperature anomaly with respect to domain mean, azimuthal wind speed, angular momentum, Stokes streamfunction), and azimuthally averaged wind speed profile of vortex formed in domain with aspect ratio 32 and convective Rossby number $Ro_C = 2.0$.

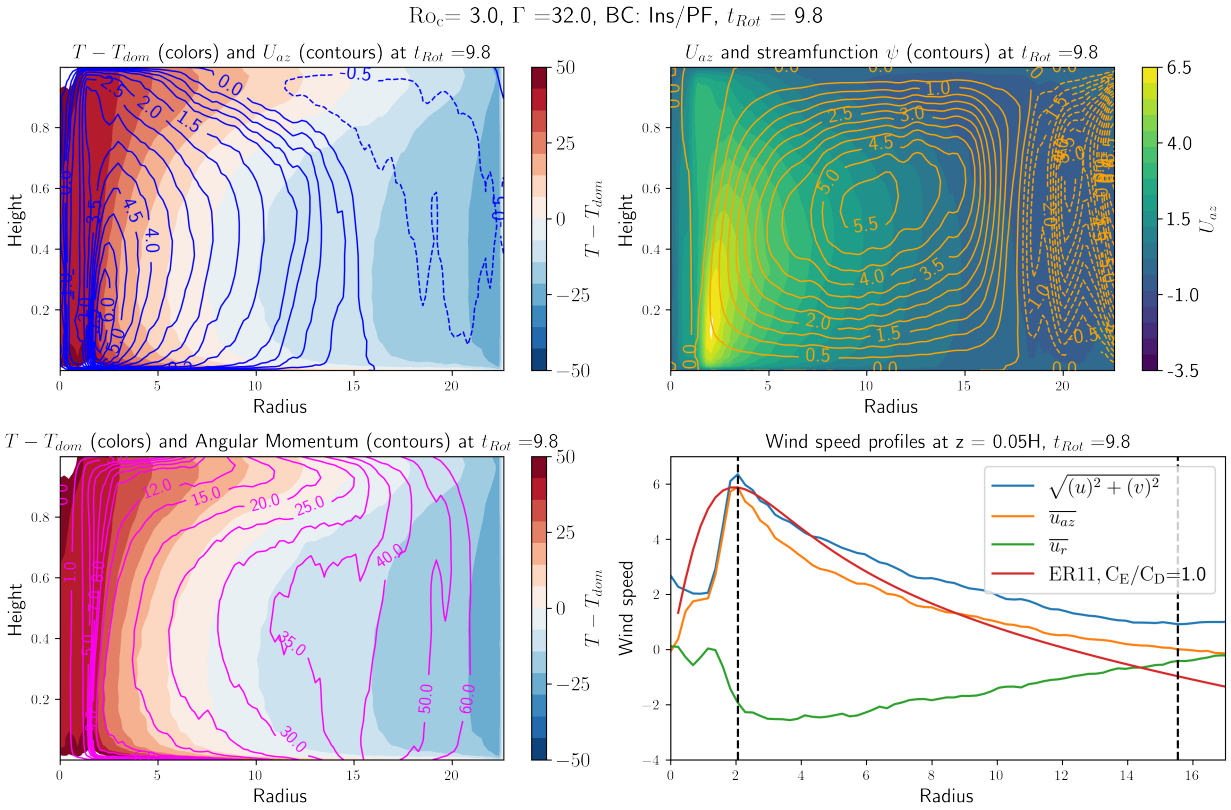


Figure A.9: Same as A.8, but with $Ro_C = 3.0$.

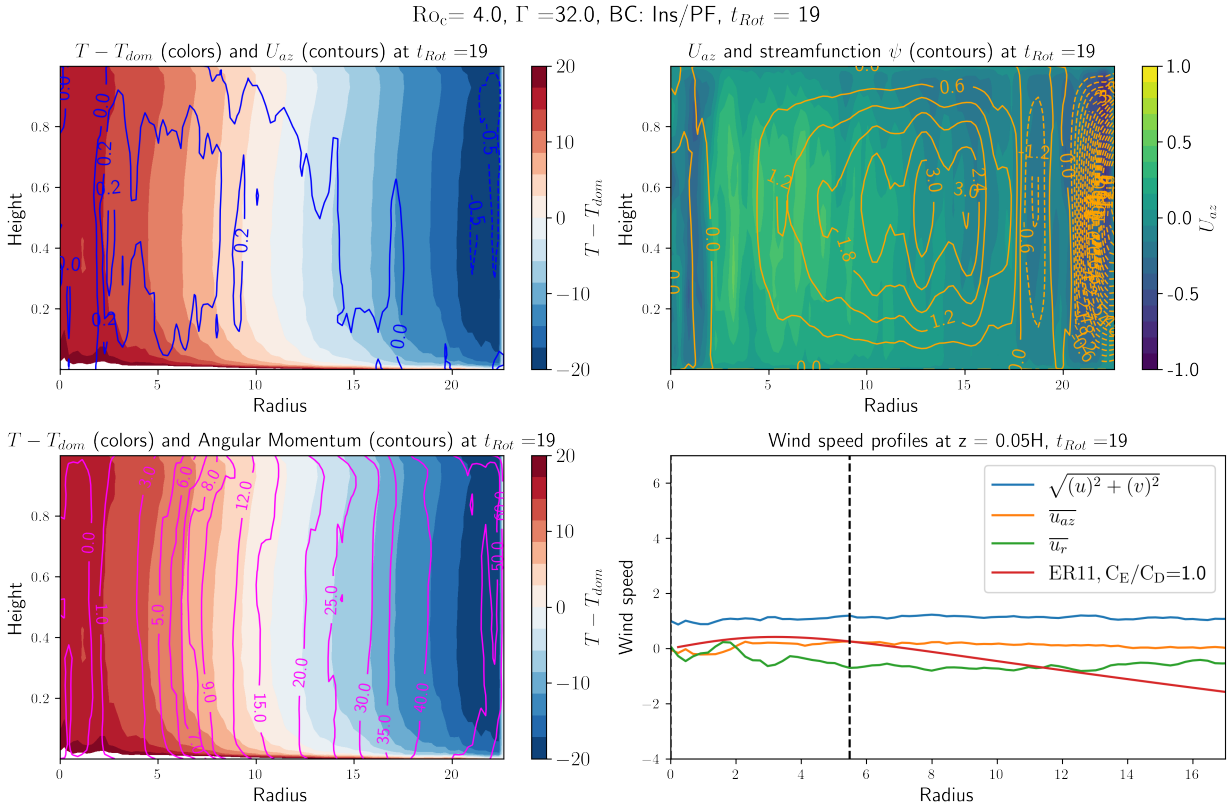


Figure A.10: Same as A.8, but with $Ro_C = 4.0$. No large-scale TC-like vortex was observed within the 20 rotational periods that the simulation was run for. The azimuthal averaging was done about the centroid of the low-pressure anomaly.

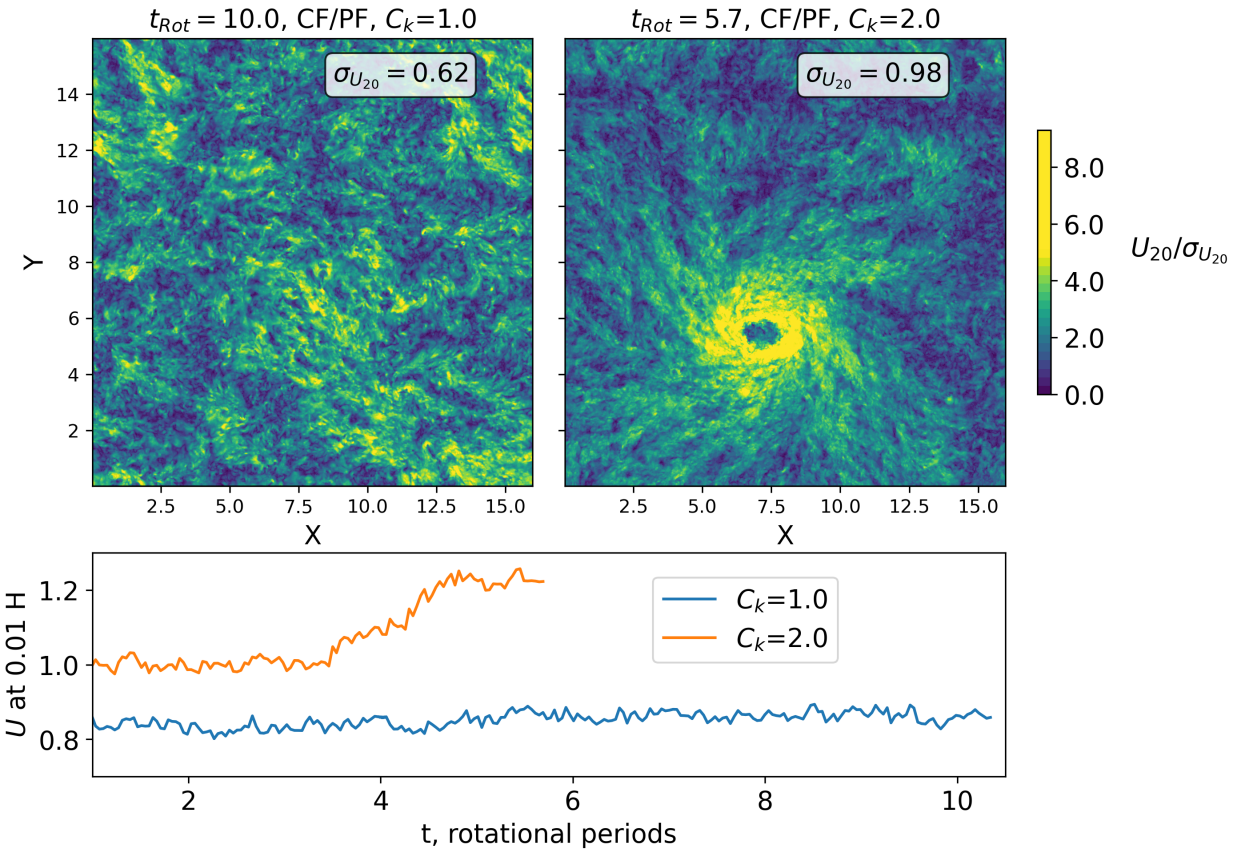


Figure A.11: Plan view of horizontal wind speeds at 20 percent (top two) and time series of mean horizontal wind speeds at 1 percent of the domain height, for simulations with CF/PF boundary conditions, with bottom boundaries with $C_k = 1.0$ and $C_k = 2.0$. Only the latter developed a TC-like structure.

# Appendix B

# (Appendix to Chapter 3)

| **Exp. ID #** | $\tau_{Rot}$**, s** | $H$**, cm** | $(\mathrm{Ra_{F,1}}, \mathrm{Ra_{F,7-10}})/10^8$ | $(\mathrm{Ro_{C,1}}, \mathrm{Ro_{C,7-10}})$ | **Notes** |
|---|---|---|---|---|---|
| 3 | 125 | 3.5 | (12.6,4.7) | (1.6,1.2) | |
| 4 | 153 | 3.5 | (12.1,2.3) | (2.3,1.4) | |
| 5 | 125 | 3.5 | (10.7,4.3) | (1.5,1.2) | |
| 6 | 70 | 3.5 | (12.7,8.0) | (0.9,0.8) | |
| 7 | 70 | 3.5 | (15.6,8.1) | (1.0,0.8) | |
| 10 | 153 | 3.5 | (13.0,2.3) | (2.3,1.4) | 40 B |
| 11 | 70 | 3.5 | (13.8,8.5) | (0.9,0.8) | 40 B |
| 12 | 125 | 3.5 | (17.4,4.8) | (1.8,1.2) | 40 B |
| 13 | 104 | 3.5 | (9.6,3.5) | (1.4,1.1) | |
| 14 | 125 | 4.5 | (34.7,11.8) | (1.6,1.2) | |
| 15 | 153 | 4.5 | (30.9,8.5) | (1.9,1.3) | |
| 16 | 104 | 4.5 | (32.8,14.9) | (1.3,1.0) | |
| 17 | 70 | 4.5 | (29.2,20.1) | (0.8,0.8) | |
| 18 | 70 | 2.5 | (2.1,0.9) | (1.1,0.9) | |
| 19 | 104 | 2.5 | (2.9,0.6) | (1.9,1.2) | |
| 20 | 125 | 2.5 | (2.7,0.5) | (2.2,1.4) | |
| 21 | 153 | 2.5 | (2.0,0.4) | (2.5,1.4) | |
| 22 | 153 | 4.5 | (33.9,8.3) | (1.9,1.3) | |
| 23 | 104 | 3.5 | (12.0,3.9) | (1.5,1.1) | |
| 24 | 70 | 2.5 | (2.0,0.9) | (1.1,0.9) | |
| 25 | 104 | 2.5 | (2.4,0.6) | (1.8,1.2) | |
| 26 | 125 | 2.5 | (1.9,0.5) | (2.0,1.3) | |
| 27 | 153 | 2.5 | (2.0,0.4) | (2.5,1.5) | |
| 28 | 104 | 4.5 | (31.3,13.6) | (1.3,1.0) | |
| 29 | 70 | 4.5 | (20.8,19.6) | (0.7,0.8) | |
| 30 | 153 | 4.5 | (22.9,8.6) | (1.7,1.3) | |
| 31 | 153 | 3.5 | (11.2,2.3) | (2.2,1.4) | |
| 32 | 153 | 2.5 | (2.2,0.4) | (2.5,1.5) | |
| 33 | 70 | 4.5 | (20.5,17.1) | (0.7,0.7) | |
| 34 | 70 | 3.5 | (11.2,5.2) | (1.0,0.8) | |
| 35 | 70 | 2.5 | (1.9,1.0) | (1.1,0.9) | |
| 39 | 35 | 4.5 | (3.5,19.4) | (0.2,0.4) | |
| 40 | 35 | 3.5 | (3.0,10.4) | (0.3,0.5) | |
| 41 | 35 | 2.5 | (2.1,1.9) | (0.6,0.6) | |

Table B.1: Experiment data. Columns represent the experiment ID number, the rotational time period $\tau_{rot}$, water depth $H$, the pair given by the flux Rayleigh number at 1 rotation and the average $\mathrm{Ra_F}$ between 7 and 10 rotations, and the pair given by the convective Rossby number number at 1 rotation and the average $\mathrm{Ro_C}$ between 7 and 10 rotations. The notes "40 B" represent experiments where the wind barrier was 40 cm, whereas for all others it was 25 cm.

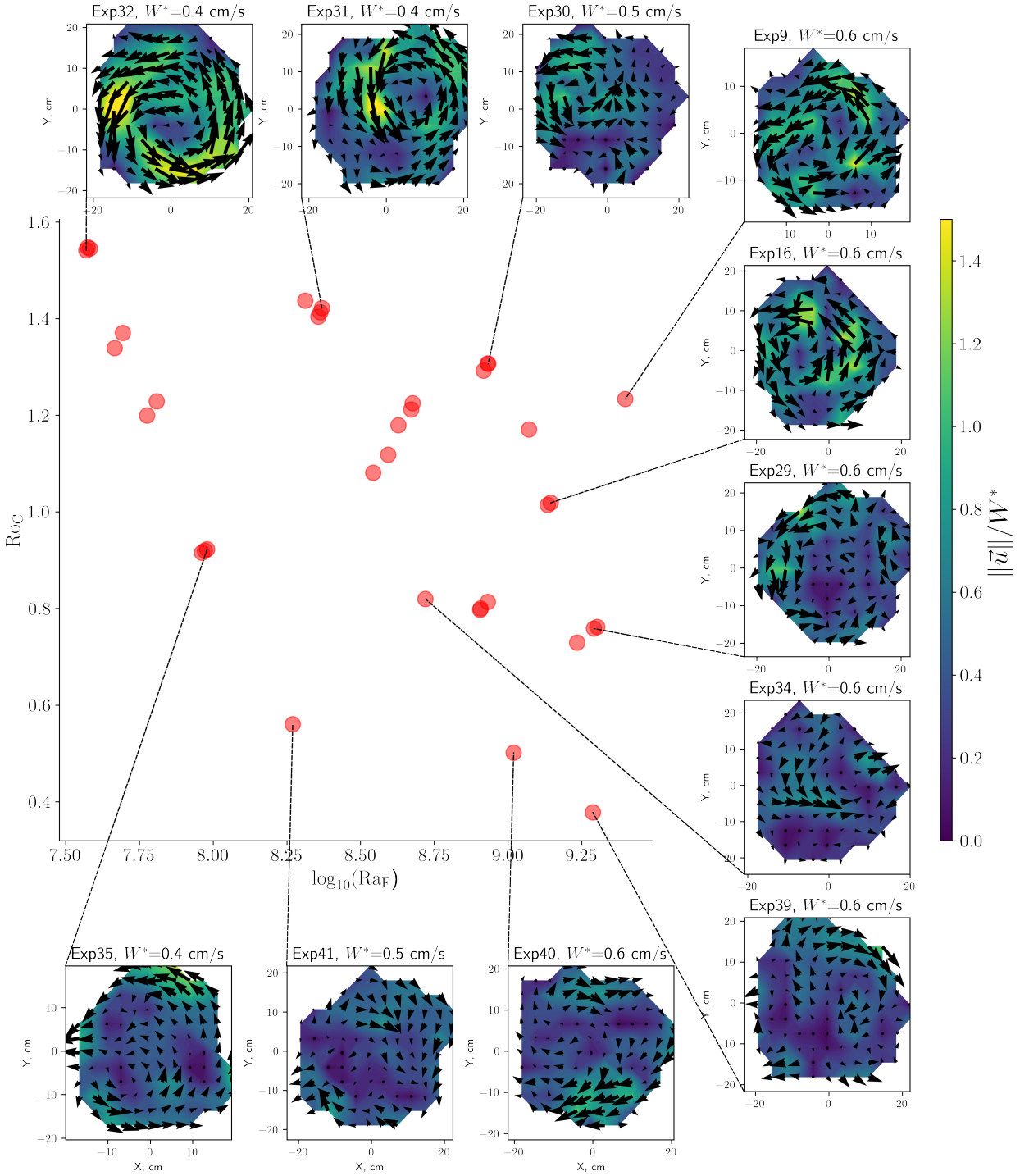


Figure B.1: Scatterplot as in Figure 3.3, with flow fields at $t = 7$ rotational periods.

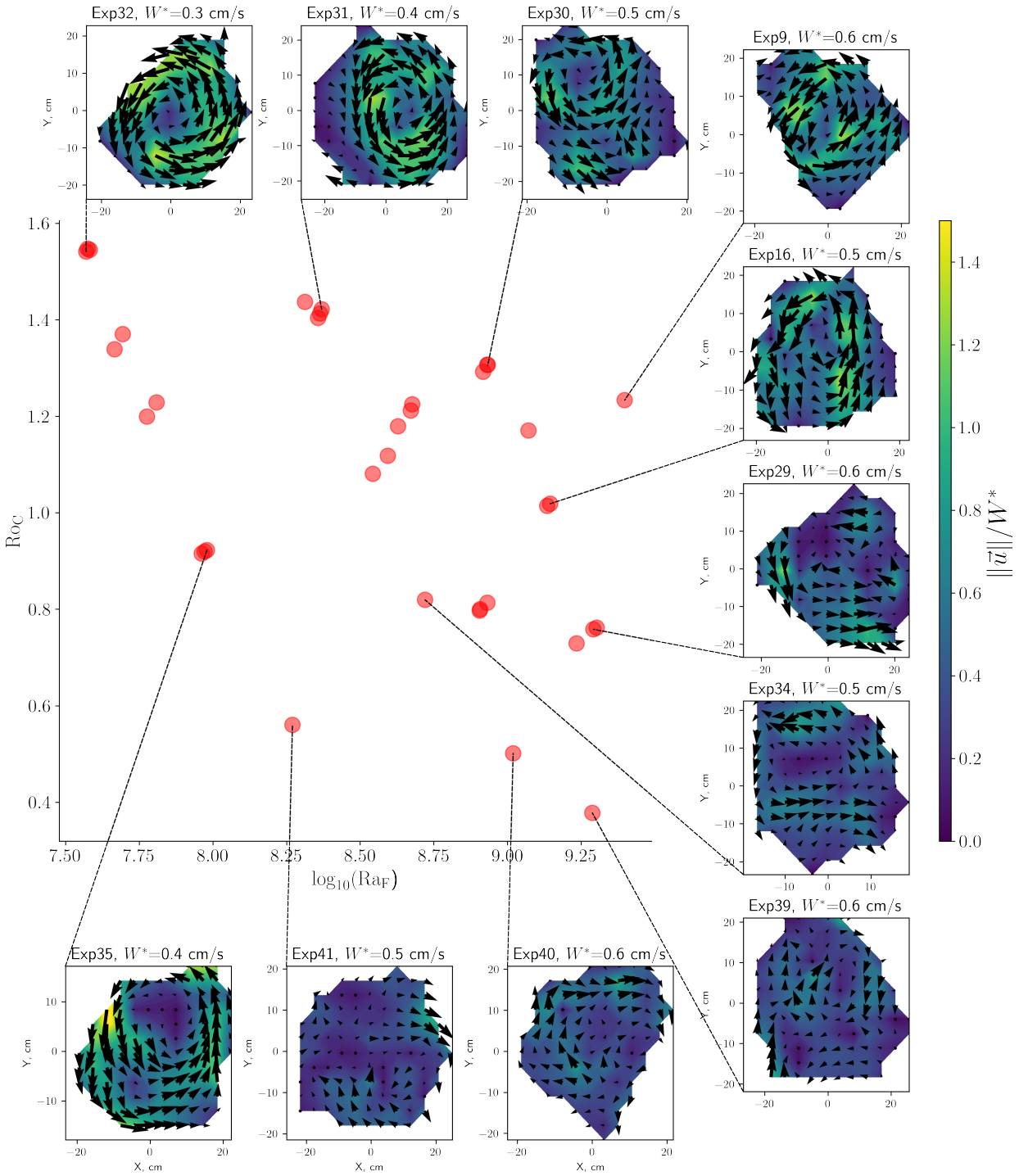


Figure B.2: Scatterplot as in Figure 3.3, with flow fields at $t = 9$ rotational periods.

# Appendix C

# (Appendix to Chapter 4)

## C.1 Derivation of reference w profile for momentum forcing (MF) simulations

From mass continuity, we have

$$-\frac{\partial w}{\partial z} = \frac{\partial u}{\partial x} \tag{C.1}$$

Integrating in x across the patch yields

$$-\int_{-L}^{L} \frac{\partial w}{\partial z} dx = \int_{-L}^{L} \frac{\partial u}{\partial x} dx, \tag{C.2}$$

which implies

$$-2L\frac{\partial w}{\partial z} = -2u_b, \tag{C.3}$$

where $u_b$ is the onshore wind at patch border. To find its value, we integrate the forcing from $-\infty$ to the patch border, giving

$$\int_{-\infty}^{x_b} \beta \exp\left(-\frac{(x-x_b)^2}{2\sigma^2}\right) \exp\left(-\frac{z}{h_l}\right) dx = \frac{u_b^2}{2} \tag{C.4}$$

Thus,

$$\frac{u_b^2}{2} = \beta\sigma\sqrt{\frac{\pi}{2}} \exp\left(-\frac{z}{h_l}\right) \tag{C.5}$$

Since $\beta = \frac{u_{max}^2}{2\sigma_m\sqrt{2\pi}}$, the above expression yields

$$u_b = \frac{u_{max}}{\sqrt{2}} \exp\left(\frac{-z}{2h_l}\right) \tag{C.6}$$

Integrating both sides of equation C.18 in z, we obtain

$$w(z) = \int_0^z \frac{u_b(z)}{L} dz \tag{C.7}$$

Substituting equation C.21, this becomes

$$w(z) = \frac{\sqrt{2}h_l u_{max}}{L}\left(1 - \exp\left(\frac{-z}{2h_l}\right)\right) \tag{C.8}$$

## C.2 Derivation of reference w profile for sea-surface temperature forcing (SSTA) simulations

Although an expected vertical wind in the case of SSTA requires more assumptions than for the other two cases, a rough estimate can be obtained by assuming a constant temperature difference of 2 kelvin between the patch and the surroundings, extending from the surface to a level $H$, where the pressure is assumed to equalize at a value $p_b$. A more rigorous treatment would involve a transition layer where the temperatures also equalize—requiring an additional parameter for the depth of that layer. However, we are interested in the winds over the mixed layer, where the potential temperature is approximately conserved, and so is the temperature anomaly.

We start from hydrostatic balance and assume an approximate density variation dictated by $\rho = \rho_0(1 - \beta T')$, where $\beta = 1/T_0$, with $T_0 = 300K$ a reference temperature. This approximation for $\rho$ is reasonable since the scale of interest ($\sim 1km$) is substantially smaller than typical scale heights for the atmosphere ($\sim 8km$). This gives

$$\frac{\partial p}{\partial z} = -\rho_0 g(1 - \beta T'). \tag{C.9}$$

Separating variables and integrating from pressure $p_b$, we obtain the pressure in the mixed layer over the patch:

$$p_p(z) = -\rho_0 g(1 - \beta T')(z - H) + p_b. \tag{C.10}$$

Analogously, the pressure of the surroundings is

$$p_{surr}(z) = -\rho_0 g(z - H) + p_b. \tag{C.11}$$

This yields a pressure difference $(p_{surr} - p_p)$

$$\Delta p = \rho_0 g \frac{T'}{T_0}(H - z). \tag{C.12}$$

We can use Bernoulli's equation to relate this pressure drop to a theoretical maximum wind speed at the border $u_b$ as

$$\frac{u_b^2}{2} = g\frac{T'}{T_0}(H - z), \tag{C.13}$$

Which gives

$$u_b = \left(2g\frac{T'}{T_0}(H - z)\right)^{1/2}. \tag{C.14}$$

Finally, integrating mass continuity (equation C.22), we obtain

$$w(z) = \frac{1}{L}\left(2g\frac{T'}{T_0}\right)^{1/2}\left[-\frac{2}{3}\left((H - z)^{3/2} - H^{3/2}\right)\right]. \tag{C.15}$$

## C.3 Derivation of reference w profile for momentum forcing (MF) simulations

From mass continuity, we have

$$-\frac{\partial w}{\partial z} = \frac{\partial u}{\partial x} \tag{C.16}$$

Integrating in x across the patch yields

$$-\int_{-L}^{L}\frac{\partial w}{\partial z}dx = \int_{-L}^{L}\frac{\partial u}{\partial x}dx, \tag{C.17}$$

which implies

$$-2L\frac{\partial w}{\partial z} = -2u_b, \tag{C.18}$$

where $u_b$ is the onshore wind at patch border. To find its value, we integrate the forcing from $-\infty$ to the patch border, giving

$$\int_{-\infty}^{x_b} \beta \exp\left(-\frac{(x-x_b)^2}{2\sigma^2}\right) \exp\left(-\frac{z}{h_l}\right) dx = \frac{u_b^2}{2} \tag{C.19}$$

Thus,

$$\frac{u_b^2}{2} = \beta\sigma\sqrt{\frac{\pi}{2}} \exp\left(-\frac{z}{h_l}\right) \tag{C.20}$$

Since $\beta = \frac{u_{max}^2}{2\sigma_m\sqrt{2\pi}}$, the above expression yields

$$u_b = \frac{u_{max}}{\sqrt{2}} \exp\left(\frac{-z}{2h_l}\right) \tag{C.21}$$

Integrating both sides of equation C.18 in z, we obtain

$$w(z) = \int_0^z \frac{u_b(z)}{L} dz \tag{C.22}$$

Substituting equation C.21, this becomes

$$w(z) = \frac{\sqrt{2}h_l u_{max}}{L}\left(1 - \exp\left(\frac{-z}{2h_l}\right)\right) \tag{C.23}$$

## C.4 Derivation of reference w profile for sea-surface temperature forcing (SSTA) simulations

Although an expected vertical wind in the case of SSTA requires more assumptions than for the other two cases, a rough estimate can be obtained by assuming a constant temperature difference of 2 kelvin between the patch and the surroundings, extending from the surface to a level $H$, where the pressure is assumed to equalize at a value $p_b$. A more rigorous treatment would involve a transition layer where the temperatures also equalize—requiring

an additional parameter for the depth of that layer. However, we are interested in the winds over the mixed layer, where the potential temperature is approximately conserved, and so is the temperature anomaly.

We start from hydrostatic balance and assume an approximate density variation dictated by $\rho = \rho_0(1 - \beta T')$, where $\beta = 1/T_0$, with $T_0 = 300K$ a reference temperature. This approximation for $\rho$ is reasonable since the scale of interest ($\sim 1km$) is substantially smaller than typical scale heights for the atmosphere ($\sim 8km$). This gives

$$\frac{\partial p}{\partial z} = -\rho_0 g(1 - \beta T'). \tag{C.24}$$

Separating variables and integrating from pressure $p_b$, we obtain the pressure in the mixed layer over the patch:

$$p_p(z) = -\rho_0 g(1 - \beta T')(z - H) + p_b. \tag{C.25}$$

Analogously, the pressure of the surroundings is

$$p_{surr}(z) = -\rho_0 g(z - H) + p_b. \tag{C.26}$$

This yields a pressure difference $(p_{surr} - p_p)$

$$\Delta p = \rho_0 g \frac{T'}{T_0}(H - z). \tag{C.27}$$

We can use Bernoulli's equation to relate this pressure drop to a theoretical maximum wind speed at the border $u_b$ as

$$\frac{u_b^2}{2} = g\frac{T'}{T_0}(H - z), \tag{C.28}$$

Which gives

$$u_b = \left(2g\frac{T'}{T_0}(H - z)\right)^{1/2}. \tag{C.29}$$

Finally, integrating mass continuity (equation C.22), we obtain

$$w(z) = \frac{1}{L}\left(2g\frac{T'}{T_0}\right)^{1/2}\left[-\frac{2}{3}\left((H - z)^{3/2} - H^{3/2}\right)\right]. \tag{C.30}$$

## C.5 Derivation of the Normalized Gross Moist Stability ($\Gamma_R$) and its approximation by the contributions from mean vertical transport of moist and dry static energy ($\Gamma_W$)

Following Raymond et al. (2009), we derive a form of the Normalized Gross Moist Stability, $\Gamma_R$, based on the moist and dry static energies, $h$ and $s$. Starting from the budgets for $h$ and for latent energy, $L_v q$ (which we write as $h - s$), where $q$ is the specific humidity and $L_v$ the latent heat of vaporization, we have, in steady state

$$\nabla \cdot \langle \vec{v} h \rangle = \dot{Q}_{atm} \tag{C.31}$$

$$-\nabla \cdot \langle \vec{v}(h - s) \rangle = P - E, \tag{C.32}$$

where angle brackets represent mass-weighted, vertically integrated quantities. Combining these yields

$$P - E = \frac{\dot{Q}_{atm}}{\frac{\nabla \cdot \langle \vec{v} h \rangle}{\nabla \cdot \langle \vec{v}(s-h) \rangle}}. \tag{C.33}$$

As this shows, $\Gamma_R = \frac{\nabla \cdot \langle \vec{v} h \rangle}{\nabla \cdot \langle \vec{v}(s-h) \rangle}$. Neglecting transients as well as contributions from horizontal transport in both the numerator and denominator gives $\Gamma_W = \frac{\langle \overline{w}(\partial \overline{h}/\partial z) \rangle}{\langle \overline{w} \partial(\overline{s}-\overline{h})/\partial z \rangle}$, an approximation to the full NGMS that leaves out contributions from eddy transient terms such as $\langle \overline{w'(\partial h'/\partial z)} \rangle$, or horizontal transport terms such as $\langle \overline{u(\partial h/\partial x)} \rangle$.

Simple algebraic manipulation allows us to write equation C.33 as

$$P - E = \frac{\dot{Q}_{atm}}{M} - \dot{Q}_{atm}, \tag{C.34}$$

where $M = \frac{\nabla \cdot \langle \vec{v} h \rangle}{\nabla \cdot \langle \vec{v} s \rangle}$ is an alternative definition of a NGMS, and is related to our definition by $\Gamma_R = \frac{M}{1-M}$. Equation C.34 is equivalent to equation 5 in Wang and Sobel (2012) and equation 3 in Anber et al. (2015), except that they approximate $M$ by the mean vertical contributions only, namely taking $M \approx \frac{\langle \overline{w} \partial \overline{h}/\partial z \rangle}{\langle \overline{w} \partial \overline{s}/\partial z \rangle}$.

# References


Abbott, T. (2023, August). Pytrack: Multi [Branch: multi].

Adams, E. E., Cosler, D. J., & Helfrich, K. R. (1990). Evaporation from heated water bodies: Predicting combined forced plus free convection. *Water Resources Research*, *26*(3), 425–435.

American Meteorological Society. (n.d.). Thermal low [Online; accessed 11/10/2023]. http://glossary.ametsoc.org/wiki/Thermal_low

Anber, U., Wang, S., & Sobel, A. (2015). Effect of surface fluxes versus radiative heating on tropical deep convection. *Journal of the Atmospheric Sciences*, *72*(9), 3378–3388.

Aurnou, J. M., Horn, S., & Julien, K. (2020). Connections between nonrotating, slowly rotating, and rapidly rotating turbulent convection transport scalings. *Physical Review Research*, *2*(4), 043115.

Back, L. E., & Bretherton, C. S. (2009). On the relationship between sst gradients, boundary layer winds, and convergence over the tropical oceans. *Journal of Climate*, *22*(15), 4182–4196.

Back, L. E., & Bretherton, C. (2006). Geographic variability in the export of moist static energy and vertical motion profiles in the tropical pacific. *Geophysical research letters*, *33*(17).

Bénard, H. (1901). *Les tourbillons cellulaires dans une nappe liquide propageant de la chaleur par convection: En régime permanent*. Gauthier-Villars.

Berlengiero, M., Emanuel, K., Von Hardenberg, J., Provenzale, A., & Spiegel, E. (2012). Internally cooled convection: A fillip for philip. *Communications in Nonlinear Science and Numerical Simulation*, *17*(5), 1998–2007.

Beucler, T., & Cronin, T. (2019). A budget for the size of convective self-aggregation. *Quarterly Journal of the Royal Meteorological Society*, *145*(720), 947–966.

Beucler, T., Cronin, T., & Emanuel, K. (2018). A linear response framework for radiative-convective instability. *Journal of Advances in Modeling Earth Systems*, *10*(8), 1924–1951.

Bischoff, T., & Schneider, T. (2014). Energetic constraints on the position of the intertropical convergence zone. *Journal of Climate*, *27*(13), 4937–4951.

Bogatyrev, G. (1990). Excitation of cyclonic vortex or laboratory model of tropical cyclone. *JETP Lett*, *51*(11), 630–633.

Bogatyrev, G., Kolesnichenko, I., Levina, G., & Sukhanovsky, A. (2006). Laboratory model of generation of a large-scale spiral vortex in a convectively unstable rotating fluid. *Izvestiya, Atmospheric and Oceanic Physics*, *42*, 423–429.

Boos, W. R., & Korty, R. L. (2016). Regional energy budget control of the intertropical convergence zone and application to mid-holocene rainfall. *Nature Geoscience*, *9*(12), 892–897.

Boubnov, B., & Golitsyn, G. (1986). Experimental study of convective structures in rotating fluids. *Journal of Fluid Mechanics*, *167*, 503–531.

Bouillaut, V., Lepot, S., Aumaıtre, S., & Gallet, B. (2019). Transition to the ultimate regime in a radiatively driven convection experiment. *Journal of Fluid Mechanics*, *861*.

Bretherton, C. S., Blossey, P. N., & Khairoutdinov, M. (2005). An energy-balance analysis of deep convective self-aggregation above uniform sst. *Journal of the atmospheric sciences*, *62*(12), 4273–4292.

Bretherton, C. S., Peters, M. E., & Back, L. E. (2004). Relationships between water vapor path and precipitation over the tropical oceans. *Journal of climate*, *17*(7), 1517–1528.

Brown, E., & Ahlers, G. (2006). Effect of the earth's coriolis force on the large-scale circulation of turbulent rayleigh-bénard convection. *Physics of Fluids*, *18*(12).

Brown, E., Nikolaenko, A., & Ahlers, G. (2005). Reorientation of the large-scale circulation in turbulent rayleigh-bénard convection. *Phys. Rev. Lett.*, *95*, 084503. https://doi.org/10.1103/PhysRevLett.95.084503

Burns, K. J., Vasil, G. M., Oishi, J. S., Lecoanet, D., & Brown, B. P. (2020). Dedalus: A flexible framework for numerical simulations with spectral methods. *Physical Review Research*, *2*(2), 023068.

Busse, F. H. (2006). Bénard convection and geophysical applications. In *Dynamics of spatio-temporal cellular structures: Henri bénard centenary review* (pp. 103–125). Springer.

Carstens, J. D., & Wing, A. A. (2020). Tropical cyclogenesis from self-aggregated convection in numerical simulations of rotating radiative-convective equilibrium. *Journal of Advances in Modeling Earth Systems*, *12*(5), e2019MS002020.

Chandrasekhar, S. (1953). Problems of stability in hydrodynamics and hydromagnetics (george darwin lecture). *Monthly Notices of the Royal Astronomical Society*, *113*, 667.

Chandrasekhar, S. (1961). Hydrodynamic and hydromagnetic stability, 652 pp., clarendon.

Chapman, C., & Proctor, M. (1980). Nonlinear rayleigh–bénard convection between poorly conducting boundaries. *Journal of Fluid Mechanics*, *101*(4), 759–782.

Chavas, D. R. (2017). A simple derivation of tropical cyclone ventilation theory and its application to capped surface entropy fluxes. *Journal of the Atmospheric Sciences*, *74*(9), 2989–2996.

Chavas, D. R., & Emanuel, K. (2014). Equilibrium tropical cyclone size in an idealized state of axisymmetric radiative–convective equilibrium. *Journal of the Atmospheric Sciences*, *71*(5), 1663–1680.

Chavas, D. R., & Lin, N. (2016). A model for the complete radial structure of the tropical cyclone wind field. part ii: Wind field variability. *Journal of the Atmospheric Sciences*, *73*(8), 3093–3113.

Chavas, D. R., Lin, N., & Emanuel, K. (2015). A model for the complete radial structure of the tropical cyclone wind field. part i: Comparison with observed structure. *Journal of the Atmospheric Sciences*, *72*(9), 3647–3662.

Chien, M.-H., Pauluis, O. M., & Almgren, A. S. (2022). Hurricane-like vortices in conditionally unstable moist convection. *Journal of Advances in Modeling Earth Systems*, *14*(7), e2021MS002846.

Craig, G. C., & Gray, S. L. (1996). Cisk or wishe as the mechanism for tropical cyclone intensification. *Journal of Atmospheric Sciences*, *53*(23), 3528–3540.

Cronin, T. W. (2014). On the choice of average solar zenith angle. *Journal of the Atmospheric Sciences*, *71*(8), 2994–3003.

Cronin, T. W. (2023). An analytic model for tropical cyclone outer winds. *Geophysical Research Letters*, *50*(11), e2023GL103942.

Cronin, T. W., & Chavas, D. R. (2019). Dry and semidry tropical cyclones. *Journal of the Atmospheric Sciences*, *2019*(1), 1–20.

Cronin, T. W., Emanuel, K. A., & Molnar, P. (2015). Island precipitation enhancement and the diurnal cycle in radiative-convective equilibrium. *Quarterly Journal of the Royal Meteorological Society*, *141*(689), 1017–1034.

Davis, C. A. (2015). The formation of moist vortices and tropical cyclones in idealized simulations. *Journal of the Atmospheric Sciences*, *72*(9), 3499–3516.

Derbyshire, S., Beau, I., Bechtold, P., Grandpeix, J.-Y., Piriou, J.-M., Redelsperger, J.-L., & Soares, P. (2004). Sensitivity of moist convection to environmental humidity. *Quarterly Journal of the Royal Meteorological Society: A journal of the atmospheric sciences, applied meteorology and physical oceanography*, *130*(604), 3055–3079.

Dinçer, İ., & Zamfirescu, C. (2016). *Drying phenomena: Theory and applications*. John Wiley & Sons.

Dingley, B., Dagan, G., & Stier, P. (2021). Forcing convection to aggregate using diabatic heating perturbations. *Journal of Advances in Modeling Earth Systems*, *13*(10), e2021MS002579.

Donohoe, A., Marshall, J., Ferreira, D., & Mcgee, D. (2013). The relationship between itcz location and cross-equatorial atmospheric heat transport: From the seasonal cycle to the last glacial maximum. *Journal of Climate*, *26*(11), 3597–3618.

Dowling, T. (1988). Rotating rayleigh–bénard convection with fixed flux boundaries. *Summer Study Program in Geophysical Fluid Dynamics, Woods Hole Oceanographic Institution Technical Report*, 230–247.

Duffy, M. L., O'Gorman, P. A., & Back, L. E. (2020). Importance of laplacian of low-level warming for the response of precipitation to climate change over tropical oceans. *Journal of Climate*, *33*(10), 4403–4417.

Ecke, R. E., & Shishkina, O. (2023). Turbulent rotating rayleigh–bénard convection. *Annual Review of Fluid Mechanics*, *55*, 603–638.

Emanuel, K. A. (1994). *Atmospheric convection*. Oxford University Press, USA.

Emanuel, K. (1986). An air-sea interaction theory for tropical cyclones. part i: Steady-state maintenance. *Journal of Atmospheric Sciences*, *43*(6), 585–605.

Emanuel, K. (2019). Inferences from simple models of slow, convectively coupled processes. *Journal of the Atmospheric Sciences*, *76*(1), 195–208.

Emanuel, K., & Rotunno, R. (2011). Self-stratification of tropical cyclone outflow. part i: Implications for storm structure. *Journal of the Atmospheric Sciences*, *68*(10), 2236–2249.

Fernando, H. J., Chen, R.-R., & Boyer, D. L. (1991). Effects of rotation on convective turbulence. *Journal of Fluid Mechanics*, *228*, 513–547.

Fonda, E., & Sreenivasan, K. R. (2015). Turbulent thermal convection. In *Selected topics of computational and experimental fluid mechanics* (pp. 37–49). Springer.

Gnip, I., Vėjelis, S., & Vaitkus, S. (2012). Thermal conductivity of expanded polystyrene (eps) at 10 c and its conversion to temperatures within interval from 0 to 50 c. *Energy and Buildings*, *52*, 107–111.

Goluskin, D. (2016). *Internally heated convection and rayleigh-bénard convection*. Springer.

Gray, W. M. (1975). *Tropical cyclone genesis* [Doctoral dissertation, Colorado State University. Libraries].

Guervilly, C., & Hughes, D. W. (2017). Jets and large-scale vortices in rotating rayleigh-bénard convection. *Physical Review Fluids*, *2*(11), 113503.

Guervilly, C., Hughes, D. W., & Jones, C. A. (2014). Large-scale vortices in rapidly rotating rayleigh–bénard convection. *Journal of Fluid Mechanics*, *758*, 407–435.

Haerter, J. O., Böing, S. J., Henneberg, O., & Nissen, S. B. (2019). Circling in on convective organization. *Geophysical Research Letters*, *46*(12), 7024–7034.

Hart, J., Kittelman, S., & Ohlsen, D. (2002). Mean flow precession and temperature probability density functions in turbulent rotating convection. *Physics of Fluids*, *14*(3), 955–962.

Held, I. M. (2005). The gap between simulation and understanding in climate modeling. *Bulletin of the American Meteorological Society*, *86*(11), 1609–1614.

Held, I. M., Hemler, R. S., & Ramaswamy, V. (1993). Radiative-convective equilibrium with explicit two-dimensional moist convection. *Journal of Atmospheric Sciences*, *50*(23), 3909–3927.

Houze Jr, R. A., & Betts, A. K. (1981). Convection in gate. *Reviews of Geophysics*, *19*(4), 541–576.

Hurle, D., Jakeman, E., & Pike, E. R. (1967). On the solution of the bénard problem with boundaries of finite conductivity. *Proceedings of the Royal Society of London. Series A. Mathematical and Physical Sciences*, *296*(1447), 469–475.

Incropera, F. P., DeWitt, D. P., Bergman, T. L., Lavine, A. S., et al. (1996). *Fundamentals of heat and mass transfer* (Vol. 6). Wiley New York.

Jakob, C., Singh, M., & Jungandreas, L. (2019). Radiative convective equilibrium and organized convection: An observational perspective. *Journal of Geophysical Research: Atmospheres*, *124*(10), 5418–5430.

Jeevanjee, N., Hassanzadeh, P., Hill, S., & Sheshadri, A. (2017). A perspective on climate model hierarchies. *Journal of Advances in Modeling Earth Systems*, *9*(4), 1760–1771.

Jeevanjee, N., & Romps, D. M. (2013). Convective self-aggregation, cold pools, and domain size. *Geophysical Research Letters*, *40*(5), 994–998.

Johnson, R. (2003). Thermal low. *Encyclopedia of Atmospheric Science*, 2269–2273.

Julien, K., Legg, S., McWilliams, J., & Werne, J. (1996). Rapidly rotating turbulent rayleigh-bénard convection. *Journal of Fluid Mechanics*, *322*, 243–273.

Julien, K., Knobloch, E., & Plumley, M. (2018). Impact of domain anisotropy on the inverse cascade in geostrophic turbulent convection. *Journal of Fluid Mechanics*, *837*.

Kannan, V. (2023). Hydrodynamics of cyclogenesis from numerical simulations. https://doi.org/10.17863/CAM.93479

Khairoutdinov, M., & Emanuel, K. (2013). Rotating radiative-convective equilibrium simulated by a cloud-resolving model. *Journal of Advances in Modeling Earth Systems*, *5*(4), 816–825.

Khairoutdinov, M. F., & Randall, D. A. (2003). Cloud resolving modeling of the arm summer 1997 iop: Model formulation, results, uncertainties, and sensitivities. *Journal of Atmospheric Sciences*, *60*(4), 607–625.

King, E. M., Stellmach, S., & Aurnou, J. M. (2012). Heat transfer by rapidly rotating rayleigh–bénard convection. *Journal of Fluid Mechanics*, *691*, 568–582.

Kleinschmidt, E. (1951). Grundlagen einer theorie der tropischen zyklonen. *Archiv für Meteorologie, Geophysik und Bioklimatologie, Serie A*, *4*(1), 53–72.

Krishnamurti, R., & Howard, L. N. (1981). Large-scale flow generation in turbulent convection. *Proceedings of the National Academy of Sciences*, *78*(4), 1981–1985.

Kuang, Z. (2010). Linear response functions of a cumulus ensemble to temperature and moisture perturbations and implications for the dynamics of convectively coupled waves. *Journal of the atmospheric sciences*, *67*(4), 941–962.

Kuang, Z. (2012). Weakly forced mock walker cells. *Journal of the Atmospheric Sciences*, *69*(9), 2759–2786.

Kuang, Z. (2018). Linear stability of moist convecting atmospheres. part i: From linear response functions to a simple model and applications to convectively coupled waves. *Journal of the Atmospheric Sciences*, *75*(9), 2889–2907.

Kunnen, R., Clercx, H., & Geurts, B. J. (2008). Breakdown of large-scale circulation in turbulent rotating convection. *EPL (Europhysics Letters)*, *84*(2), 24001.

Kunnen, R. P. (2021). The geostrophic regime of rapidly rotating turbulent convection. *Journal of Turbulence*, *22*(4-5), 267–296.

Lemmon, E. W. (2010). Thermophysical properties of fluid systems. *NIST chemistry WebBook*.

Lepot, S., Aumaıtre, S., & Gallet, B. (2018). Radiative heating achieves the ultimate regime of thermal convection. *Proceedings of the National Academy of Sciences*, *115*(36), 8937–8941.

Lindzen, R. S., & Nigam, S. (1987). On the role of sea surface temperature gradients in forcing low-level winds and convergence in the tropics. *Journal of Atmospheric Sciences*, *44*(17), 2418–2436.

Malkus, J. S., & Riehl, H. (1960). On the dynamics and energy transformations in steady-state hurricanes. *Tellus*, *12*(1), 1–20.

Manabe, S., & Wetherald, R. T. (1967). Thermal equilibrium of the atmosphere with a given distribution of relative humidity.

Marshall, J., Donohoe, A., Ferreira, D., & McGee, D. (2014). The ocean's role in setting the mean position of the inter-tropical convergence zone. *Climate Dynamics*, *42*, 1967–1979.

Martinez-Villalobos, C., & Neelin, J. D. (2019). Why do precipitation intensities tend to follow gamma distributions? *Journal of the Atmospheric Sciences*, *76*(11), 3611–3631.

Montgomery, M. T., Persing, J., & Smith, R. K. (2015). Putting to rest wishe-ful misconceptions for tropical cyclone intensification. *Journal of Advances in Modeling Earth Systems*, *7*(1), 92–109.

Moran, J. L., Cottrill, A. L., Benck, J. D., Liu, P., Yuan, Z., Strano, M. S., & Buongiorno, J. (2018). Noble-gas-infused neoprene closed-cell foams achieving ultra-low thermal conductivity fabrics. *RSC advances*, *8*(38), 21389–21398.

Mrowiec, A. A., Garner, S. T., & Pauluis, O. M. (2011). Axisymmetric hurricane in a dry atmosphere: Theoretical framework and numerical experiments. *Journal of the atmospheric sciences*, *68*(8), 1607–1619.

Muller, C., & Bony, S. (2015). What favors convective aggregation and why? *Geophysical Research Letters*, *42*(13), 5626–5634.

Muller, C. J., & Held, I. M. (2012). Detailed investigation of the self-aggregation of convection in cloud-resolving simulations. *Journal of the Atmospheric Sciences*, *69*(8), 2551–2565.

Muller, C. J., & Romps, D. M. (2018). Acceleration of tropical cyclogenesis by self-aggregation feedbacks. *Proceedings of the National Academy of Sciences*, *115*(12), 2930–2935.

Nakazawa, T. (1988). Tropical super clusters within intraseasonal variations over the western pacific. *Journal of the Meteorological Society of Japan. Ser. II*, *66*(6), 823–839.

National Hurricane Center. (n.d.). Glossary [Available: https://www.nhc.noaa.gov/aboutgloss.shtml [Accessed: 05/07/2023]]. National Oceanic and Atmospheric Administration.

Neelin, J. D., & Held, I. M. (1987). Modeling tropical convergence based on the moist static energy budget. *Monthly Weather Review*, *115*(1), 3–12.

Nieves, D., Rubio, A. M., & Julien, K. (2014). Statistical classification of flow morphology in rapidly rotating rayleigh-bénard convection. *Physics of Fluids*, *26*(8), 086602.

Nolan, D. S. (2007). What is the trigger for tropical cyclogenesis. *Australian Meteorological Magazine*, *56*(4), 241–266.

Nolan, D. S., Rappin, E. D., & Emanuel, K. A. (2007). Tropical cyclogenesis sensitivity to environmental parameters in radiative–convective equilibrium. *Quarterly Journal of the Royal Meteorological Society: A journal of the atmospheric sciences, applied meteorology and physical oceanography*, *133*(629), 2085–2107.

Orlanski, I. (1975). A rational subdivision of scales for atmospheric processes. *Bulletin of the American Meteorological Society*, 527–530.

Oruba, L., Davidson, P., & Dormy, E. (2017). Eye formation in rotating convection. *Journal of Fluid Mechanics*, *812*, 890–904.

Oruba, L., Davidson, P., & Dormy, E. (2018). Formation of eyes in large-scale cyclonic vortices. *Physical Review Fluids*, *3*(1), 013502.

Pauluis, O., & Schumacher, J. (2010). Idealized moist rayleigh-bénard convection with piecewise linear equation of state. *Communications in Mathematical Sciences*, *8*(1), 295–319.

Pauluis, O., & Schumacher, J. (2011). Self-aggregation of clouds in conditionally unstable moist convection. *Proceedings of the National Academy of Sciences*, *108*(31), 12623–12628.

Peters, O., & Neelin, J. D. (2006). Critical phenomena in atmospheric precipitation. *Nature physics*, *2*(6), 393–396.

Plumley, M., & Julien, K. (2019). Scaling laws in rayleigh-benard convection. *Earth and Space Science*, *6*(9), 1580–1592.

Rácz, Z., & Smith, R. K. (1999). The dynamics of heat lows. *Quarterly Journal of the Royal Meteorological Society*, *125*(553), 225–252.

Ramírez Reyes, A., & Yang, D. (2021). Spontaneous cyclogenesis without radiative and surface-flux feedbacks. *Journal of the Atmospheric Sciences*, *78*(12), 4169–4184.

Rapp, B. E. (2016). *Microfluidics: Modeling, mechanics and mathematics*. William Andrew.

Rappin, E. D., Nolan, D. S., & Emanuel, K. A. (2010). Thermodynamic control of tropical cyclogenesis in environments of radiative-convective equilibrium with shear. *Quarterly Journal of the Royal Meteorological Society*, *136*(653), 1954–1971.

Rayleigh, L. (1916). Lix. on convection currents in a horizontal layer of fluid, when the higher temperature is on the under side. *The London, Edinburgh, and Dublin Philosophical Magazine and Journal of Science*, *32*(192), 529–546.

Raymond, D. J. (2000). Thermodynamic control of tropical rainfall. *Quarterly Journal of the Royal Meteorological Society*, *126*(564), 889–898.

Raymond, D. J., Sessions, S. L., Sobel, A. H., & Fuchs, Ž. (2009). The mechanics of gross moist stability. *Journal of Advances in Modeling Earth Systems*, *1*(3).

Riehl, H. (1950). A model of hurricane formation. *Journal of Applied physics*, *21*(9), 917–925.

Rossby, H. (1969). A study of bénard convection with and without rotation. *Journal of Fluid Mechanics*, *36*(2), 309–335.

Rotunno, R., & Emanuel, K. A. (1987). An air–sea interaction theory for tropical cyclones. part ii: Evolutionary study using a nonhydrostatic axisymmetric numerical model. *Journal of Atmospheric Sciences*, *44*(3), 542–561.

Ruppert Jr, J. H., Wing, A. A., Tang, X., & Duran, E. L. (2020). The critical role of cloud–infrared radiation feedback in tropical cyclone development. *Proceedings of the National Academy of Sciences*, *117*(45), 27884–27892.

Rushley, S. S., Kim, D., Bretherton, C., & Ahn, M.-S. (2018). Reexamining the nonlinear moisture-precipitation relationship over the tropical oceans. *Geophysical research letters*, *45*(2), 1133–1140.

Russell, B. (2009). *An outline of philosophy*. Routledge.

Schneider, T., Bischoff, T., & Haug, G. H. (2014). Migrations and dynamics of the intertropical convergence zone. *Nature*, *513*(7516), 45–53.

Shamekh, S., Muller, C., Duvel, J.-P., & d'Andrea, F. (2020). How do ocean warm anomalies favor the aggregation of deep convective clouds? *Journal of the Atmospheric Sciences*, *77*(11), 3733–3745.

Shi, X., & Bretherton, C. S. (2014). Large-scale character of an atmosphere in rotating radiative-convective equilibrium. *Journal of Advances in Modeling Earth Systems*, *6*(3), 616–629.

Singh, M. S., Warren, R. A., & Jakob, C. (2019). A steady-state model for the relationship between humidity, instability, and precipitation in the tropics. *Journal of Advances in Modeling Earth Systems*, *11*(12), 3973–3994.

Sobel, A. H. (2007). Simple models of ensemble-averaged tropical precipitation and surface wind, given the sea surface temperature. *The global circulation of the atmosphere*, *219*, 251.

Sobel, A. H., & Neelin, J. D. (2006). The boundary layer contribution to intertropical convergence zones in the quasi-equilibrium tropical circulation model framework. *Theoretical and Computational Fluid Dynamics*, *20*, 323–350.

Spengler, T., & Smith, R. K. (2008). The dynamics of heat lows over flat terrain. *Quarterly Journal of the Royal Meteorological Society: A journal of the atmospheric sciences, applied meteorology and physical oceanography*, *134*(637), 2157–2172.

Sreenivasan, K. R., Bershadskii, A., & Niemela, J. (2002). Mean wind and its reversal in thermal convection. *Physical Review E*, *65*(5), 056306.

Stevens, R. J., Clercx, H. J., & Lohse, D. (2013). Heat transport and flow structure in rotating rayleigh–bénard convection. *European Journal of Mechanics-B/Fluids*, *40*, 41–49.

Stevens, R. J., Zhong, J.-Q., Clercx, H. J., Ahlers, G., & Lohse, D. (2009). Transitions between turbulent states in rotating rayleigh-bénard convection. *Physical review letters*, *103*(2), 024503.

Sukhanovskii, A., Evgrafova, A., & Popova, E. (2016). Laboratory study of a steady-state convective cyclonic vortex. *Quarterly Journal of the Royal Meteorological Society*, *142*(698), 2214–2223.

Takehiro, S.-i., Ishiwatari, M., Nakajima, K., & Hayashi, Y.-Y. (2002). Linear stability of thermal convection in rotating systems with fixed heat flux boundaries. *Geophysical & Astrophysical Fluid Dynamics*, *96*(6), 439–459.

Tian, Y., & Kuang, Z. (2019). Why does deep convection have different sensitivities to temperature perturbations in the lower versus upper troposphere? *Journal of the Atmospheric Sciences*, *76*(1), 27–41.

Tulich, S. N., & Mapes, B. E. (2010). Transient environmental sensitivities of explicitly simulated tropical convection. *Journal of the atmospheric sciences*, *67*(4), 923–940.

Vallis, G. K., Parker, D. J., & Tobias, S. M. (2019). A simple system for moist convection: The rainy–bénard model. *Journal of Fluid Mechanics*, *862*, 162–199.

Velez-Pardo, M. (2023). Accompanying data for "the response of tropical rainfall to idealized small-scale thermal and mechanical forcing", by martin velez-pardo and timothy w. cronin. https://doi.org/10.5281/zenodo.10086216

Velez-Pardo, M., & Cronin, T. W. (2023). Large-scale circulations and dry tropical cyclones in direct numerical simulations of rotating rayleigh–bénard convection. *Journal of the Atmospheric Sciences*, *80*(9), 2221–2237.

Vieweg, P. P., Scheel, J. D., & Schumacher, J. (2021). Supergranule aggregation for constant heat flux-driven turbulent convection. *Physical Review Research*, *3*(1), 013231.

Vieweg, P. P., Scheel, J. D., Stepanov, R., & Schumacher, J. (2022). Inverse cascades of kinetic energy and thermal variance in three-dimensional horizontally extended turbulent convection. *arXiv preprint arXiv:2207.12606*.

Wang, D., & Lin, Y. (2020). Size and structure of dry and moist reversible tropical cyclones. *Journal of the Atmospheric Sciences*, *77*(6), 2091–2114.

Wang, D., & Lin, Y. (2021). Potential role of irreversible moist processes in modulating tropical cyclone surface wind structure. *Journal of the Atmospheric Sciences*, *78*(3), 709–725.

Wang, D., Lin, Y., & Chavas, D. R. (2022). Tropical cyclone potential size. *Journal of the Atmospheric Sciences*, *79*(11), 3001–3025.

Wang, S., & Sobel, A. (2012). Impact of imposed drying on deep convection in a cloud-resolving model. *Journal of Geophysical Research: Atmospheres*, *117*(D2).

Wang, S., & Sobel, A. H. (2017). Factors controlling rain on small tropical islands: Diurnal cycle, large-scale wind speed, and topography. *Journal of the Atmospheric Sciences*, *74*(11), 3515–3532.

Weiss, S., & Ahlers, G. (2011). The large-scale flow structure in turbulent rotating rayleigh–bénard convection. *Journal of fluid mechanics*, *688*, 461–492.

Wing, A. A. (2022). Acceleration of tropical cyclone development by cloud-radiative feedbacks. *Journal of the Atmospheric Sciences*, *79*(9), 2285–2305.

Wing, A. A., Emanuel, K., Holloway, C. E., & Muller, C. (2018). Convective self-aggregation in numerical simulations: A review. *Shallow clouds, water vapor, circulation, and climate sensitivity*, 1–25.

Wing, A. A., & Emanuel, K. A. (2014). Physical mechanisms controlling self-aggregation of convection in idealized numerical modeling simulations. *Journal of Advances in Modeling Earth Systems*, *6*(1), 59–74.

Zhang, F., & Emanuel, K. (2016). On the role of surface fluxes and wishe in tropical cyclone intensification. *Journal of Atmospheric Sciences*, *73*(5), 2011–2019.

Zhong, J.-Q., & Ahlers, G. (2010). Heat transport and the large-scale circulation in rotating turbulent rayleigh–bénard convection. *Journal of fluid mechanics*, *665*, 300–333.

Zhou, W., Held, I. M., & Garner, S. T. (2014). Parameter study of tropical cyclones in rotating radiative–convective equilibrium with column physics and resolution of a 25-km gcm. *Journal of the Atmospheric Sciences*, *71*(3), 1058–1069.